AD-A279 115

STRESS WAVE PROPAGATION IN UNSATURATED SANDS - VOL I: CENTRIFUGE MODELING

A.J. WALSH; W.A. CHARLIE

COLORADO STATE UNIVERSITY
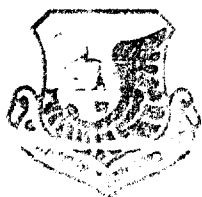FORT COLLINS CO 80523

APRIL 1993

DTIC
ELECTE
MAY 1 1 1994
S B D

FINAL REPORT

SEPTEMBER 1990 - OCTOBER 1992

94-13967

DTIC QUALITY INSPECTED 2

NOTICE

PLEASE DO NOT REQUEST COPIES OF THIS REPORT FROM HQ AFCESA/RA (AIR
FORCE CIVIL ENGINEERING SUPPORT AGENCY). ADDITIONAL COPIES MAY BE
PURCHASED FROM:

> NATIONAL TECHNICAL INFORMATION SERVICE
> 5285 PORT ROYAL ROAD
> SPRINGFIELD, VIRGINIA 22161

FEDERAL GOVERNMENT AGENCIES AND THEIR CONTRACTORS REGISTERED
WITH DEFENSE TECHNICAL INFORMATION CENTER SHOULD DIRECT REQUESTS
FOR COPIES OF THIS REPORT TO:

> DEFENSE TECHNICAL INFORMATION CENTER
> CAMERON STATION
> ALEXANDRIA, VIRGINIA 22314

REPORT DOCUMENTATION PAGE

1 AGENCY USE ONLY (Leave blank)	2 REPORT DATE	3 REPORT TYPE AND DATES COVERED
	April 1993	Final Report, Sept. 1990–October 1991

4 TITLE AND SUBTITLE
Stress Wave Propagation in Unsaturated Sands:
Vol. 1 Centrifuge Modeling

5 FUNDING NUMBERS
F08635-90-C-0306

6 AUTHOR(S)
Andy J. Walsh and Wayne A. Charlie
(Wayne A. Charlie, P.I.)

7 PERFORMING ORGANIZATION NAME(S) AND ADDRESS(ES)
Colorado State University
Fort Collins, CO 80523

8 PERFORMING ORGANIZATION REPORT NUMBER
TR-92-73-VOL.I

9 SPONSORING MONITORING AGENCY NAME(S) AND ADDRESS(ES)
Air Base Survivability Branch
HQ Air Force Civil Engineering Support Agency
139 Barnes Drive
Tyndall AFB, FL 32403-5319

10 SPONSORING MONITORING AGENCY REPORT NUMBER

11 SUPPLEMENTARY NOTES

12a DISTRIBUTION AVAILABILITY STATEMENT
Approved for Public Release Distribution Unlimited

12b DISTRIBUTION CODE

13 ABSTRACT

Explosive model testing was conducted using a geotechnical centrifuge in order to simulate prototype stresses and ground motions in a representative cohesionless backfill. Models were constructed of sand and compacted moist to a constant void ratio using a vibratory technique. Exploding detonators were used to simulate contained bombs in the backfill material. The objective of this study was to determine the influence of moisture content, at the time of backfill compaction, on blast induced stress wave propagation. Models were constructed to 1/18.9 and 1/26.3 scales. Explosives consisted of 1031 mg and 350 mg of PBX 9407 and were buried to depths of 7.6 cm and 5.4 cm respectively. These scaled models simulated prototype charges of 6.9 kg and 6.4 kg (7.8 kg and 7.3 kg TNT equivalent) at a depth of burial of 1.4 meters. Attenuation coefficients (n) show some influence with respect to saturation. Peak stress and peak particle acceleration intercepts at a scaled distance of one ($R/W^{1/3}=1$ m/kg$^{1/3}$ and 1 ft/lb$^{1/3}$) are lowest at 0 and 53 percent saturations and are maximum at 35 percent saturation. Peak particle velocity intercepts are lowest at 0 and 70 percent saturations and again are maximum at 35 percent saturation.

14 SUBJECT TERMS
Centrifuge, Centrifuge Modeling, Sand, Unsaturated sand,
Explosion Modeling, Explosives, Moisture

15 NUMBER OF PAGES
122

16 PRICE CODE

17 SECURITY CLASSIFICATION OF REPORT	18 SECURITY CLASSIFICATION OF THIS PAGE	19 SECURITY CLASSIFICATION OF ABSTRACT	20 LIMITATION OF ABSTRACT
Unclassified	Unclassified	Unclassified	UL

Standard Form 298 (Rev. 2-89)

(The reverse of this page is blank)

EXECUTIVE SUMMARY

STRESS WAVE PROPAGATION IN UNSATURATED SANDS: CENTRIFUGE MODELING

Explosive model testing was conducted using a centrifuge in order to simulate prototype stresses and ground motions in a representative cohesionless backfill. Models were constructed of sand and compacted moist to a constant void ratio using a vibratory technique. Exploding detonators were used to simulate contained bombs in the backfill material. The objective of this study was to determine the influence of moisture content, at the time of backfill compaction, on blast induced stress wave propagation. Models were constructed to 1/18.9 and 1/26.3 scales. Explosives consisted of 1031 mg and 350 mg of PBX 9407 and were buried to depths of 7.6 cm and 5.4 cm respectively. Accelerating these scaled models to 18.9 g's and 26.3 g's simulated prototype charges of 6.9 kg and 6.4 kg (7.8 kg and 7.3 kg TNT equivalent) at a depth of burial of 1.4 meters. Peak stress, peak particle acceleration, and peak particle velocity are presented as a function of scaled distance for both Tyndall beach and Ottawa 20-30 sands. Attenuation coefficients (n) for this data show some influence with respect to saturation. Peak stress and peak particle acceleration intercepts (b) at a scaled distance of one ($R/W^{1/3}$ = 1 $m/kg^{1/3}$ and 1 $ft/lb^{1/3}$) for Tyndall sand are lowest at 0 and 53 percent saturations and are maximum at 35 percent saturation. Peak particle velocity intercepts are lowest at 0 and 70 percent saturations and again are maximum at 35 percent saturation. Peak stress intercepts for Ottawa sand follow a similar trend to stress intercepts of Tyndall sand.

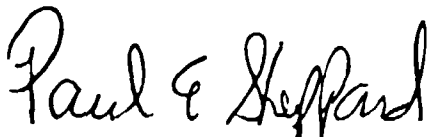(The reverse of this page is blank.)

PREFACE

This report was prepared by the Department of Civil Engineering, Colorado State University, Fort Collins, Colorado, 80523 under contract Number F08635-90-C-0306 for the Air Force Civil Engineering Support Agency, Air Base Survivability Branch (AFCESA/RACS) 139 Barnes Drive, Tyndall AFB, FL, 32403-5319. The work was initiated in November 1989 and was completed in October 1992.

This report is published in two volumes. Volume 1 is written by Mr. Andy J. Walsh and Dr. Wayne A. Charlie and covers centrifuge explosives tests conducted at AFCESA/RACS during the summers of 1990 and 1991. Volume 2 is written by Mr. Edward J. Villano and covers field explosives tests conducted at Colorado State University during the fall of 1991 and spring of 1992. Mr. Andy J. Walsh and Mr. Edward J. Villano worked under the direction of Professor Wayne A. Charlie.

This report has been reviewed by the Public Affairs Office (PA) and is releasable to the National Technical Information Service (NTIS). At NTIS, it is available to the general public, including foreign nationals.
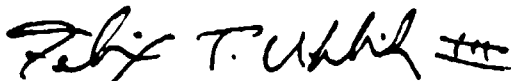
This technical report has been reviewed and is approved for publication.

Paul E. Sheppard, GS-13
Project Officer

W.S. Strickland, GM-14
Chief, Air Base Survivability
Section

Felix T. Uhlik, III, Lt Col, USAF
Chief, Air Base Systems Branch

TABLE OF CONTENTS

APPENDICES

LIST OF FIGURES

LIST OF FIGURES
(CONCLUDED)

LIST OF TABLES

LIST OF SYMBOLS

a = peak particle acceleration (g's)

a_c = centripetal acceleration (m/s^2)

b = y-intercept of regression line

c_c = seismic velocity (ft/s; m/s)

c_s = shear wave velocity (ft/s; m/s)

c' = effective cohesion intercept (kPa)

D = depth of overburden

d = peak particle displacement (ft; m)

E = elastic modulus (kPa)

e = void ratio

f = ground shock coupling factor

G_0 = shear modulus (kPa)

g = earth gravity force (1 g = 32.2 ft/s^2 = 9.81 m/s^2)

I = peak impulse (psi-s; kPa-s)

M = constrained modulus (kPa)

m = regression line slope

m_v = coefficient of volumetric compressibility (kPa)

N = number of g accelerations

n = attenuation coefficient

P = peak stress (psi; kPa)

p_c = capillary pressure (kPa)

R = distance to the explosive (ft; m)

r = radial distance from centrifuge axis (m)

r_m = curved water interface radius (m)

u = pore fluid pressure (kPa)

u_a = pore air pressure (kPa)

u_w = pore water pressure (kPa)

V = peak particle velocity (ft/s; m/s)

v = uniform circular velocity (m/s)

W = charge weight; charge mass (lb; kg).

$\dot{x}$ = particle velocity (m/s)

Δt = time increment (sec.)

ϵ = strain

θ = angular displacement

μ = Poisson's ratio

π = pi

ρ = mass density (lb-s^2/ft^4; kg/m^3)

ρc_o = acoustic impedance (lb-s/ft^3; kg/m^2-s)

σ = stress (kPa)

σ_a = total normal stress (kPa)

τ = shear stress (kPa)

ϕ^b = angle of shear strength increase with increase in matric

   suction (degrees)

ϕ' = effective angle of internal friction (degrees)

χ = soil suction ratio (Bishop's theory)

ψ = capillary stress (kPa)

SECTION I

INTRODUCTION

A. OBJECTIVE

The general objective of this research program is to determine the influence that the degree of saturation during compaction of sand has on blast-induced ground shock and stress wave propagation. Four specific objectives arise out of this general objective.

1. Develop empirical equations that accurately predict peak stresses, peak particle velocities, and peak particle accelerations in Tyndall beach and Ottawa 20-30 sands as a function of compactive saturation.

2. Compare centrifuge results with work on dynamically loaded sands from the split-Hopkinson pressure bar reported by Ross et al. (1988), Pierce et al. (1989) and Charlie et al. (1990).

3. Compare the validity of centrifuge results with those of full scale blasting by Drake and Little (1983).

4. Compare centrifuge results with unsaturated soil mechanic theory proposed by Fredlund (1985).

B. BACKGROUND

Blast loading of soils is of considerable importance to those concerned with buried structures because of the high intensity, high amplitude compressive stress waves produced. Compacted backfill, placed around and over a buried structure, transmits the blast induced stresses and thus determines the survivability and vulnerability of the structure.

Although Drake and Little (1983) conducted numerous blast tests and developed stress and ground motion prediction equations on various soils, there has not been a systematic explosive testing program conducted on

1

unsaturated sands. Laboratory research on sands by Ross et al. (1988), Pierce et al. (1989), and Charlie et al. (1990), utilizing the split-Hopkinson pressure bar, has shown that the degree of saturation during compaction is influential on dynamic stress wave velocity and stress transmission ratio.

C.   SCOPE

This report presents the results of systematic explosive testing on unsaturated Tyndall beach and Ottawa 20-30 sands. Our purpose is to determine the influence of moisture content during compaction on blast induced stress and ground motion response. Explosive events are carried out in small-scale models. A centrifuge is utilized to subject the models to increased accelerations such that prototype blast induced stresses can be simulated. Scaling laws are used to relate model and prototype performance.

Performing scaled model testing on the centrifuge allows prototype explosive events to be conducted at a fraction of the time and money required to perform large scale blast testing. Charge masses of 1031 mg and 350 mg of PBX 9407 are utilized to induce explosive loadings in models of 1/18.9 and 1/26.3 scale. Accelerating the models to 18.9 and 26.3 times the acceleration of earth's gravity results in scaled prototype charges of 6.9 kg and 6.4 kg respectively (7.8 kg and 7.3 kg TNT equivalent) detonated at a depth of burial of 1.4 meters.

SECTION II

LITERATURE REVIEW

This chapter briefly provides insight on the theories and principles involved in this research effort. These theories and principles are the basis for drawing conclusions in this report.

A. STRESS WAVES AND GROUND MOTIONS

1. Stress Wave Propagation

As a stress wave travels further from its source, the wave front becomes less curved and particles traveling in a direction away from the source are assumed to be parallel. Representing wave motions in this manor is known as one-dimensional, or planar wave propagation. Planar wave propagation and constrained modulus, M, can be related by considering a stress wave propagating down a bar. Derivation begins by using Newtons' Second Law of motion

$$F_x = m \, a_x \qquad (2.1)$$

where F_x represents an induced force on an element of the bar of mass m, and a_x is the acceleration of the element (Dowding, 1985). Applying this force over an elemental area of the bar results in the equation

$$\sigma = \rho \, c_c \, \dot{x} \qquad (2.2)$$

where σ is stress, ρ is the density of the material in the bar, c_c is the plane wave propagation velocity through the bar (or seismic velocity), and $\dot{x}$ is the velocity of the element, or particle velocity (Kolsky, 1963). The

3

quantity ρc_c in Equation (2.2) is commonly known as the acoustic impedance of the medium. Equation (2.2) predicts stress on the stress wave front of planar, spherical and cylindrical stress waves (Rinehart, 1975).

Considering elastic materials, strain can be expressed in terms of particle velocity and seismic velocity

$$\epsilon = \frac{\dot{x}}{c_c}. \tag{2.3}$$

Seismic velocity and constrained modulus can be related in the form

$$c_c = \sqrt{\frac{M}{\rho}}. \tag{2.4}$$

Similarly, shear wave velocity is expressed in terms of shear modulus, G_o

$$c_s = \sqrt{\frac{G_c}{\rho}} \tag{2.5}$$

(Rinehart, 1975). Shear modulus and constrained modulus are related to elastic modulus and Poisson's ratio, μ, with

$$G_o = \frac{E}{2(1 + \mu)} \tag{2.6}$$

and

$$M = \frac{E(1 - \mu)}{(1 + \mu)(1 - 2\mu)} \tag{2.7}$$

(Lambe and Whitman, 1969).

Seismic velocity is measured at strains below 10^{-4} percent and may be used as a crude index for predicting stress wave propagation. Generally, low seismic velocity is associated with low relative density and indicates poor stress wave transmission. Wave attenuation can be described as the change in peak stress, peak particle velocity, or peak particle acceleration with time or distance and is greatest among low density soils. Attenuation coefficients, n, are determined from the slopes of least squared regression lines of blast data when plotted on log-log scale. Table 2.1 shows ground shock parameters for sands of various saturation and relative density and determined from several hundred

4

Table 2.1 SOIL PROPERTIES FROM EXPLOSIVE TESTING IN SAND BY DRAKE AND LITTLE (1983).

Soil Description	Dry Mass Density ρ_d (kg/m³) (1)	Total Mass Density ρ (kg/m³) (2)	Air-Filled Voids % (3)	Percent Saturation % (4)	Seismic Velocity c (m/s) (5)	Acoustic Impedance ρc (kg/m²-s) (6)	Attenuation Coefficient n (7)
Loose, dry, poorly-graded.	1281	1441	>30	31	183	262	3-3.5
Loose, wet, poorly-graded, free standing water.	1553	1857	10	76	152-183	283-339	3
Dense, dry, poorly-graded.	1585	1665	32	20	274-396	566	2.5-2.75
Dense, wet, poorly-graded, free standing water.	1729	1986	9	74	305	498	2.75
Very dense, dry, relative density = 100%.	1681	1745	30	17	488	995	2.5

explosive tests by Drake and Little (1983). Seismic velocities are shown in column five (5) of Table 2.1, and acoustic impedance and attenuation coefficients are shown in columns six (6) and seven (7).

2. Charge Mass and Distance Relationship

To analyze blasting data when charge mass, W, and distance, R, from the blast vary, a scaling technique relating the two variables is useful. Two common approaches are the cubed root scaling, $R/W^{1/3}$, and the square root scaling, $R/W^{1/2}$ (Dowding, 1985). Cubed root scaling is based on explosive charge distribution of spherical form, and square root scaling assumes a cylindrical explosive. Throughout this report the cubed root scaling technique will be used.

3. Ground Shock Coupling Factor

The magnitude of blast-induced stresses and ground motions is greatly enhanced as a weapon penetrates more deeply into the soil before it detonates. The ground shock coupling factor, f, is a relationship of blast energy transmitted to the surrounding medium. It is defined as the ratio of the ground shock magnitude from a partially buried or shallow weapon, to that from a fully buried weapon in the same medium. Figure 2.1 shows ground shock coupling factors as a function of scaled depth for blasts in air, soil, and concrete (Drake and Little, 1983). Depth of burial is meas... ... ... center of mass of the explosive.

4. Ground Shock Prediction Equations

Free-field stresses and ground motions can be characterized by rapidly decaying exponential time histories that decay monotonically, or attenuate, as they propagate outward from the explosion. These attenuating ground motions can be represented by a straight line when the data is plotted on log-log scale. The equation for a line on log-log scale has the form

6
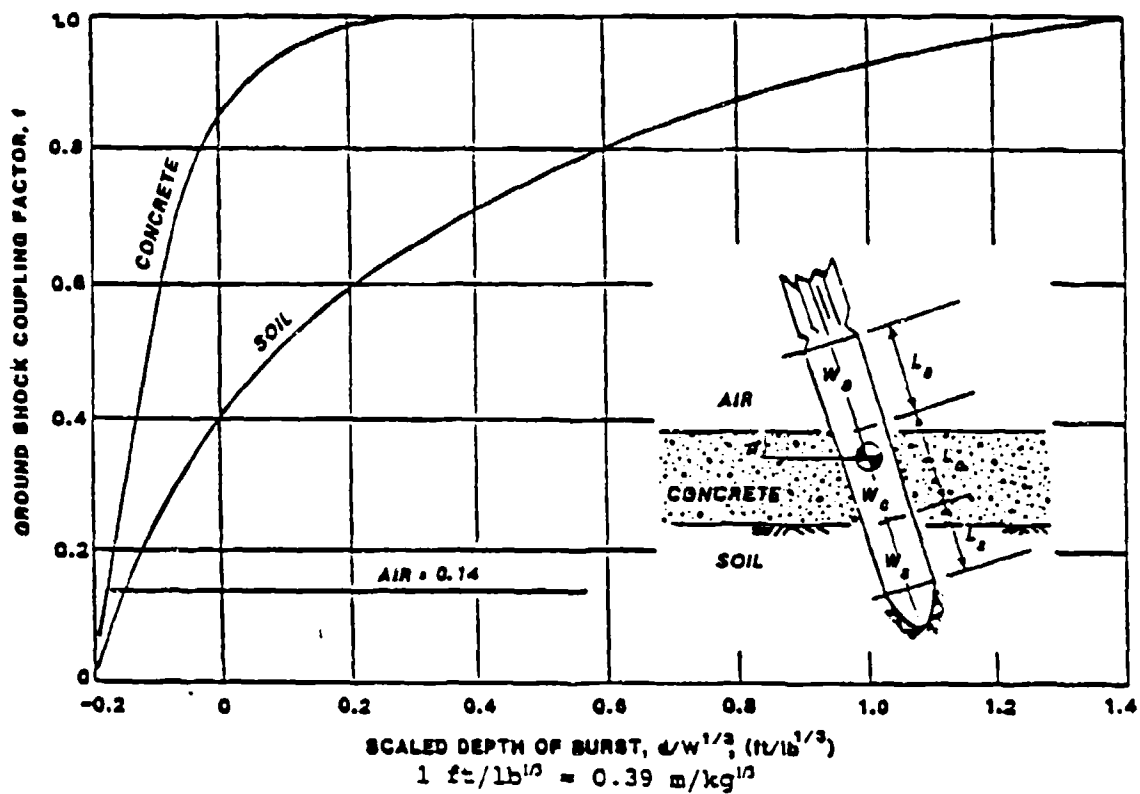
Figure 2.1   Ground shock coupling factor as a function of scaled depth of burst for air, soil, and concrete (From Drake and Little, 1983).

$$\log y = m \log x + \log b \qquad (2.8)$$

where y is the ordinate (i.e. peak stress, peak particle acceleration, or peak particle velocity), and x is the abscissa or scaled distance from the charge. The constants m and b represent the slope of the line and y-intercept of the line (at a scaled distance of one on log-log scale) respectively. The inverse log of Equation 2.8 results in an equation of the form

$$y = b \, x^a. \qquad (2.9)$$

Free-field stress and ground motion data presented by Drake and Little (1983) is in the form of Equation (2.9). Equations for peak stress (P), peak particle velocity (V), peak particle acceleration (a), peak particle displacement (d), and impulse (I), are as follows:

$$P = f \, \frac{160}{144} \, \rho c_c \left(\frac{R}{W^{1/3}} \right)^{-n} \quad (psi) \qquad (2.10a)$$

$$P = f \, 0.049 \, \rho c_c \left(2.52 \frac{R}{W^{1/3}} \right)^{-n} \quad (kPa) \qquad (2.10b)$$

$$V = f \, 160 \left(\frac{R}{W^{1/3}} \right)^{-n} \quad (ft/s) \qquad (2.11a)$$

$$V = f \, 49 \left(2.52 \frac{R}{W^{1/3}} \right)^{-n} \quad (m/s) \qquad (2.11b)$$

$$a \, W^{1/3} = f \, 50 \, c_c \left(\frac{R}{W^{1/3}} \right)^{-n-1} \quad (g's\text{-}ENGLISH) \qquad (2.12a)$$

$$a \, W^{1/3} = f \, 126 \, c_c \left(2.52 \frac{R}{W^{1/3}} \right)^{-n-1} \quad (g's\text{-}SI) \qquad (2.12b)$$

8

$$\frac{d}{W^{1/3}} = f \; 500 \; \frac{1}{c} \left(\frac{R}{W^{1/3}}\right)^{-n+1} \quad (ft) \qquad\qquad (2.13a)$$

$$\frac{d}{W^{1/3}} = f \; 60 \; \frac{1}{c} \left(2.52\frac{R}{W^{1/3}}\right)^{-n+1} \quad (m) \qquad\qquad (2.13b)$$

$$\frac{I}{W^{1/3}} = f \; \rho \; 1.1 \left(\frac{R}{W^{1/3}}\right)^{-n+1} \quad (psi\text{-}s) \qquad\qquad (2.14a)$$

$$\frac{I}{W^{1/3}} = f \; \rho \; 0.19 \left(2.52\frac{R}{W^{1/3}}\right)^{-n+1} \quad (kPa\text{-}s) \qquad\qquad (2.14b)$$

where

a = peak particle acceleration (g's);

c_c = seismic velocity (ft/s; m/s);

d = peak particle displacement (ft; m);

f = ground shock coupling factor;

g = earth gravity force (1 g = 32.2 ft/s^2 ≈ 9.81 m/s^2);

I = peak impulse (psi-s; kPa-s);

n = attenuation coefficient;

P = peak stress (psi; kPa);

R = distance to the explosive (ft; m);

ρ = mass density (lb-s^2/ft^4; kg/m^3);

ρc_c = acoustic impedance (lb-s/ft^3; kg/m^2-s);

V = peak particle velocity (ft/s; m/s); and

W = charge weight; charge mass (lb; kg).

By setting ρc_c to units of lb-s/in^2-ft, Equations (2.10a) and (2.11a) can be combined with the common term $f160(R/W^{1/3})^{-n}$ to yield

$$P = \rho \; c_c \; V. \qquad\qquad (2.15)$$

Equation 2.15 is the same as Equation (2.2) shown earlier.

9

B.   UNSATURATED SANDS

1.   Stress Wave Propagation in Unsaturated Sands

Currently, there are no theoretical, empirical or numerical methods that predict stress or ground motion behavior in cohesionless soil as a function of saturation. Most field specifications for cohesionless soil placement is based on the assumption that saturation has little or no influence on the dynamic behavior of the soil.

Ross et al. (1988) and Pierce et al. (1989) performed high-amplitude split-Hopkinson pressure bar (SHPB) tests on Eglin and Ottawa 20-30 sands. They determined that moisture content and capillary pressure during compaction and testing were important in predicting wave velocity and stress wave transmission. The results of Ross et al. (1988) showed that, for sands compacted moist to a constant dry density, wave velocity and stress transmission increased as the saturation was increased from 0 to 20 percent, remained steady to 70 percent saturation, and then decreased (Figures 2.2(a), (b), (c), and (d)). Pierce et al. (1989) conducted similar tests to those of Ross et al. (1988) except that the specimens were compacted both moist to a constant dry density, and compacted dry to a constant density, then wetted. Pierce et al. (1989) results for Eglin sand compacted moist (Figures 2.2(b) and (d)) are similar to those obtained by Ross et al. (1988), and results for specimens compacted dry (Figures 2.2(e), (f), (g), and (h)) indicate little change in wave velocity and stress transmission with saturation.

Similar results were reported by Charlie et al. (1990) from SHPB tests conducted on silica 50/80 sand compacted moist to a constant dry density. Transmitted stresses increased from 0 to approximately 20 percent saturation, then decreased with increasing saturation (Figure 2.3(a)). Wave velocities, however, remained steady to approximately 70 percent saturation, then decreased with increased saturation (Figure 2.3(b)). They concluded that both water content and dry density need to be controlled during compaction if stress transmission and attenuation are critical.

10
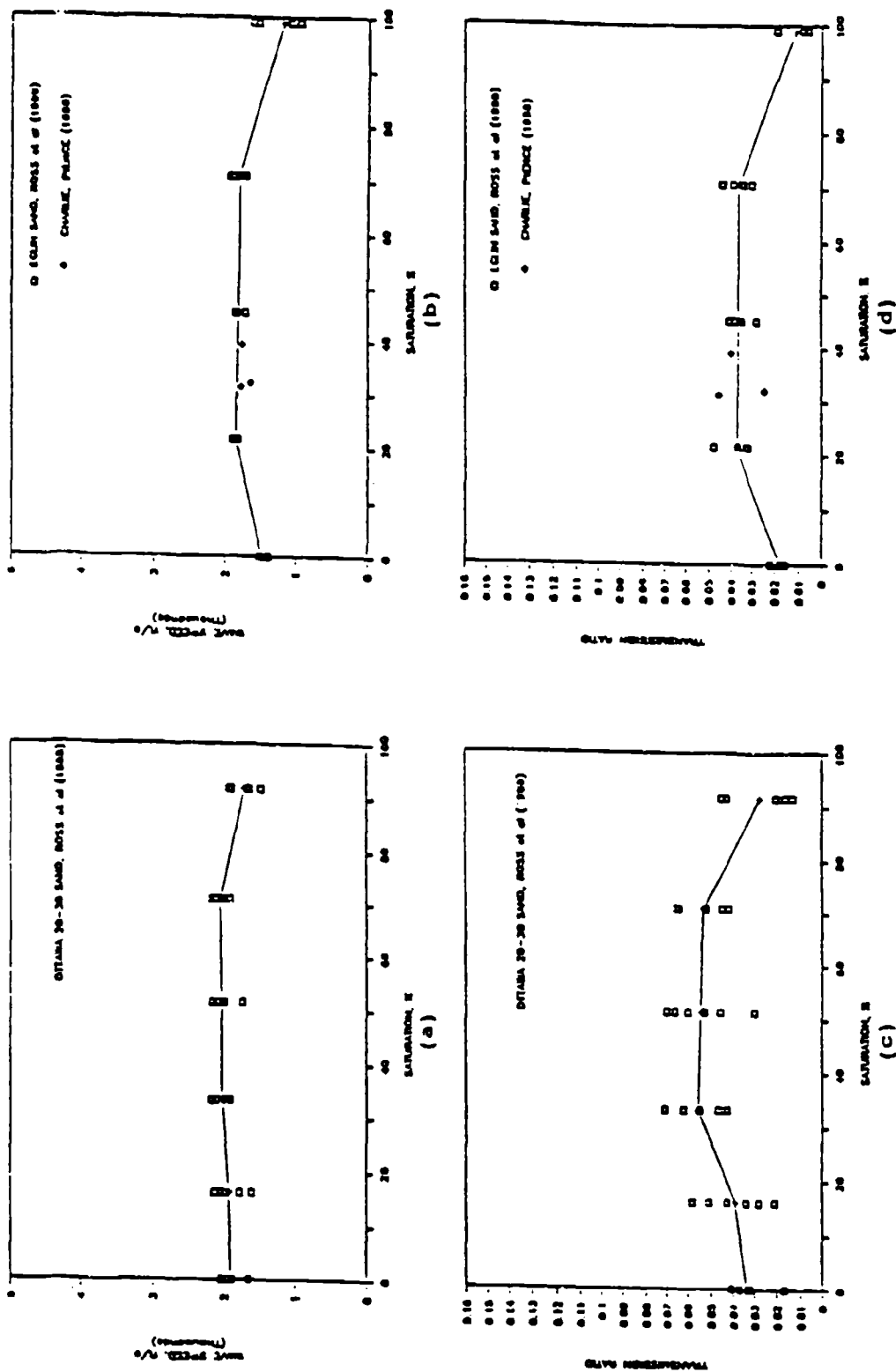
Figure 2.2 Results obtained by Ross et al. (1988) and by Pierce et al. (1989) on Eglin and Ottawa sands compacted moist. (a) Ottawa wave speed. (b) Eglin wave speed. (c) Ottawa transmission ratio. (d) Eglin transmission ratio. Results of Pierce et al. (1989) taken from Charlie and Pierce (1988).

11
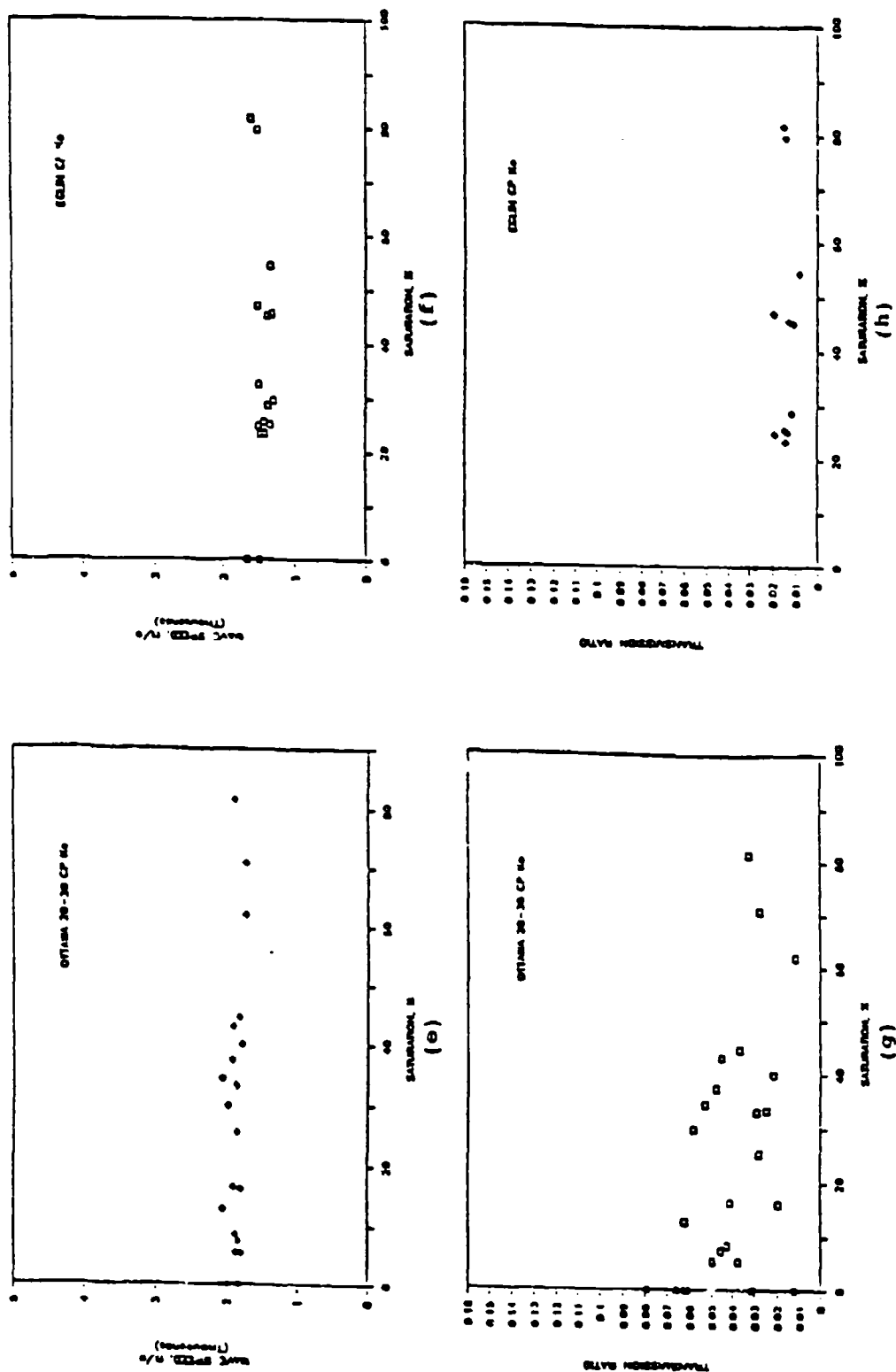
Figure 2.2 (continued) Results obtained by Pierce et al. (1989) on Eglin and Ottawa sands compacted dry. (e) Ottawa wave speed. (f) Eglin wave speed. (g) Ottawa transmission ratio. (h) Eglin transmission ratio. Results of Pierce et al. (1989) taken from Charlie and Pierce (1988).

12
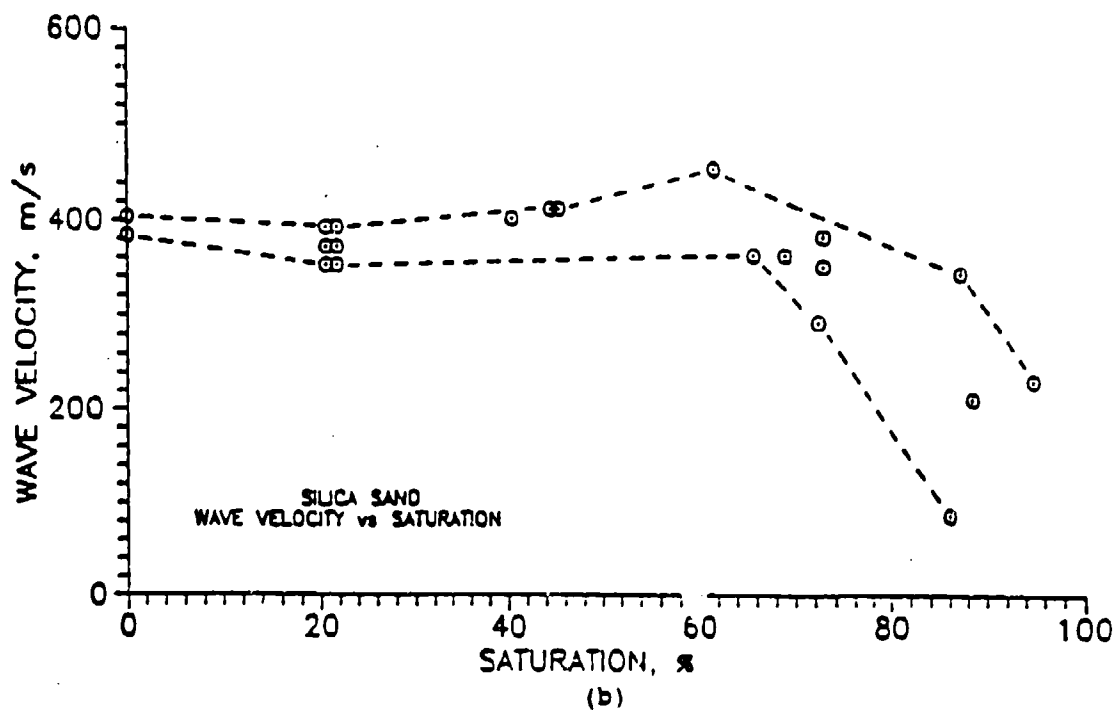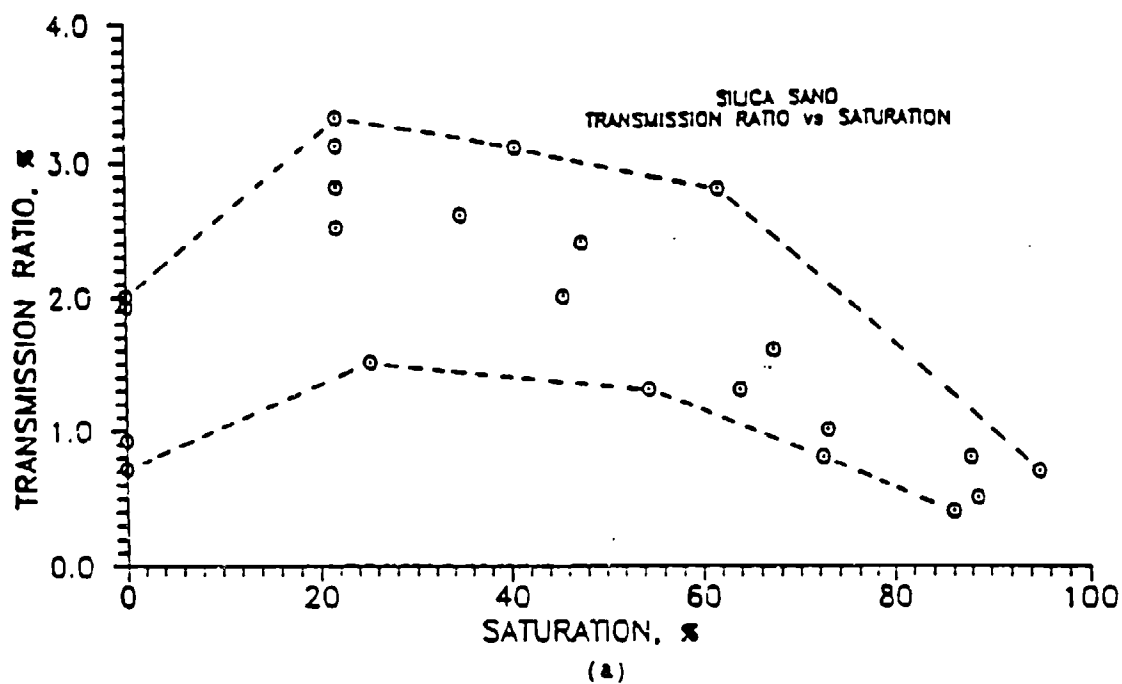
Figure 2.3   Results obtained by Charlie et al. (1990) on Silica 50/80
             sand.   (a) Stress transmission ratio.   (b) Wave velocity.

13

Charlie and Walsh (1990) conducted one-dimensional (planar) blast testing in soil models on the centrifuge simulating full scale blast events. Wave velocity results showed an increase from 0 to 20 percent saturation, remained steady to 60 percent saturation, and then decreased (Figure 2.4). Unpublished results of average peak stress for various scaled depths and explosive mass are shown in Figure 2.5. The general trend is an increase in peak stress as saturation increases from 0 to 40 or 60 percent, then peak stresses decrease as saturation increases to 80 percent.

Veyera and Fitzpatrick (1990) examined the relationship between compaction moisture content, soil microstructure and dynamic stress transmission from tests conducted on the SHPB for Ottawa 20-30 sand. They found that the compactive energy required to obtain constant dry density is strongly dependent on the amount of moisture present during compaction (Figure 2.6). They attribute this to the formation of preferred particle orientation and capillary pressure during compaction.

Dynamic shear modulus, G_0, is a principal soil property required for evaluation of wave propagation in fine grained cohesionless soils. Wu et al. (1984) determined the significance of capillarity effects on shear modulus and the effective grain size D_{10}. Results showed a significant increase in shear modulus when the soils were compacted moist to a constant dry density. These effects were greatest among soils having the smallest grain diameter. Resonant column tests on glacier way silt (Figure 2.7) show that shear modulus displays a definite peak between 10 and 20 percent saturation and for various confining pressures. This increase in G_0 is a result of an increase in shear wave velocity.

2. Effective Stresses in Unsaturated Sands

Stress transmission is inherently related to interparticle contact and normal contact stress. Shukla and Prakash (1988) have conducted blast-induced stress wave propagation tests in plate specimens
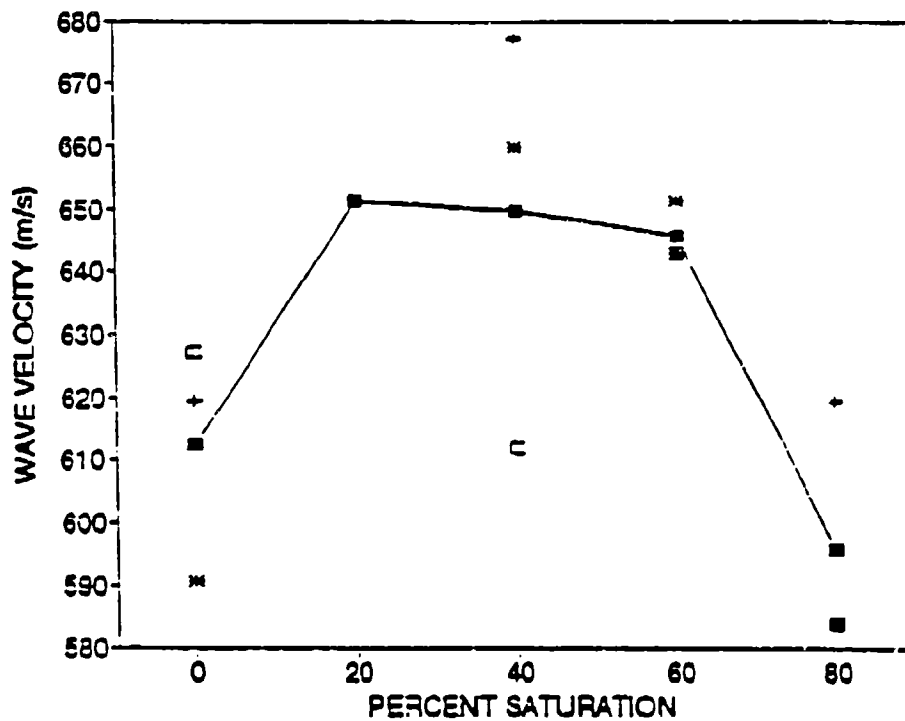
Figure 2.4   Average wave velocity results obtained by Charlie and Walsh
(1990) on Tyndall beach sand.
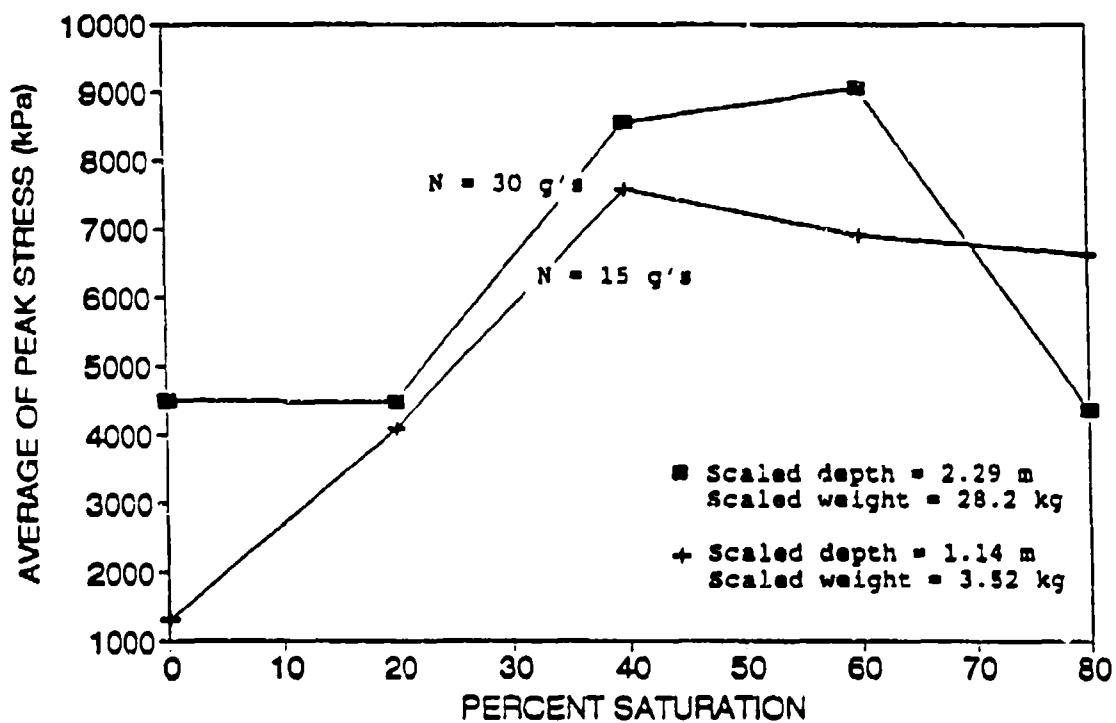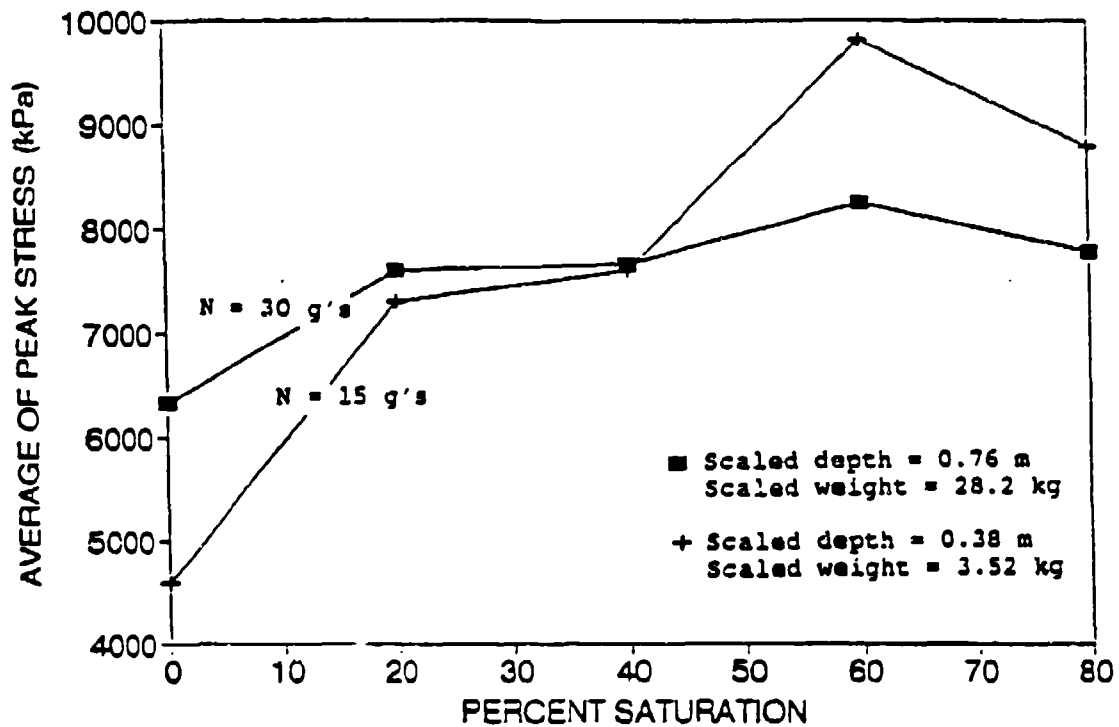
Figure 2.5 Average peak stress as a function of saturation from unpublished centrifuge results on Tyndall beach sand by Charlie and Walsh (1990).
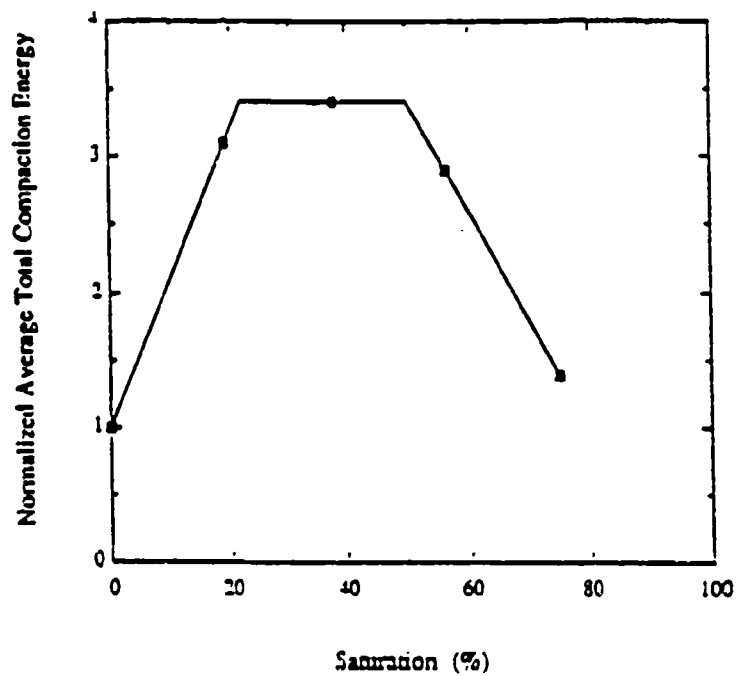
Figure 2.6 Normalized average total compactive energy for Ottawa 20-30 sand compacted to a dry density cf 1715 kg/m³ (From Veyera and Fitzpatrick, 1990).
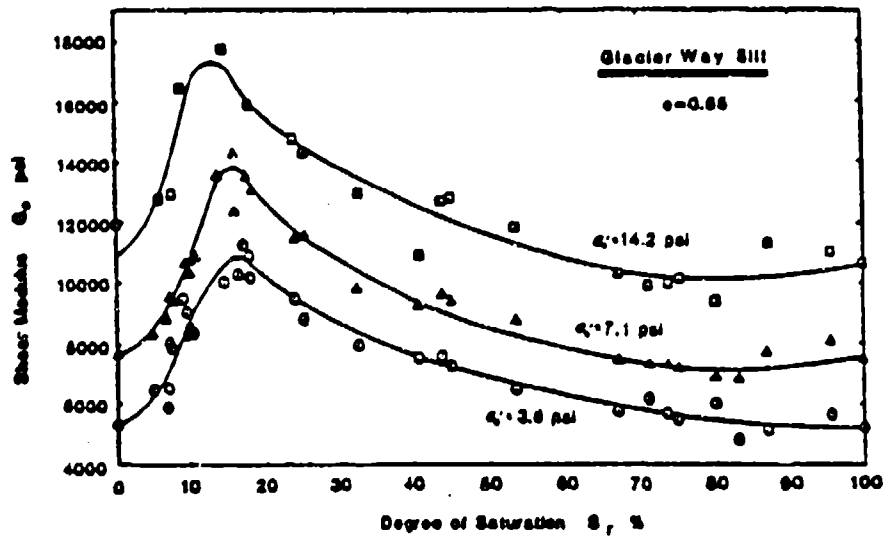
Figure 2.7 Shear modulus results from resonant column tests on Glacier way silt (From Wu et al., 1984).

17

and have shown that wave speed drops with increasing porosity. They go on to conclude that wave velocity shows a strong dependence on the microstructure of the porous media.

Stress waves are transmitted through the soil skeleton across the small mineral contacts. The response of a soil mass to changes in compressive stress depends a great deal on the intergranular stresses.

The equation for effective stress, developed by Terzaghi (1943), has the form

$$\sigma' = \sigma - u \qquad (2.16)$$

where σ' denotes effective stress, σ is the normal stress, and u is the pore fluid pressure. In the case of partially saturated soil where pore spaces contain two fluids, (water and air), Bishop et al. (1960) extended the conventional equation to the form:

$$\sigma' = (\sigma - u_a) + \chi(u_a - u_w). \qquad (2.17)$$

Here u_a and u_w represent pore air and pore water pressures respectively, and χ is an empirical parameter representing the proportion of the soil suction $(u_a - u_w)$ that contributes to the effective stress. For fully saturated soils χ is unity, and for dry soils χ is zero. Bishop et al. (1960) suggests that the value of χ depends mainly on the degree of saturation and to a lesser degree soil structure, cycle of wetting and drying, and external stress changes. Blight (1967) stated that the main drawback of Equation (2.20) is the difficulty of evaluating χ.

3.   Influence of Capillarity

Knowledge of the configuration of air and water in the interstices of the soil mineral skeleton helps to understand the influence of capillarity on effective stress. Height of capillary rise in soil above the water table depends mainly on effective grain diameter, whether the water is draining or imbibing, and to some extent particle shape (Holtz and Kovacs, 1981). Pore water above the groundwater table in unsaturated soil has a negative pressure with respect to air pressure.

18

Bulking of soil is a result of capillarity and forms a very loose relative density soil structure. Holtz and Kovacs (1981) describe how sands under certain deposition conditions can form a honeycomb structure as a result of bulking (Figure 2.8). Individual soil particles in this unsaturated soil structure are held together by capillary stress. The capillary stress is formed at the air and water interface and results in interparticle stress (Figure 2.9).

McWhorter and Sunada (1977) describe capillary stress, or interfacial tension (ψ) between soil particles as a force that opposes pressure differences in the pore water and local air pressure. Interfacial tension is measured as force per unit length acting along the perimeter of the interface in a direction tangent to the curved water surface.

Matric suction, or capillary pressure p_c as defined by McWhorter and Sunada (1977) is the difference between the air and water pressure ($u_a - u_w$) in the soil pore spaces. Capillary pressure and interfacial tension are related by

$$p_c = \frac{2 \psi}{r_m}$$
(2.18)

where r_w represents the radius of the curved water interface (Figure 2.9). Equation 2.18 predicts that the capillary pressure increases with decreasing saturation because of a reduction in r_m.

4.   Shear Strength and Volume Change of Unsaturated Soil

The science for unsaturated soils was slow to develop until its appearance by Bishop in the late 1950's. Fredlund (1985) summarizes shear strength and volume change equations of unsaturated soil.

Terzaghi's (1943), classic shear strength equation for saturated soil is written in terms of effective stress parameters from the effective Mohr-Coulomb failure envelope
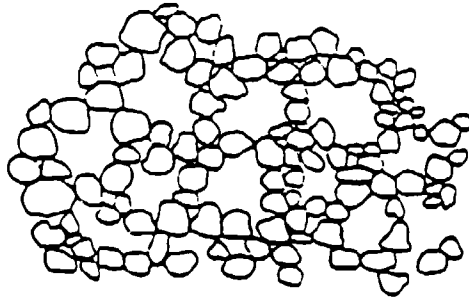
Figure 2.8   Honeycomb structure as a result of bulking in sand (From Holtz and Kovacs, 1981).
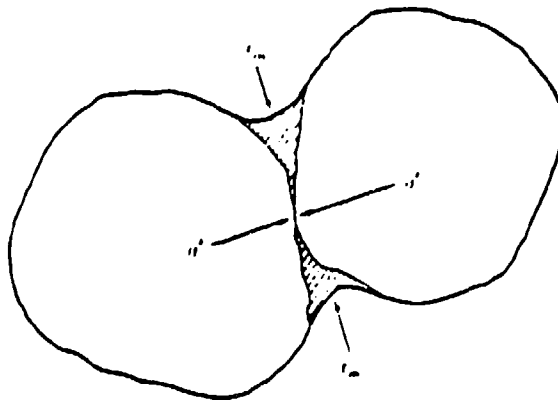
Figure 2.9   Soil grains held together due to capillary stress (From Holtz and Kovacs, 1981).

$$\tau = c' + (\sigma_n - u_w) \tan \phi' \qquad (2.19)$$

where

τ = shear stress;

c' = effective cohesion intercept;

σ_n = total normal stress;

u_w = pore water pressure; and

ϕ' = effective angle of internal friction.

Fredlund (1981) revised the shear strength equation for unsaturated soil to the form

$$\tau = c' + (u_a - u_w) \tan \phi^b + (\sigma_n - u_a) \tan \phi'. \qquad (2.20)$$

where u_a is the pore air pressure, and ϕ^b is the angle of shear strength increase with an increase in matric suction, $(u_a - u_w)$. Values for ϕ^b are consistently less than ϕ' and are on the order of 15 degrees (Fredlund, 1985).

Equation (2.20) can be interpreted as having two cohesion terms. The second of these cohesion terms, apparent cohesion, is a function of matric suction, $(u_a - u_w) \tan \phi^b$. Apparent cohesion is represented by a third dimensional extension of the Mohr-Coulomb failure criteria shown in Figure 2.10. When matric suction goes to zero, apparent cohesion becomes zero and the shear strength is reverted back to the saturated state of Equation 2.19. Equation (2.20) allows a smooth transition between saturated and unsaturated soils (Fredlund, 1985).

The three dimensional failure region developed by Fredlund (1981) is planar due to a linear increase in ϕ^b and ϕ' (Figure 2.10). The shear strength of a particular soil can be easily located on this plane if $(u_a - u_w)$ and $(\sigma - u_a)$ are known.

The classic volume change constitutive relation in terms of compressibility for saturated soils is
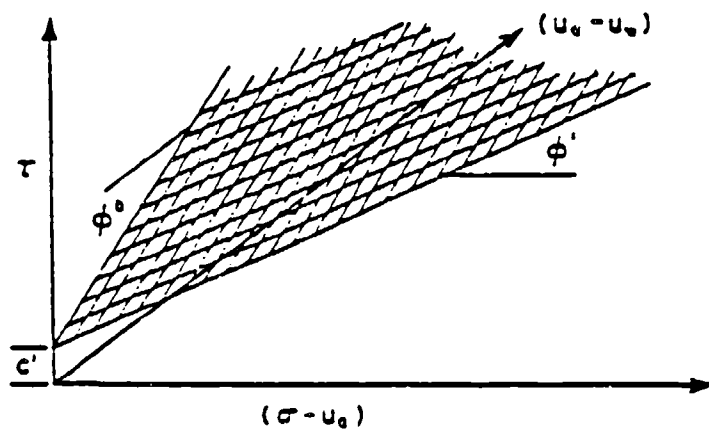
Figure 2.10   Three-dimensional extended Mohr-Coulomb failure surface (From Fredlund, 1985).

22

$$\epsilon = m_v \, d(\sigma - u_w) \tag{2.21}$$

where ϵ is volumetric strain ($\epsilon_x = \epsilon_y = \epsilon_z$), and m_v is the coefficient of volume compressibility. The coefficient of volume compressibility is simply the inverse of the constrained modulus, M.

The compressibility constitutive equation for unsaturated soil is

$$\epsilon = m_1^s \, d(\sigma - u_a) + m_2^s \, d(u_a - u_w) \tag{2.22}$$

where m_1^s is the compressibility of the soil structure with respect to a change in $(\sigma - u_a)$, and m_2^s is the compressibility with respect to a change in $(u_a - u_w)$ (Fredlund, 1985).

Equation (2.22) utilizes matric suction similar to the shear strength equation. The stress variable, again, yields a smooth transition to the saturated case of Equation (2.21) when the absolute pore pressure is zero.

5. Unsaturated Soil Placement

Holtz and Kovacs (1981) describe an "end-product" earthwork specification that states as long as the contractor is able to obtain the specified relative compaction, it doesn't matter how it is obtained, nor the equipment he uses. Earthwork specifications for compaction of sands are generally of this type in that only the final dry density is specified. Laboratory tests to determine the behavior of sand backfill are generally conducted in this manor as well. The design assumption is that moisture content during compaction does not effect the dynamic behavior of unsaturated sands.

C. CENTRIFUGE MODELING

1. Historical Background

The earliest engineering use of a centrifuge was introduced in 1869, by a Frenchman named Phillips, who simulated self-weight stresses of structural beams. His tests were relatively insignificant, however, and the concept of increased gravity for modeling soil and rock did not come to its fruition until 1931 by an American named Bucky. Bucky developed

23

the technique of simulating self-weight stresses in mines. At the same time in Russia, Pokrovsky developed the centrifuge technique to determine the stability of slopes in river banks. Through the 1950's, centrifuge testing in the U.S. remained confined to mining applications. In 1966, Schofield and his colleagues at the University of Cambridge built a prototype geotechnical centrifuge. In 1969, Schofield built a 1.5 meter geotechnical centrifuge at the University of Manchester Institute of Science and Technology. Then in 1976 Schmidt and Schofield began dynamic work on explosive cratering. Schmidt and Holsapple are predecessors for the development of explosive testing to simulate nuclear explosives.

At this time several centrifuge facilities were located throughout the U.S. and centrifuge techniques were becoming more accepted. Japan, Denmark, Sweden, Netherlands, and France developed centrifuge modeling facilities as well. In 1979, modification of a large centrifuge began at the NASA Ames Research Center in order to make it the largest capacity centrifuge in the U.S.

Today, state of the art centrifuge testing is practical and well accepted world wide for most static applications. However, there is a considerable amount of research to be conducted to further develop simulation of dynamic events.

2.   Principles of Centrifuge Modeling

Gravity effects are important during scaled model testing in order to simulate conditions that properly replicate the prototype. An artificial gravitational field is the answer to this problem, and the centrifuge is the most convenient tool to achieve this requirement. Prototype throughout this report refers to a system that exists at one g.

In order to properly simulate gravity induced stresses, it is necessary to test an Nth scale model in a gravity field N times stronger (N g's) than that experienced by the prototype at one g. Thus, a model can be constructed of height 1/N the height of the prototype and obtain similar overburden stresses when the model is accelerated at N g's. To achieve required accelerations from the centrifuge, the scaled model

24

travels in a circular path with uniform circular velocity, v, as shown in Figure 2.11. Uniform circular velocity of a point in the model over a period of time, Δt, is given by

$$v = \frac{\theta \, r}{\Delta t} \qquad (2.23)$$

where θ is the angle displaced over Δt, and r is the radius of the path of a point in the model. Points in the model are accelerated in a direction toward the axis of the centrifuge with the magnitude

$$a_c = \frac{v^2}{r} \qquad (2.24)$$

where a_c is the centripetal acceleration. Relative to the model itself is an acceleration acting away from the axis equal in magnitude and is termed centrifugal acceleration. The number of g's (N) at which the model is accelerated can be expressed as

$$N = \frac{a_c}{g}. \qquad (2.25)$$

a.   Buckingham Pi Theory

The physical parameters of a model at a particular g level and the respective parameters of a prototype are related through principles known as scaling laws. Scaling laws are necessary so that model parameters can be extrapolated to represent prototype performance (Kline, 1965). These scaling laws are developed through the principles of dimensional analysis and utilize a method known as the Buckingham Pi Theory (Buckingham, 1915).

The Buckingham Pi Theory is a powerful technique that non-dimensionalizes the parameters of a physical system. These non-dimensional quantities are known as pi (π) terms and can be related outside the context of the physical system with similar quantities of another physical system (i.e. relating the physical system of a model with that of a prototype). Scaling laws are then developed which relate the two systems. Scaling relations for centrifuge modeling are given in Table

25
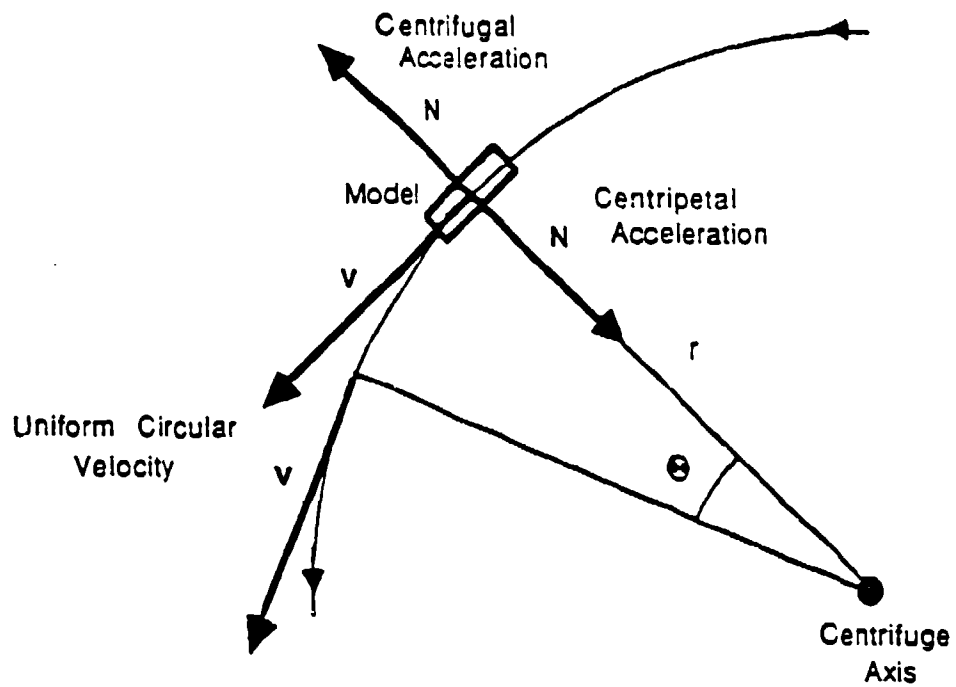
Figure 2.11   Circular path of uniform circular velocity on the centrifuge.

2.2. Derivation of scaling laws and further detail of the Buckingham Pi Theory are provided in APPENDIX A.

b. Modeling of Models

Scaling laws can become very complicated when several parameters interact with one another resulting in distortion of the model. In order to prevent this, one must verify the scaling assumptions, and this is best accomplished by full scale testing of the prototype. Prototype testing can be very costly, however, and sometimes impossible. As an alternative, the concept of "modeling of models" provides a check on the consistency of centrifuge modeling.

Modeling of models is illustrated by Ko (1988) in Figure 2.12 where the model size is plotted against the gravity level on log-log scale. Consider a 1000 cm prototype at point A1. If the prototype is modeled at 1/10 scale, the dimensions become 100 cm at 10 g's (A2), or at 1/100 scale the dimensions become 10 cm at 100 g's (A3). Points A2 and A3 are models of A1 and are also models of each other. To verify that the performance of the models simulates the prototype, A2 and A3 can be compared to one another in the absence of the prototype.

3. Limitations of Models

Before conducting model testing, the applicable scale to be used must be evaluated outside of the scaling laws and theory of multiple gravity testing. The physical limitations of the modeling material plays a critical role in the determination of scale. Using the same soil material to construct both the model and prototype is a great advantage when conducting centrifuge modeling. By doing this, the complex modeling of constitutive soil properties can be avoided. Furthermore, homologous points in the geometrically similar model and prototype will be subjected to similar stresses, and thus will develop the same strains (Schmidt, 1981; and Ko, 1988).

Table 2.2   STANDARD SCALING LAWS (FROM BRADLEY ET AL., 1984).

N = NUMBER OF G ACCELERATIONS

QUANTITY	PROTOTYPE	MODEL
LINEAR DIMENSION	1	$1/N$
GRAVITY (g)	1	N
AREA	1	$1/N^2$
VOLUME	1	$1/N^3$
DYNAMIC TIME	1	$1/N$
VELOCITY (DISTANCE/TIME)	1	1
ACCELERATION (DISTANCE/TIME^2)	1	N
DENSITY (MASS/VOLUME)	1	1
UNIT WEIGHT (FORCE/UNIT VOLUME)	1	N
FORCE	1	$1/N^2$
STRESS (FORCE/AREA)	1	1
MASS	1	$1/N^3$
ENERGY	1	$1/N^3$
STRAIN (DISPLACEMENT/UNIT LENGTH)	1	1
HYDRODYNAMIC TIME	1	$1/N^2$
IMPULSE	1	$1/N^3$
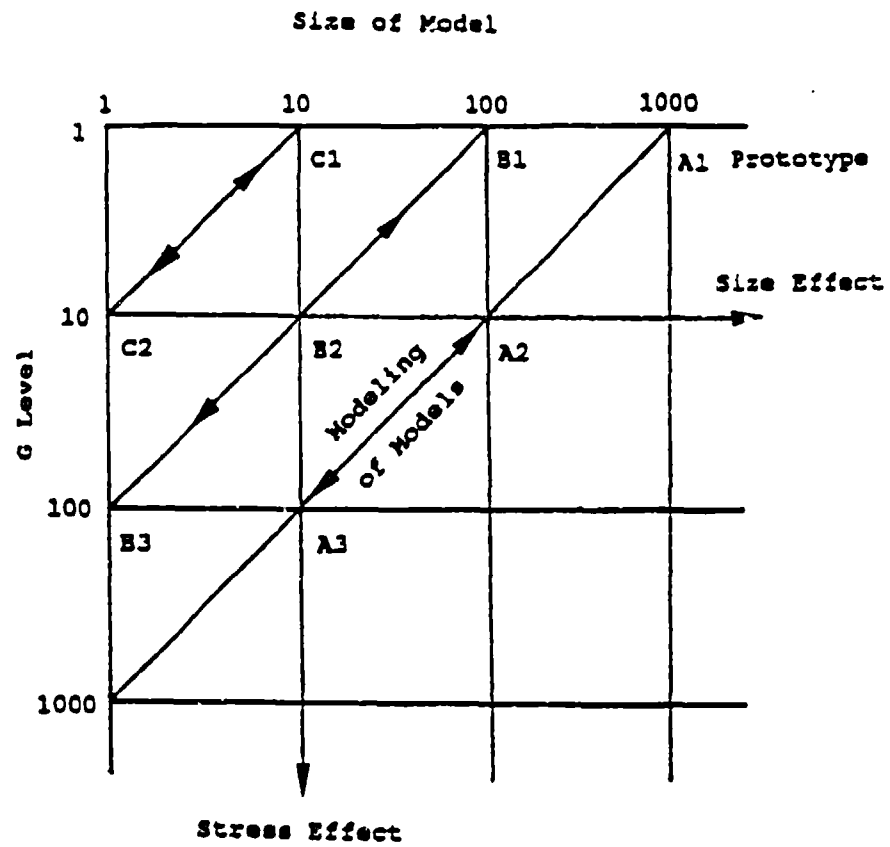
Figure 2.12 Graphical representation of "modeling of models" (Ko, 1988).

Although scaling theory suggests that particle size should be scaled with g's, perturbations from similar model-prototype materials have proven insignificant as long as the grain size is maintained much smaller than adjacent structure elements. Bradley et al. (1984) reports that a simple reduction in particle size has proven unsatisfactory due to the complex interrelationship of soil strength and response to particle size. Testing based on "modeling of models" can provide guidelines for limitations arising from grain size effects.

Model constructability depends upon the limitations of the centrifuge facility. As discussed earlier, centrifugal acceleration in the model is dependent on radial distance from the center of rotation. Thus, stresses vary nonlinearly with depth in the model because of the difference in centrifugal force with depth. This can complicate model behavior unless the radius arm to the model is sufficiently large with respect to model depth. A similar problem exists with a difference in stresses in a horizontal plane of the model due to differences in radial distance from the center of rotation. Again, stress differences are minimized with a sufficiently large centrifuge radius.

Finally, scaling of instrumentation size and mass is just as important as scaling of the model itself. Instruments used to measure modeling events are often too large to adequately represent prototype behavior at homologous points. Therefore, it is imperative that the presence of these instruments do not adversely affect the model behavior. Miniature transducers are needed to obtain a soil-instrument likeness in scaled size.

SECTION III

EXPERIMENTAL INVESTIGATION

A. CENTRIFUGE FACILITY, INSTRUMENTATION AND EXPLOSIVES

1. Description of the Centrifuge

The centrifuge used to conduct the experimental phase of this research is a Genisco (model E185, Serial Number 11) located at HQ AFCESA/RACS, Tyndall Air Force Base, Florida (Figure 3.1). The capacity of the centrifuge is 13.6 metric g-tons at a maximum acceleration of 100 g's and radius of 1.83 meters. Thus, at its maximum acceleration of 100 g's, a load of 136 kg can be applied to each of the two payload platforms. The centrifuge is rotated by a variable speed hydraulic motor regulated from the control console shown in Figure 3.2.

The centrifuge consists of two symmetrical cantilever arms opposite of one another, each of which supports a 76 cm square payload platform. The specimen payload is attached to one platform while counter balance weight of equal mass is placed on the opposite platform. While the centrifuge is in flight, an automatic dynamic balancing motor equalizes payload masses of less than 4.53 kg. The rotation rate of the centrifuge is indicated on a digital tachometer located on the control console (Figure 3.2).

2. Instrumentation

a. Carbon piezoresistive stress gages

Stress time histories generated by the blast are measured with 1/8 watt 1000 ohm (+5% tolerance) carbon resistors manufactured by Allen Bradley (Figure 3.3). These resistors were selected

31
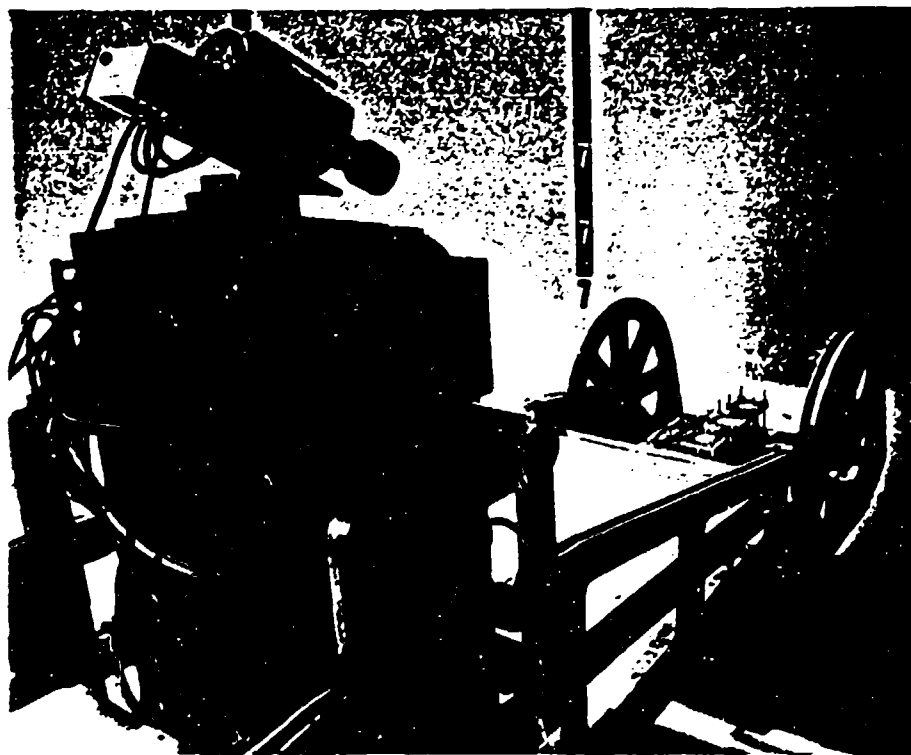
Figure 3.1   Centrifuge located at Tyndall Air Force Base.
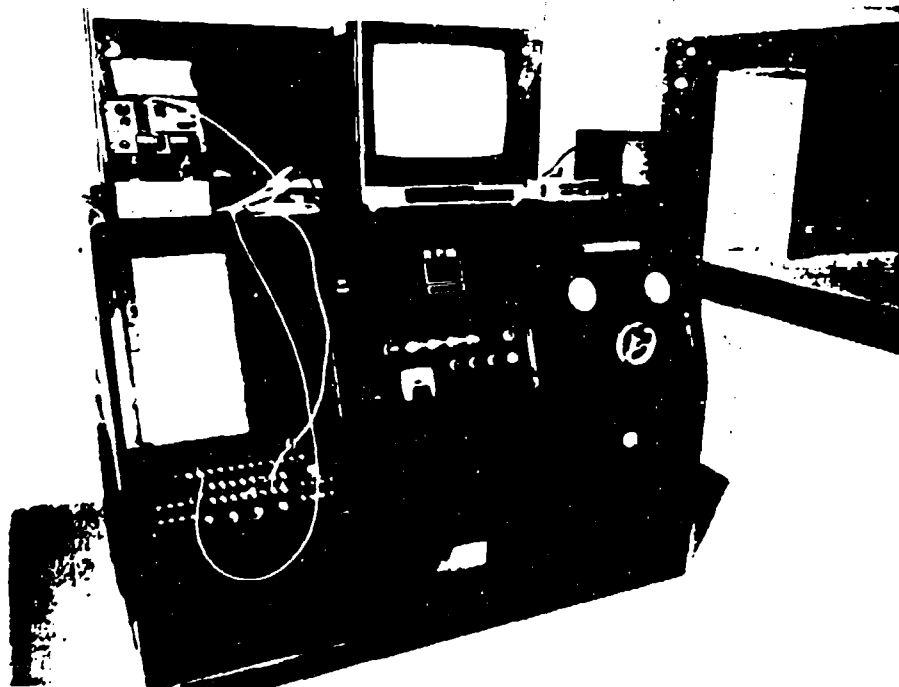
Figure 3.2   Control console for operation of the centrifuge.

Figure 3.3   Carbon piezoresistive stress gage.

34

for their small size (1.58 mm in diameter and 4.00 mm in length) and their ability to represent a point measurement. In addition, carbon resistors are readily available, can be statically calibrated, and are inexpensive.

Carbon stress gages are configured as Wheatstone bridges and have four carbon resistors (Figure 3.4). The active arm of the gage, R_1, is located in the specimen, while the remaining bridge arms are mounted outside the specimen on the centrifuge. All resistors are nominally equal to one another (i.e. $R_1=R_2=R_3=R_4$). Operation of the bridge utilizes the stress-resistance characteristics of carbon such that a resistance change due to applied stress in the active arm produces a proportional voltage change in the bridge.

As described by Holloway et al. (1985), carbon resistors display a very fast response time, roughly the time required for the shock wave front to cross the resistor. Carbon resistors can be used to measure dynamic peak pressures to at least 100 MPa.

Based on the agreement between static and dynamic calibration (Holloway, 1985), quasi-static stress-voltage relationships for eight carbon stress gages were experimentally determined. Linear stress-voltage relationships were obtained for these gages, and a slope of the mean regression of 190.7 MPa/volt resulted. All voltage-time history data analyzed in this report utilizes this calibration value. Gage calibration results are given in APPENDIX B.

b.   Accelerometers

The instruments used to determine peak free field accelerations are ENDEVCO piezoresistive accelerometers (model 7270A) shown in Figure 3.5. These accelerometers are rugged undamped units designed for linear shock measurements up to 20,000 g's. The units are chemically sculptured from a single piece of silicon with an active four arm strain gage Wheatstone bridge. Its low mass of 1.5 grams, small size (14.2 mm by 7.1 mm by 2.8 mm thick), high resonant frequency (mounted; 350 kHz), and zero damping allow the accelerometers to respond accurately to

35
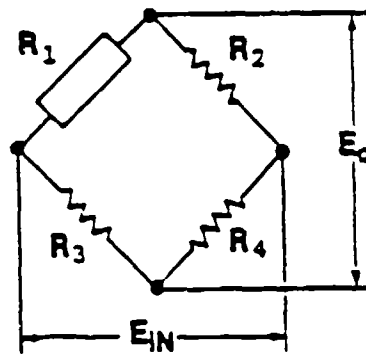
Figure 3.4 Single active arm Wheatstone bridge.

Figure 3.5   Endevco Piezoresistive accelerometers.

37

fast rise time, short duration shock motion. Calibration of the accelerometers was conducted by ENDEVCO. Calibration curves are given in APPENDIX B.

c. Data Recording System

Voltage-time histories were recorded by a Portable Data Acquisition System (Model 5700) manufactured by Pacific Instruments. It conditions, amplifies, digitizes, and records transducer signals at sampling rates of up to one million samples per second. The fully programmable 16 channel system has a memory capacity of 256 kilobytes per channel. The data acquisition system is mounted on the axis of the centrifuge (Figure 3.1) so that data can be transferred directly from the instruments without having to send signals through the slip rings. Slip rings, located at the base of the centrifuge axis, provide all electrical communication to the control console during operation. A high-speed video camera is mounted above the data recorder (Figure 3.1) and allows the operator to continuously monitor the specimen during flight.

3. System Configuration

A schematic of the centrifuge and equipment is shown in Figure 3.6. When the firing mechanism is engaged, a signal is sent through the slip rings triggering the data acquisition and detonating the charge simultaneously. After testing is completed, an IEEE-488 general purpose interface bus (GPIB) is connected to the data recorder mounted on the centrifuge, and the data is downloaded to a personal computer. A system language, ASYST, is utilized for communication between the data recorder and computer by means of the GPIB. Software utilized to control data recorder functions and channel programming is Pacmon revision C written by Pacific Instruments. The large amount of data acquired over a period of very fast sampling is stored on a 44-megabyte removable cartridge Bernoulli.
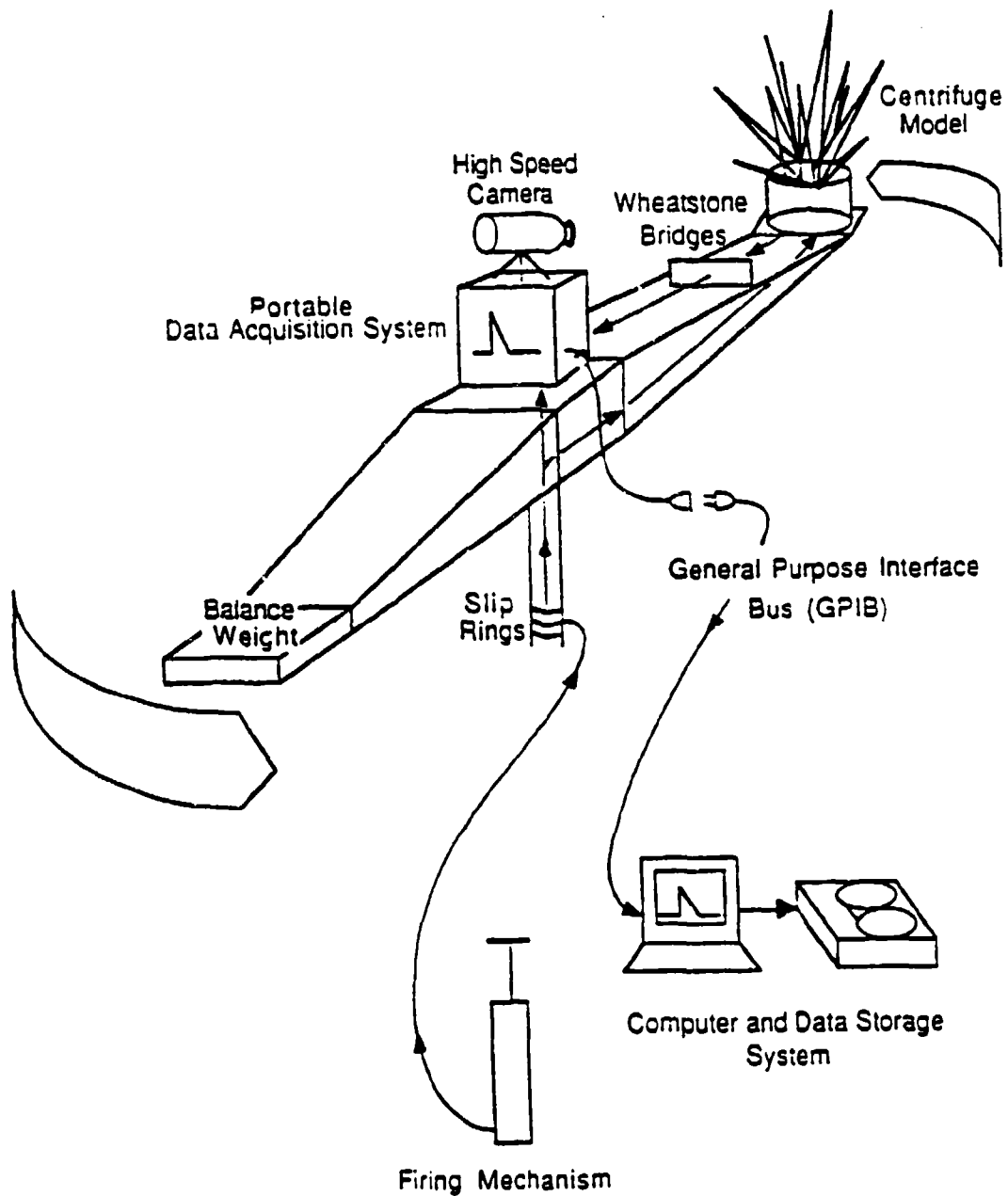
Figure 3.6 Schematic of the centrifuge and equipment.

39

4. Explosives

The explosive charges utilized in these tests are exploding bridgewire detonators manufactured by Reynolds Industries. Two types of detonators were used in our studies, the RP-83 detonator and a modification of this detonator. A cross section of an RP-83 detonator is shown in Figure 3.7.

The detonators consist of an exploding wire bridge, 80 mg of a low-density initiating explosive of PETN (pentaerythritol tetranitrate), 123 mg of PBX 9407 (cyclotetramethyl-enetetranitramine) in addition to the initiator, and a high density PBX 9407 output charge, all of which are contained in a 0.018 mm thick aluminum cup. The high output charge of the RP-83 detonator consists of four individual pressings of PBX 9407 each weighing 227 mg, and the modified RP-83 detonator has only one pressing of PBX 9407. Table 3.1 breaks down the total output charge for both detonators.

The composition of PBX 9407 consists of 94 percent RDX, and 6 percent Exon 461 which acts as a binder. Explosive TNT equivalency for RDX, PETN and PBX 9407, as described in The Manual for the Prediction of Blast and Fragment Loadings on Structures (Baker et al, 1980), is given in Table 3.2. Most blast work is presented using equivalent TNT weight. TNT equivalents for shock pressures are based on heat of detonation as suggested in Anonymous (1990).

Because the charge density of the PETN initiator is about half of that of PBX 9407 (Table 3.1), and because its mass is small compared to the total output charge, the mass of PETN is not included in the total output charge of the detonator. These total output charge masses were also suggested by Reynolds Industries (personal communication, Ron Varosh). Future reference to detonator explosive mass in this report will refer to PBX 9407 total output charge (Table 3.1).

40

0.294 DIA. MAX. (7.47)

2 1 3 4 6 5 7

0.280 Dia. Max. (7.11)

10.0 - 11.0 (254 - 279)

1.56 MAX. (39.62)
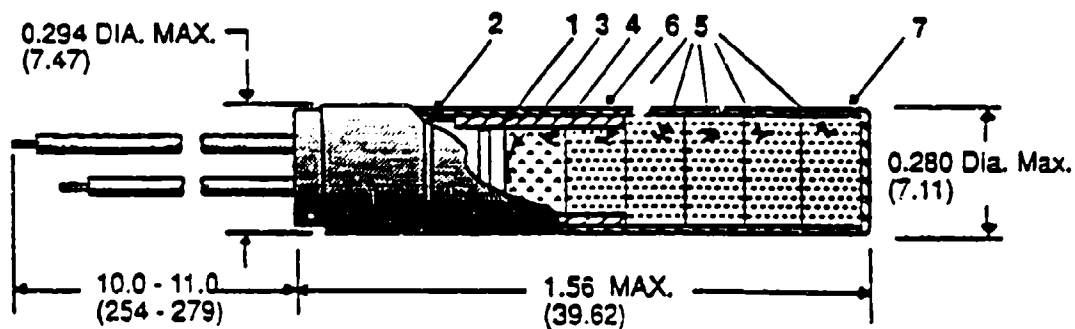
PARTS DESCRIPTION

1. MOLDED HEAD:
2. "O" RING.
3. BRIDGEWIRE: Gold.
4. INITIATING EXPLOSIVE: 80 mg of PETN.
5. TOTAL OUTPUT CHARGE: 1031 mg
6. ALUMINUM CUP:

Figure 3.7   RP-83 detonator (Reynolds Industries).

Table 3.1 CHARGE MASS FOR RP-83 AND MODIFIED RP-83 DETONATORS
(PERSONAL COMMUNICATION: RON VAROSH, REYNOLDS INDUSTRIES).

| | CHARGE | | DETONATOR | |
COMPONENT	TYPE	DENSITY (gm/cc)	RP-83 (mg)	Modified RP-83 (mg)
Initiating Explosive	PETN	0.88	80*	80*
Pellet	PBX 9407	1.60	123	123
Output Charge	PBX 9407	1.60	908	227
	TOTAL OUTPUT CHARGE:		1031 mg	350 mg

* Not used in total output charge.

Table 3.2 EXPLOSIVE EQUIVALENCE WITH RESPECT TO HEAT OF DETONATION (BAKER ET AL., 1980).

EXPLOSIVE	HEAT OF DETONATION H^d (ft-lb/lb)	TNT EQUIVALENCE H^d_{exp}/H^d_{TNT}
TNT	1.97×10^6	1.000
PETN	2.31×10^6	1.173
RDX	2.27×10^6	1.152
PBX 9407	2.24×10^6	1.137

B.   SOIL PROPERTIES AND SPECIMEN PREPARATION

1.   Soil Properties

Tyndall beach sand is obtained from dunes at Tyndall Air Force Base, Florida. The sand is oven dried, then sieved to remove organics. Ottawa 20-30 sand, is obtained from the U.S. Silica Company, Ottawa, Illinois (ASTM C190). A summary of the physical properties of both Tyndall and Ottawa sands is given in Tables 3.3a and 3.3b. Grain size distributions for the sands are shown in Figure 3.8 (ASTM D421-58 and D422-63). Both Tyndall and Ottawa sands are poorly graded sands.

Desaturation curves obtained by the porous plate method for Tyndall and Ottawa sands are shown in Figures 3.9(a) and (b) (ASTM D2325). Both sands begin to desaturate at capillary pressures (u_a-u_w) of 1 kPa and reach residual saturations (approximately 11 percent for Tyndall sand and 5 percent for Ottawa sand) at capillary pressures greater than 15 kPa. ASTM standard test methods can be found in ASTM (1987).

2.   Compaction Methods

Soil placement is critical in conducting our investigation and we are interested in placement techniques similar to those commonly used to place cohesionless backfill material during construction. Two methods of compaction, raining and vibration, were evaluated for preparing sand specimens efficiently and with reproducibility. The vibration method was used to conduct this research effort.

The method of raining is widely used and offers the ability to obtain sand specimens with a great deal of reproducibility and best simulates the natural process of sand deposition. The procedure for this method consists of dry sand raining from a shutter, through a vertical column, then through a series of diffuser sieves. Shutter porosity and fall height are a few of the many variables one can adjust to obtain a target density. Three apparent problems exist with this method: first, there are no known techniques for raining partially saturated specimens;

Table 3.3a PHYSICAL PROPERTIES OF TYNDALL BEACH SAND.

Soil Description	Poorly graded sand composed mainly of quartz. Soil particles are subangular to subrounded.	
Maximum Relative Density ($\rho_{d\,maximum}$)	1630 kg/m^3	(ASTM D4253)
Minimum Relative Density ($\rho_{d\,minimum}$)	1450 kg/m^3	(ASTM D4254)
Mean Grain Size (D_{50})	0.25 mm	(ASTM D422)
Specific Gravity (G_s)	2.65	(ASTM D854)

Table 3.3b PHYSICAL PROPERTIES OF OTTAWA 20-30 SAND.

Soil Description	Poorly graded sand composed mainly of quartz. Soil particles are subrounded to rounded in shape.	
Maximum Relative Density ($\rho_{d\,maximum}$)	1720 kg/m^3	(ASTM D4253)
Minimum Relative Density ($\rho_{d\,minimum}$)	1560 kg/m^3	(ASTM D4254)
Mean Grain Size (D_{50})	0.70 mm	(ASTM D422)
Specific Gravity (G_s)	2.65	(ASTM D854)
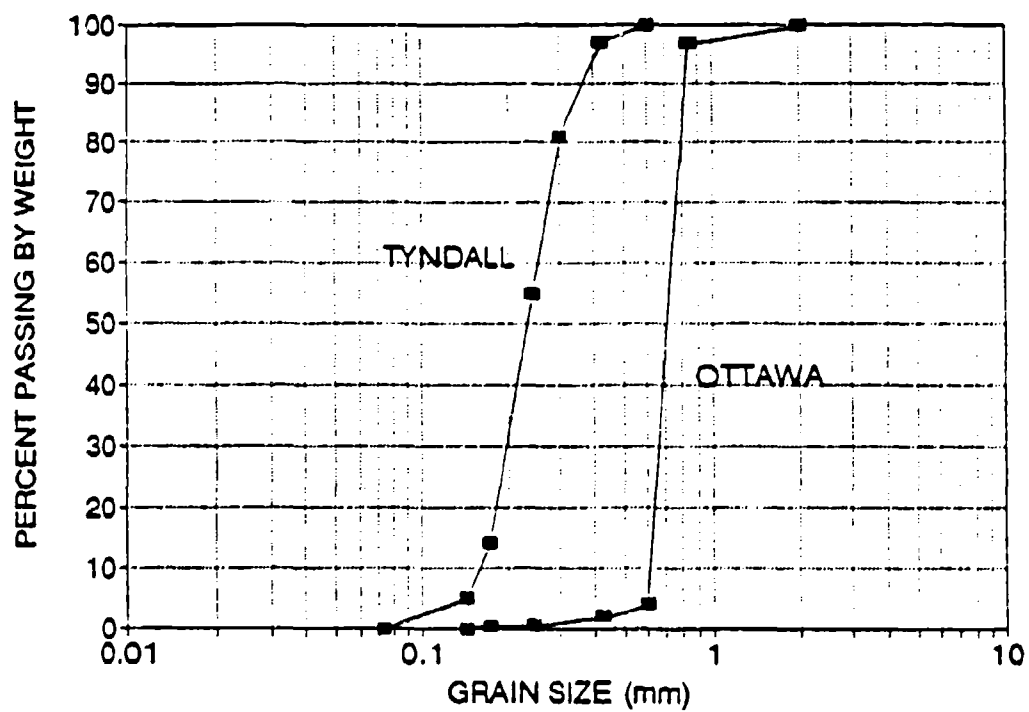
Figure 3.8 Grain size distributions for Tyndall beach and Ottawa 20-30 sands.
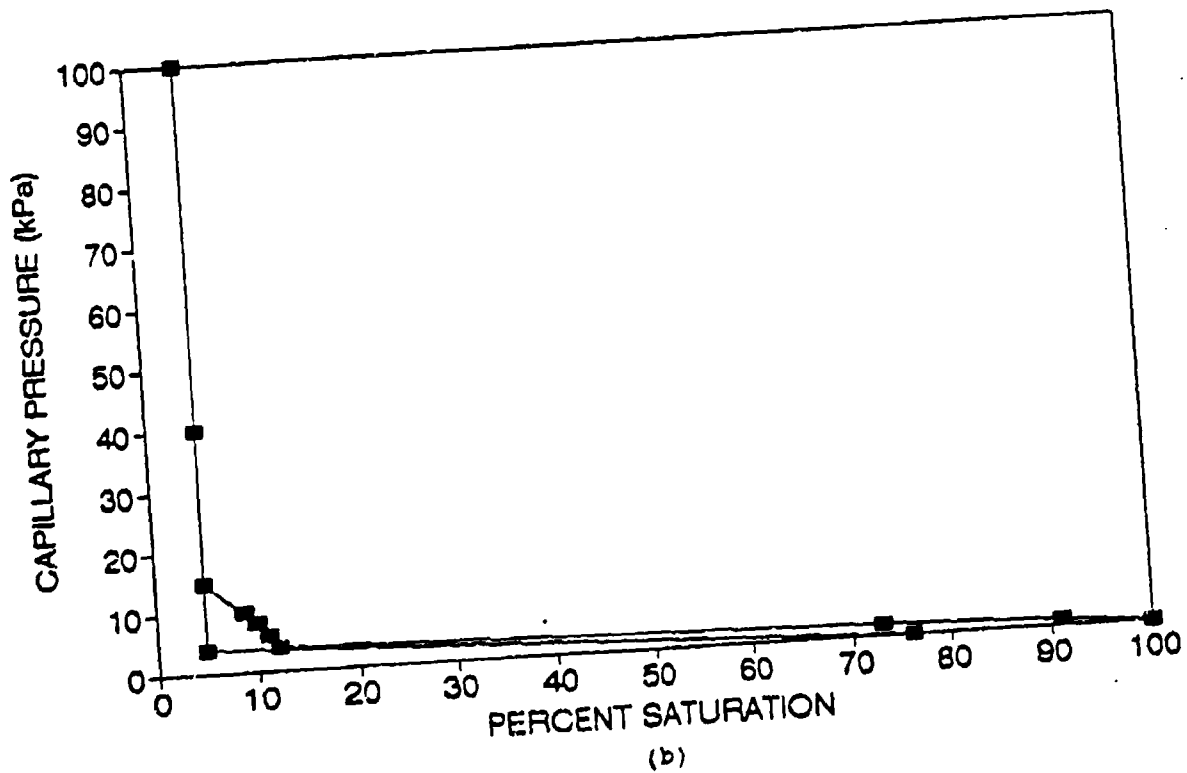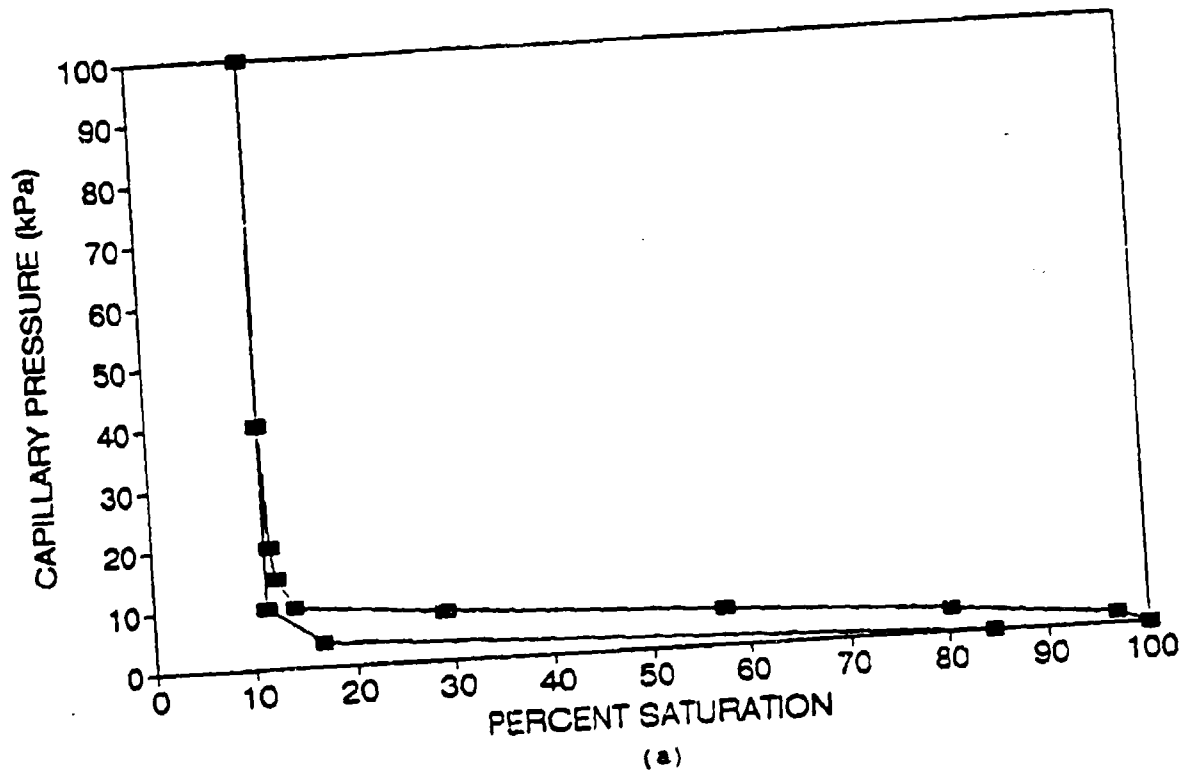
Figure 3.9   Desaturation curves.   (a) Tyndall beach sand.   (b) Ottawa 20-
30 sand.   46

second, placement of a level layer is difficult to obtain; and third, raining is not used for placing backfill during construction.

Vibration proves to be quite effective for compacting both dry and wet soils and opposing the forces of capillarity. The vibration apparatus used for preparing the specimens is a variable amplitude 60 Hz vibrator motor, manufactured by Syntron (model V51 D1), and is mounted to a 13 mm thick aluminum plate (Figure 3.10). The apparatus is placed on the surface of the soil and allowed to compact as a vibrating surcharge. Additional surcharge weight can be placed on the aluminum plate. The vibration technique developed is similar to vibratory methods used during construction (i.e. walk behind vibrators and vibrating roller compactors).

3. Specimen and Instrumentation Placement

Centrifuge soil models are constructed in a specimen bucket with inside diameter of 46 cm and depth of 25.7 to 27.9 cm (Figure 3.11). Models consist of five horizontal lifts, each lift is compacted separately in order to obtain uniformity throughout the specimen. Target degree of saturation for the specimens are obtained when the appropriate amounts of sand and water for each lift are combined and compacted to a unit lift volume.

Target saturation levels for Tyndall sand are 0, 17, 35, 53, and 70 percent, and for Ottawa sand are 0, 20, 40, and 60 percent. Target dry density for Tyndall sand is 1521 kg/m³ (95.0 pcf) and for Ottawa sand is 1612 kg/m³ (100.7 pcf). Dry relative densities for Tyndall and Ottawa sands are 42 percent and 35 percent respectively. Distilled water is used as the pore fluid.

The bottom four lifts of the specimen are 5.1 cm thick and the overburden lift, above the instrument layer, varies in height (Figure 3.11). Overburden stresses at a prototype depth of 1.43 meters are simulated with a model overburden of 7.6 cm when accelerated to 18.86 g's. Similarly, accelerating the model to 26.34 g's with an overburden of 5.4 cm will produce a similar prototype overburden stress. As noted in

47
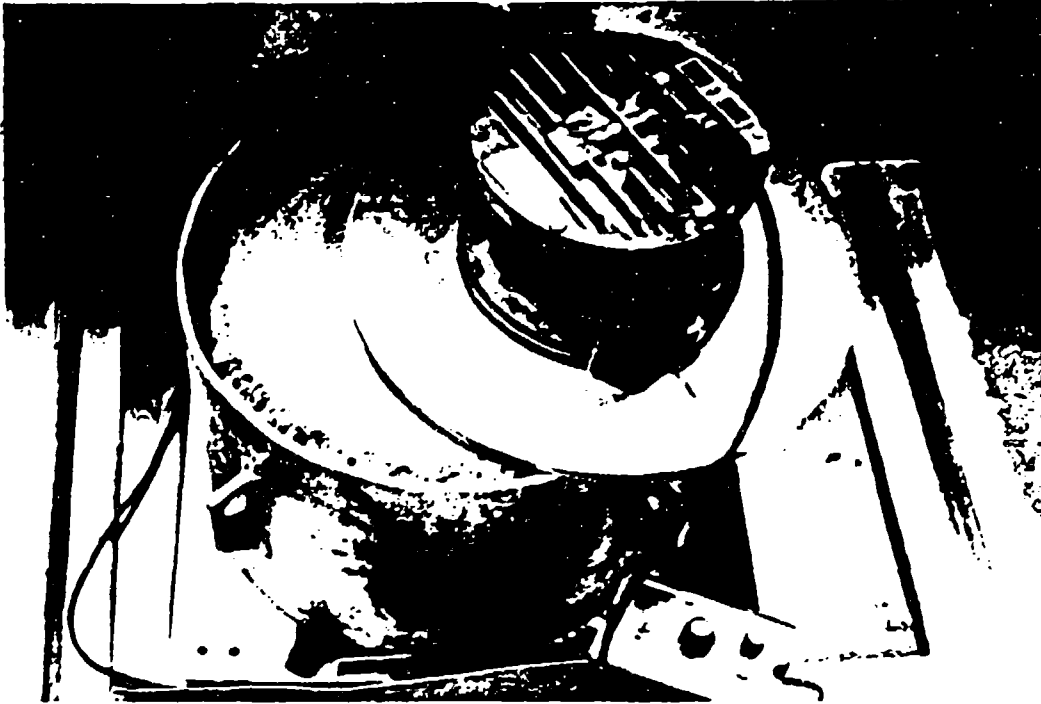
Figure 3.10   Vibrating apparatus used to compact specimens.
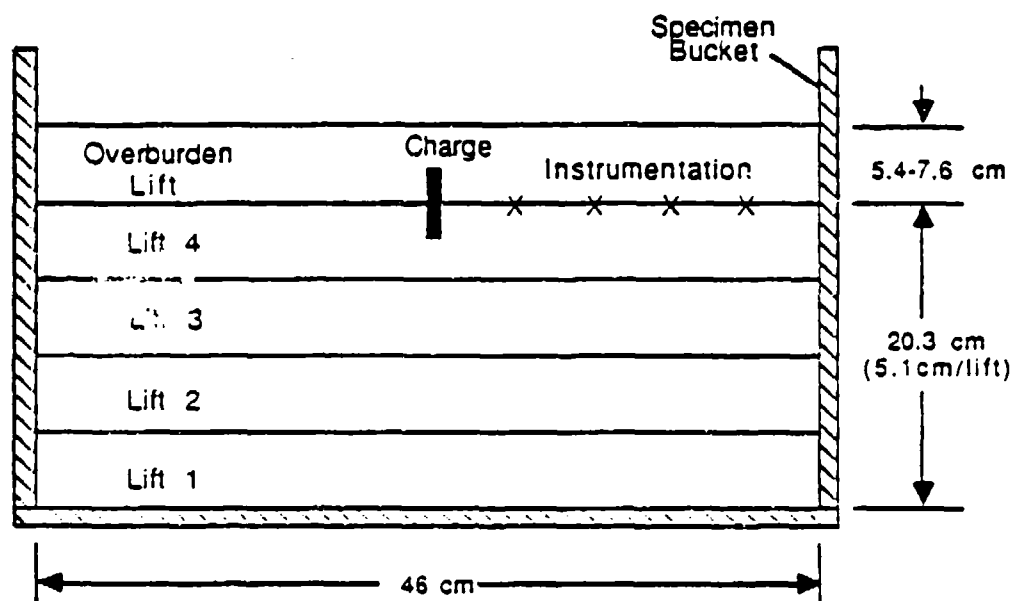
Figure 3.11 Cross section of centrifuge specimen.

Section II.A.3, the depth of burial of the blast is critical in order to completely transmit the energy of the blast to the surrounding medium. A scaled depth of burst of 0.71 m/kg$^{1/3}$ (1.8 ft/lb$^{1/3}$) was chosen to insure a ground shock coupling factor, f, of unity (Figure 2.1). Tables 3.4a and 3.4b list model-prototype relations for Tyndall and Ottawa sands. Extrapolating the prototype performance using scaled models at different g levels allows one to verify the principle of "modeling of models."

At the instrument layer, carbon stress gages and accelerometers extend outward form the center of the bucket where the charge is placed. Figure 3.12 illustrates the gage positions and distances from the charge. The prefix letter R designates carbon stress gages and the letter A designates accelerometers. Gage wires trail behind the gages toward the bucket wall so that stress waves traveling to the gages will not be distorted. Data interference due to transient waves reflected off the bucket bottom or transmitted through the container are minimized by situating the gages in the path of shortest travel from the blast (Figure 3.13).

4. Charge Placement

Blast simulation requires that the explosive yield of a model is the reciprocal of the acceleration cubed $(1/N^3)$ according to the scaling law for mass in Table 2.2. Depth of burial of the explosive similarly scales with the reciprocal of acceleration using the linear dimension property. Model-prototype relationships for charge mass and depth of burial for Tyndall and Ottawa sands are given in Tables 3.4a and 3.4b.

Two methods are used for placing charges consistently and with minimum disturbance to the model: first, a drilling method for placement in moist specimens, and second, a vacuum method for dry specimens. The depth of the borehole is determined such that the centroid of the charge is at the same level as the instrument layer. Dry sand is backfilled into the borehole after the charge is placed.

Table 3.4a MODEL-PROTOTYPE CHARACTERISTICS FOR TYNDALL BEACH SAND.

RPM	Arm Radius (m)	MODEL Accel. N[a] (g's)	Charge W[b] (gm)	Overburden D (cm)	PROTOTYPE Charge N³xW (kg)	Overburden NxD (m)
102.1	1.83	18.86	1.031	7.6	6.9	1.43
120.6	1.83	26.34	0.35	5.44	6.4	1.43

[a] Acceleration at level of instrumentation ($r = 1.62$ m).
[b] Based on total output charge mass (Table 3.1).

Table 3.4b MODEL-PROTOTYPE CHARACTERISTICS FOR OTTAWA 20-30 SAND.

RPM	Arm Radius (m)	MODEL Accel. N[a] (g's)	Charge W[b] (gm)	Overburden D (cm)	PROTOTYPE Charge N³xW (kg)	Overburden NxD (m)
191.9	1.83	66.65	0.35	5.44	104	3.63

[a] Acceleration at level of instrumentation ($r = 1.62$ m).
[b] Based on total output charge mass (Table 3.1).
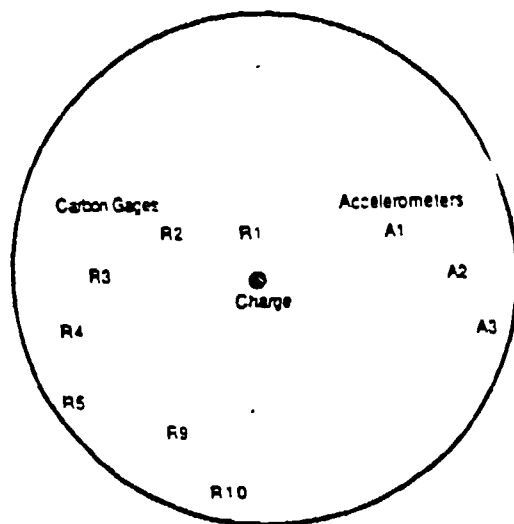
Gage	Distance from charge (cm)
R1	3.81
R2	7.62
R3	12.70
R4	17.78
R5	20.32
R9	17.78
R10	20.32
A1	12.70
A2	17.78
A3	20.32

Figure 3.12 Top view of gage and charge placement in centrifuge specimens.
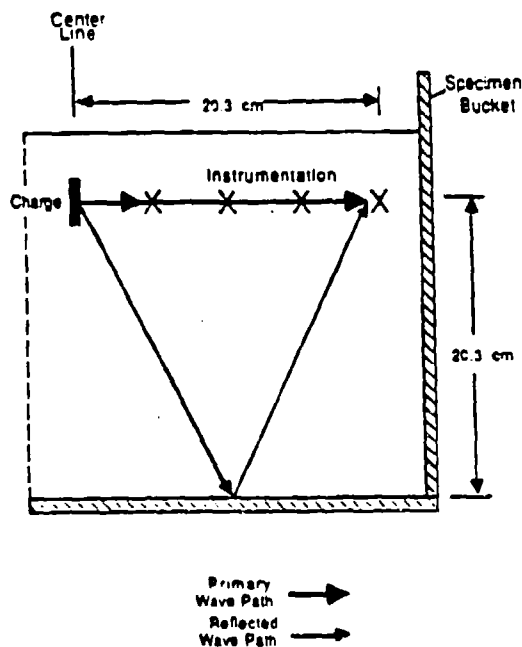
Figure 3.13 Illustration of wave path in centrifuge specimen.

SECTION IV

EXPERIMENTAL RESULTS

This chapter presents the results of 10 centrifuge explosive tests on Tyndall beach sand and 4 centrifuge explosive tests on Ottawa 20-30 sand.

A.   STRESS GAGE RESULTS

Voltage-time histories for four typical carbon stress gages are illustrated in Figure 4.1. Voltage readings were converted to values of stress using the calibration constant 190.7 MPa/volt obtained from static calibration of eight carbon gages (APPENDIX B). The stress gages are located at increasing distances from the charge (Figure 3.13). Arrival time of the stress wave increases respectively with increasing distance to the gages. Attenuation of peak stress is evident from the decrease in wave amplitudes with time in Figure 4.1.

A summary of stress gage results for Tyndall Beach sand are presented in Table 4.1 listing values of peak stress, wave arrival times, and average wave velocity between respective stress gages. Ten tests were conducted, two tests each of 0, 20, 40, 60, and 70 percent saturations. Test names are listed in the left column of these tables; the first numeral represents the g level at the model platform, followed by the saturation of the test, then the test number performed at that saturation level. The g level at the instrumentation level is given in parenthesis below the test name. Results of four tests on Ottawa 20-30 sand are given in Table 4.2 for saturations of 0, 20, 40, and 60 percent.

Peak stresses from Tables 4.1 and 4.2 for Tyndall and Ottawa sands are plotted versus scaled distance in Figures 4.2 and 4.3. Wave arrival

(The reverse of this page is blank.)
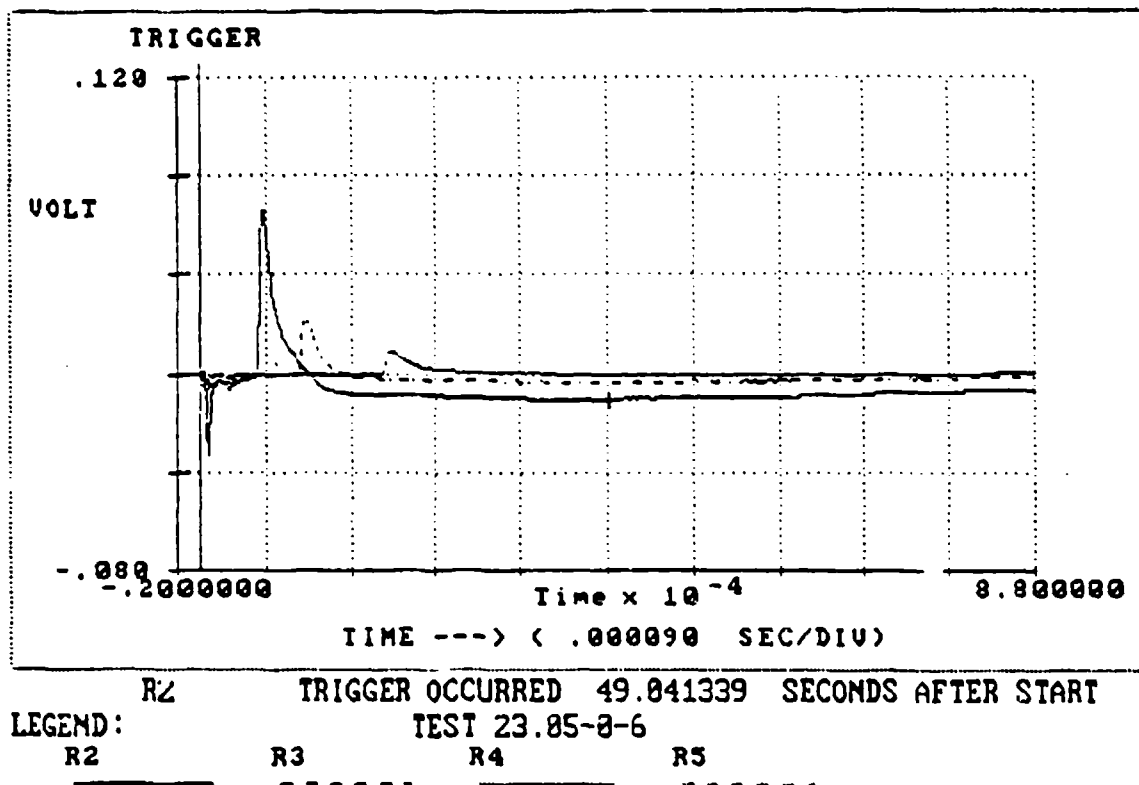
Figure 4.1 Typical voltage-time histories for carbon stress gages R2, R3, R4, and R5.

Table 4.1   STRESS GAGE RESULTS FOR TYNDALL BEACH SAND

Test	Charge Wt. (gm)	Instr.	Gage Dist. to Charge (cm)	Peak Stress (kPa)	Arrival Time (u s)	Wave Velocity (m/s)
21.3-0-7	1.031	R1	3.81	17015	47	
(18.86)		R2	7.62	3584	114	569
		R3	12.7	132	221	475
		R4	17.78	528	352	388
		R5	20.32	183	436	302
		R9	17.78	416	3?4	
		R10	20.32	214	483	257
29.8-0-9	0.35	R1	3.81	11172	47	
(26.34)		R2	7.62	2030	115	560
		R3	12.7	410	260	350
		R4	17.78	130	464	249
		R5	20.32	114	565	251
		R6	17.78	336	413	
		R7	20.32	86	532	213
29.8-20-2	0.35	R1	3.81	7464	51	
(26.34)		R2	7.62	2978	122	537
		R3	12.7	601	249	400
		R4	17.78	370	377	397
		R5	20.32	109	449	353
21.3-20-3	1.031	R1	3.81	15917	42	
(18.86)		R2	7.62	4004	114	529
		R3	12.7	1243	223	466
		R4	20.32	463	426	375
		R5	17.78	536	348	326
		R9	17.78	360	368	
		R10	20.32	286	416	529
29.8-40-1	0.35	R1	3.81	6291	57	
(26.34)		R2	7.62	1573	132	508
		R3	12.7	597	262	391
		R4	17.78	282	427	308
		R5	20.32	126	516	285
		R10	20.32	183	478	
21.3-40-2	1.031	R1	3.81	22752	41	
(18.86)		R2	7.62	4404	111	544
		R3	12.7	1285	214	493
		R4	17.78	757	367	332
		R5	20.32	377	445	326
		R9	17.78	702	359	
		R10	20.32	429	409	508

Table 4.1 (continued)   STRESS GAGE RESULTS FOR TYNDALL BEACH SAND

Test	Charge Wt. (gm)	Instr.	Gage Dist. to Charge (cm)	Peak Stress (kPa)	Arrival Time (u s)	Wave Velocity (m/s)
29.8-60-1	0.35	R1	3.81	5977	60	537
(26.34)		R2	7.62	1098	131	394
		R3	12.7	387	260	294
		R4	17.78	290	433	
		R5	20.32	132	597	0
		R10	20.32	194	480	
21.3-60-2	1.031	R1	3.81	20534	49	605
(18.86)		R2	7.62	3937	112	488
		R3	12.7	1336	216	348
		R4	17.78	694	362	326
		R5	20.32	368	440	
		R9	7.62	5008	113	450
		R10	12.7	1401	226	
21.3-70-3	1.031	R2	7.62	4720	113	454
(18.86)		R3	12.7	1584	225	382
		R4	17.78	644	358	343
		R5	20.32	370	432	
		R6	20.32	667	431	
29.8-70-4	0.35	R1	3.81	7039	61	488
(26.34)		R2	7.62	1443	139	353
		R3	12.7	467	283	293
		R4	20.32	120	543	
		R5	20.32	69	628	0
		R6	17.78	137	443	

Parentheses indicate g level at instrument depth.

Table 4.2   STRESS GAGE RESULTS FOR OTTAWA 20-30 SAND

Test	Charge Wt. (gm)	Instr.	Gage Dist. to Charge (cm)	Peak Stress (kPa)	Arrival Time (u s)	Wave Velocity (m/s)
75.3-0-10	0.35	R1	3.81	8916	20	
(66.65)		R2	7.62	503	102	465
		R3	12.7	349	279	287
		R4	17.78	103	468	269
		R5	20.32	19	652	138
		R6	20.32	29	634	153
75.3-20-6	0.35	R2	7.62	1192	120	
(66.65)		R3	12.7	448	273	332
		R4	17.78	92	487	237
		R5	20.32	59	546	431
75.3-40-5	0.35	R1	3.81	6293	47	
(66.65)		R2	7.62	1312	128	470
		R3	12.7	391	269	360
		R4	17.78	162	547	274
		R5	20.32	23	576	248
75.3-60-5	0.35	R1	3.81	4879	51	
(66.65)		R2	7.62	1233	138	438
		R3	12.7	381	289	336
		R4	17.78	72	520	220
		R5	20.32	27	618	259
		R6	20.32	74	644	205

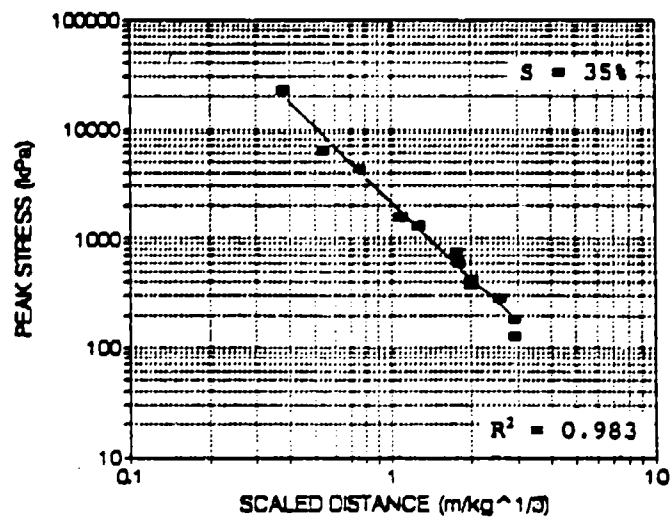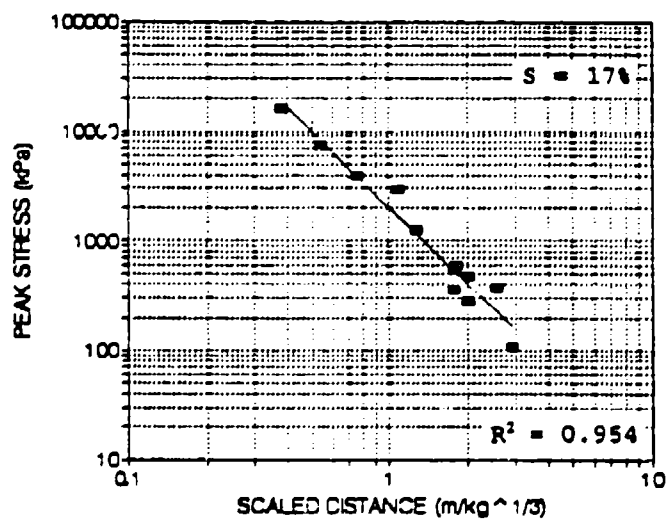Parentheses indicate g level at instrument depth.

58

Figure 4.2 **Peak stress as a function of scaled distance for Tyndall beach sand.**

Figure 4.2 (continued) Peak stress as a function of scaled distance for Tyndall beach sand.
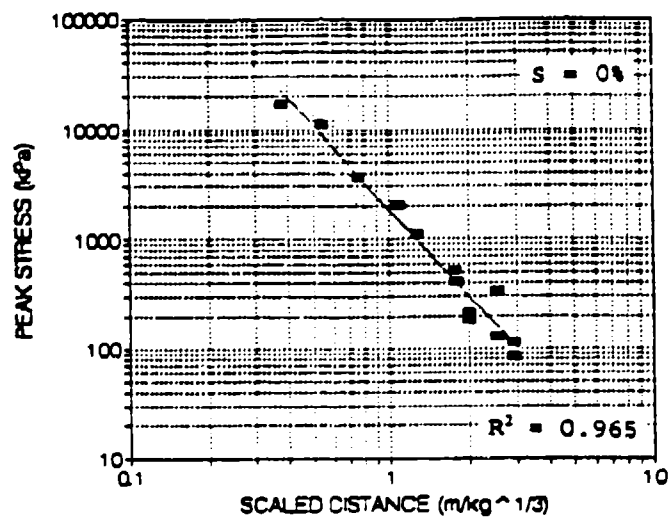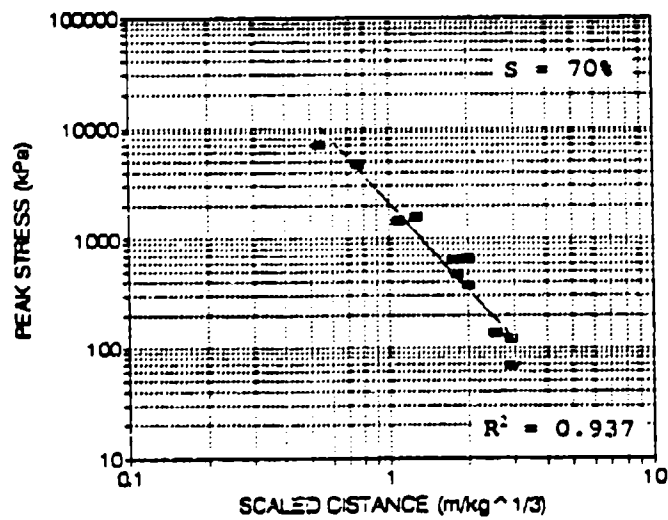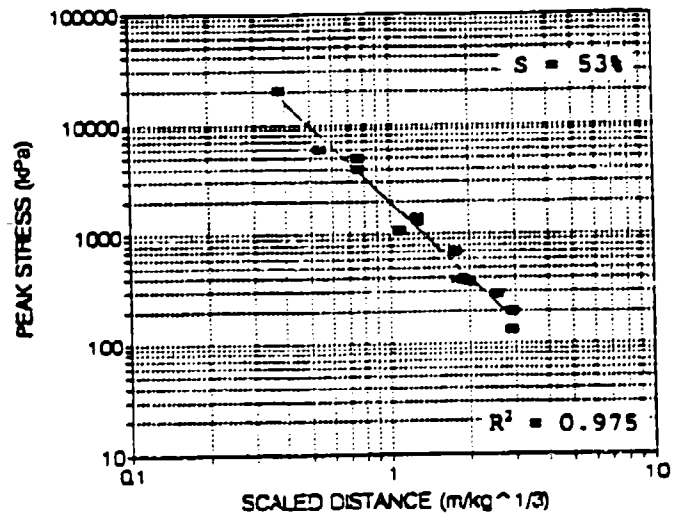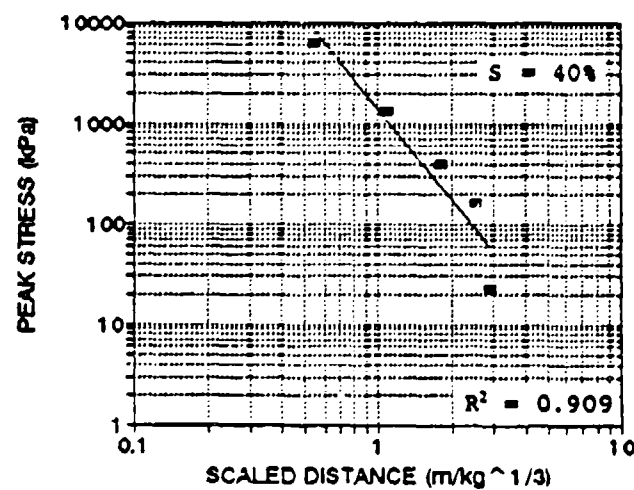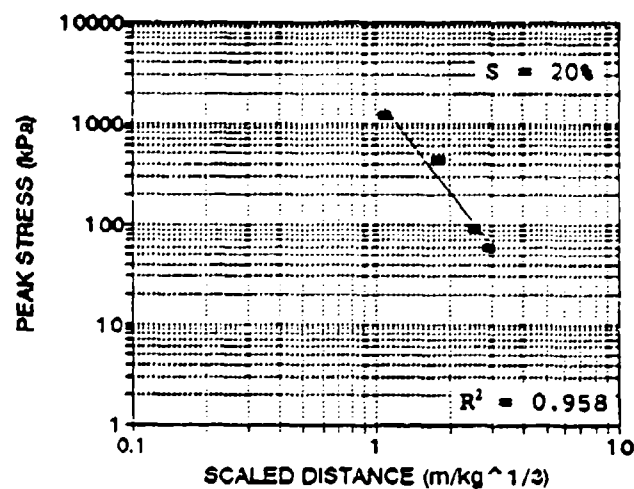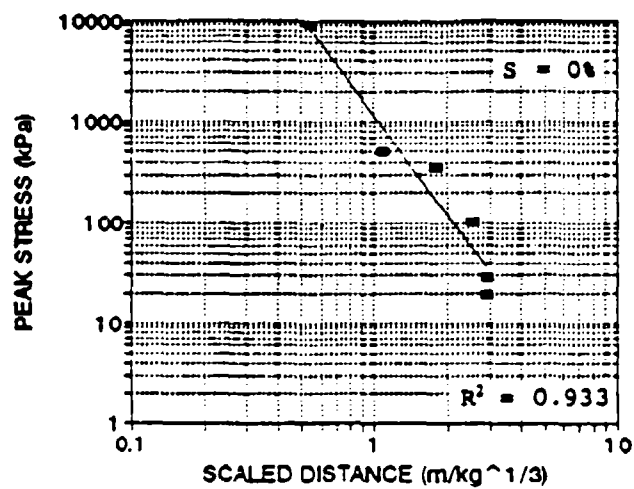
Figure 4.3 Peak stress as a function of scaled distance for Ottawa 20-30 sand.
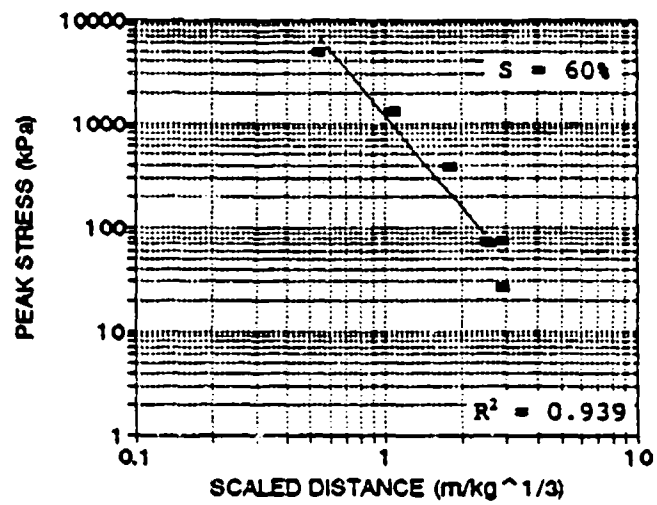
Figure 4.3 (continued)   Peak stress as a function of scaled distance for Ottawa 20-30 sand.

times from Tables 4.1 and 4.2 were obtained from stress-time histories at the wave front, or the point at which the change in stress with time is greatest. Stress wave velocity between gages was determined by taking the difference in the gage positions from the charge, then dividing by the difference in arrival times to the respective gages. The wave velocity of the model scales directly with the wave velocity of the prototype (Table 2.2). Plots of stress wave velocity versus scaled distance for Tyndall and Ottawa sands are shown in Figures 4.4 and 4.5.

B. ACCELEROMETER RESULTS

Accelerometers were utilized for free field particle acceleration-time histories. Calibration of the gages was conducted by ENDEVCO and programmed into the data recorder so that values of acceleration in units of g's could be directly obtained (1 g = 9.81 m/s^2 = 32.2 ft/s^2).

A typical acceleration-time history curve is illustrated in Figure 4.6. Peak particle accelerations were obtained from the wave peaks. Particle velocity-time histories were obtained by integrating acceleration-time histories (Figure 4.6). Similarly, peak particle velocities were obtained from the velocity-time wave peaks.

Peak particle accelerations and peak particle velocities for Tyndall and Ottawa sands are summarized in Tables 4.3 and 4.4. Scaled peak particle accelerations are plotted versus scaled distance in Figures 4.7 and 4.8. Peak particle accelerations are scaled by multiplying by N so that prototype peak particle accelerations are simulated (Table 2.2).

Peak particle velocities obtained from velocity-time histories were obtained in units of g-seconds, then converted to meters per second in Tables 4.3 and 4.4. Peak particle velocities are plotted versus scaled distance in Figures 4.9 and 4.10.

Figure 4.4 Wave velocity as a function of scaled distance for Tyndall beach sand.

64
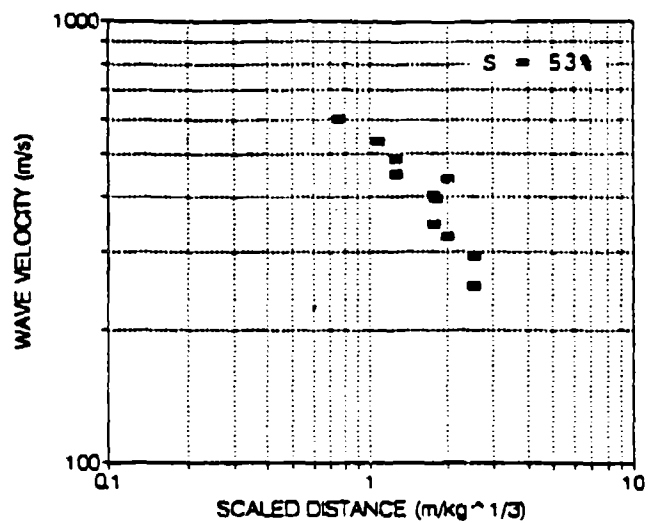
Figure 4.4 (continued)   Wave velocity as a function of scaled distance for
Tyndall beach sand.

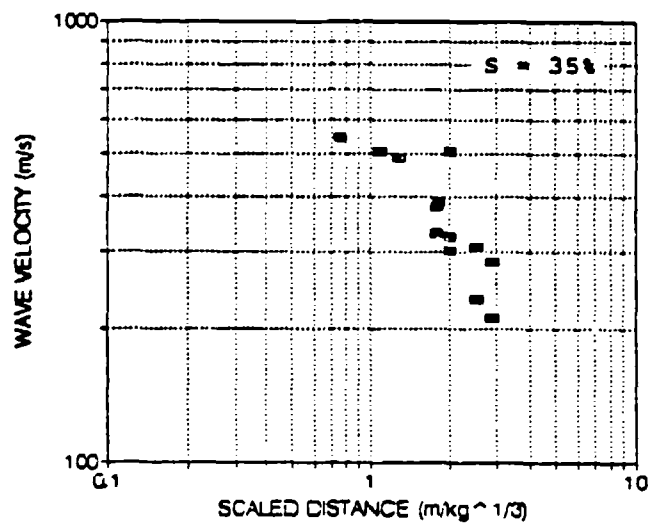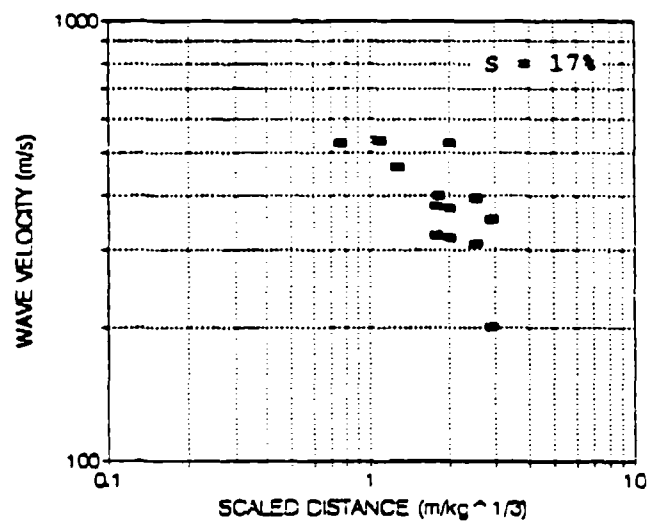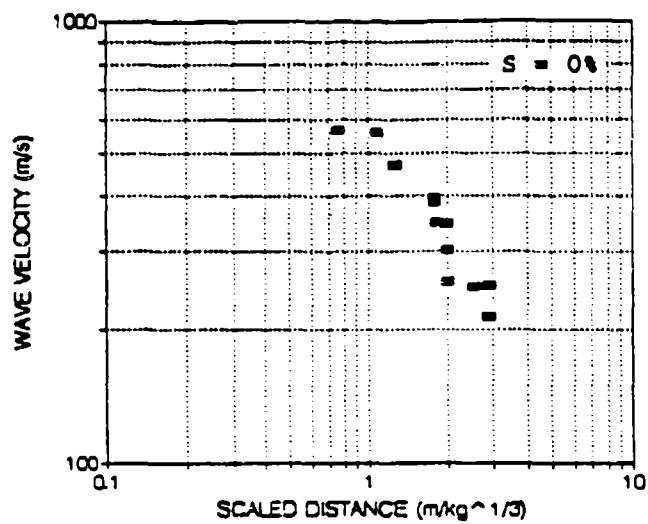**Figure 4.5** Wave velocity as a function of scaled distance for Ottawa 20-30 sand.

66
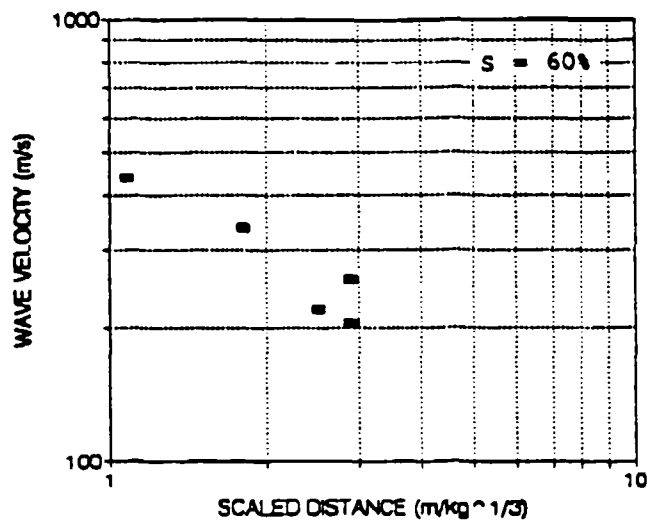
Figure 4.5 (continued) Wave velocity as a function of scaled distance for Ottawa 20-30 sand.
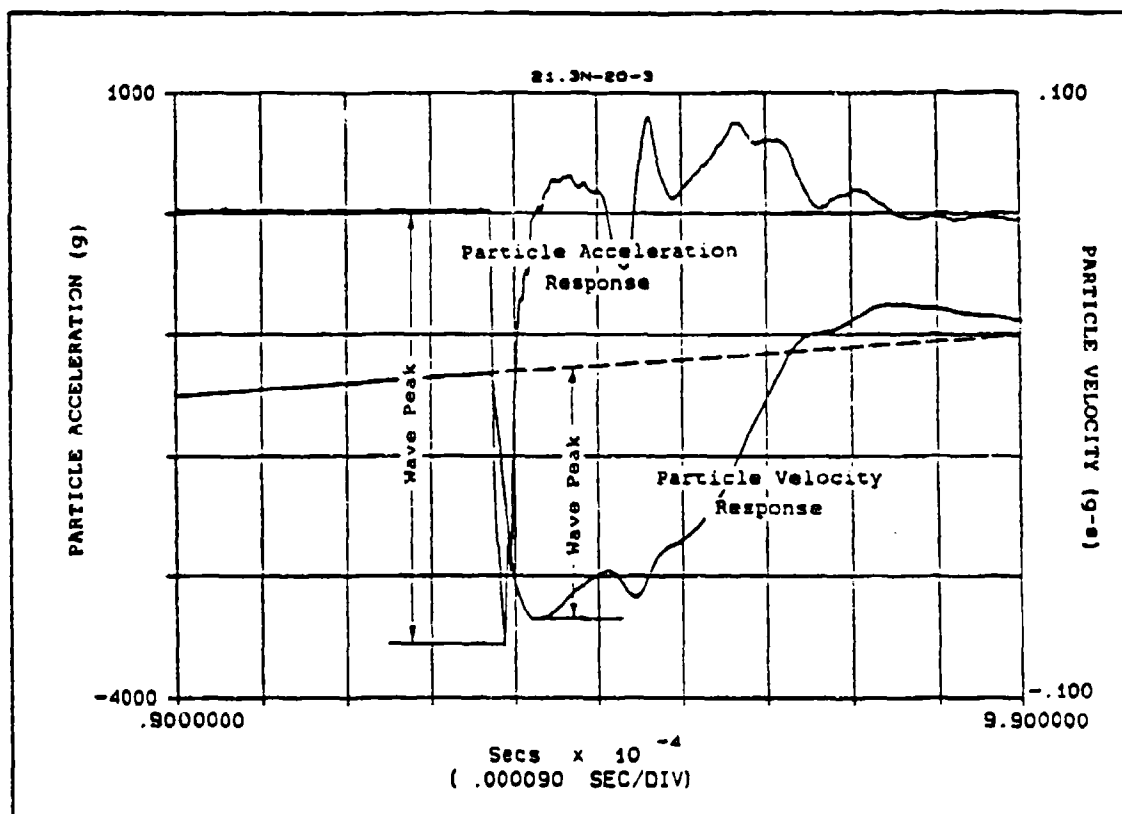
Figure 4.6 Typical acceleration-time history and integrated velocity-time history curves.

Table 4.3   ACCELEROMETER RESULTS FOR TYNDALL BEACH SAND

Test	Charge Wt. (gm)	Instr.	Gage Dist. to Charge (cm)	Peak Particle Accel. (m/s^2)	Peak Particle Velocity (g-s)	(m/s)
21.3-0-7	1.031	A1	12.7	121739	0.22	2.16
(18.86)		A2	17.78	45410	0.12	1.18
		A3	20.32	26280	0.08	0.78
29.8-0-9	0.35	A1	12.7	52050	0.11	1.04
(26.34)		A2	17.78			
		A3	20.32	10824	0.04	0.35
29.8-20-2	0.35	A1	12.7	68822	0.12	1.18
(26.34)		A2	17.78	24431	0.06	0.55
		A3	20.32	11215	0.04	0.34
21.3-20-3	1.031	A1	12.7	159186	0.24	2.35
(18.86)		A2	17.78	56155	0.12	1.18
		A3	20.32	34814	0.08	0.78
29.8-40-1	0.35	A1	12.7	48146	0.11	1.08
(26.34)		A2	17.78	9557	0.04	0.41
		A3	20.32	8873	0.03	0 31
21.3-40-2	1.031	A1	12.7	164535	0.25	2.40
(18.86)		A2	17.78	69447	0.12	1.20
		A3	20.32	46905	0.08	0.82
29.8-60-1	0.35	A1	12.7	44821	0.10	0.94
(26.34)		A2	17.78	18379	0.05	0.45
		A3	20.32	16041	0.04	0.41
21.3-60-2	1.031	A1	12.7	141402	0.27	2.55
(18.86)		A2	17.78	59209	0.12	1.18
		A3	20.32	40128	0.09	0.36
21.3-70-3	1.031	A1	12.7	152391	0.23	2.26
(18.86)		A2	17.78	49595	0.11	1.06
		A3	20.32	38957	0.08	0.82
29.8-70-4	0.35	A1	12.7	51327	0.11	1.06
(26.34)		A2	17.78	17813	0.06	0.54
		A3	20.32	13311	0.04	0.41

Parentheses indicate g level at instrument depth.

Table 4.4 ACCELEROMETER RESULTS FOR OTTAWA 20-30 SAND

Test	Charge Wt. (gm)	Instr.	Gane Dis. to Charge (cm)	Peak Particle Accel. (m/s^2)	Peak Particle Velocity (g-s)	(m/s)
75.3-0-10 (66.65)	0.35	A3	20.32	2828.2	0.02	0.21
75.3-2 6 (66.65)	0.35	A1	12.7	35336.6	0.10	0.96
		A2	17.78	7502.7	0.04	0.34
		A3	20.32	3226.5	0.03	0.25
75.3-40-5 (66.65)	0.35	A1	12.7	17638.4	0.05	0.47
		A2	17.78	13798.7	0.05	0.50
		A3	20.32	8532.7	0.04	0.34
75.3-60-5 (66.65)	0.35	A1	12.7	28916.0	0.10	1.02
		A2	17.78	9207.7	0.04	0.39
		A3	20.32	2781.1	0.02	0.22

Parentheses indicate g level at instrurnant depth.

70
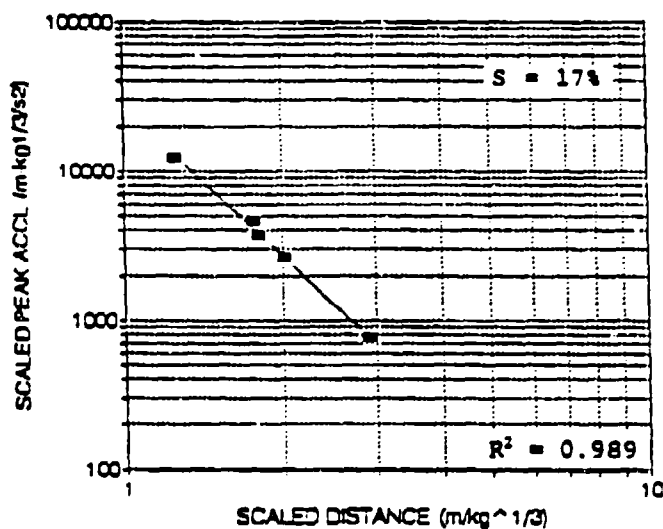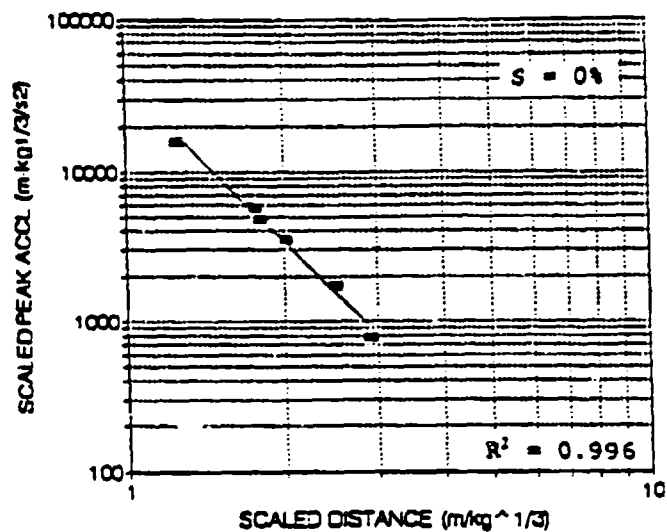
Figure 4.7   Scaled peak particle acceleration as a function of scaled distance for Tyndall beach sand.

71
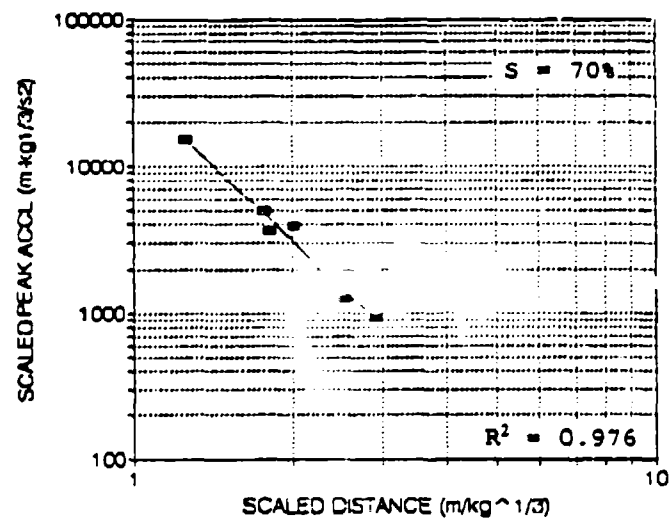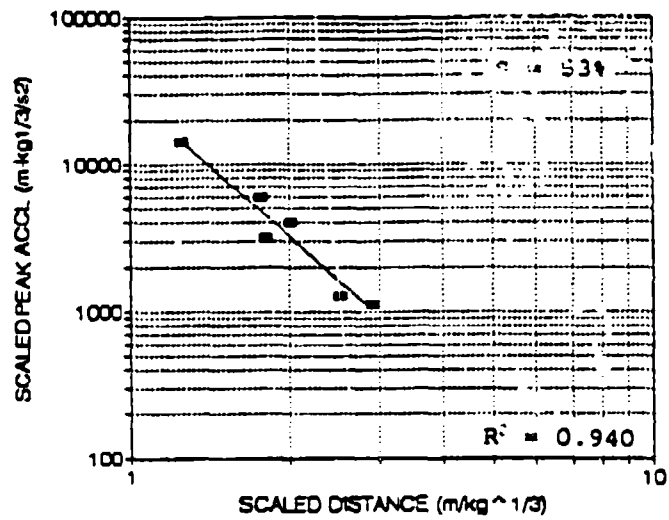
Figure 4.7 (continued)   Scaled peak particle acceleration as a function
of scaled distance for Tyndall beach sand.
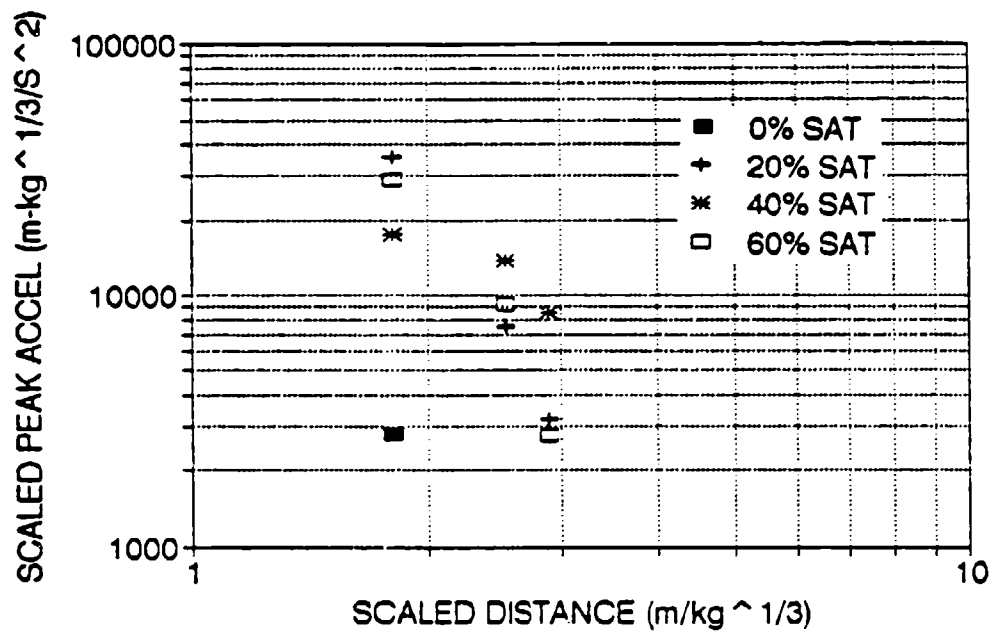
Figure 4.8 Scaled peak particle acceleration as a function of scaled distance for Ottawa 20-30 sand.

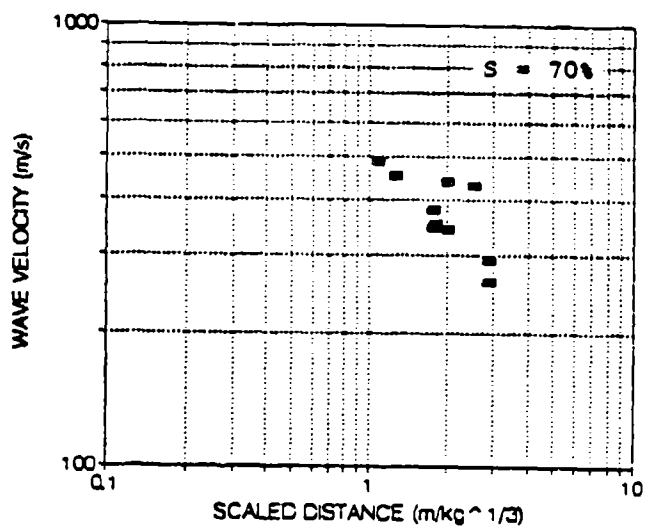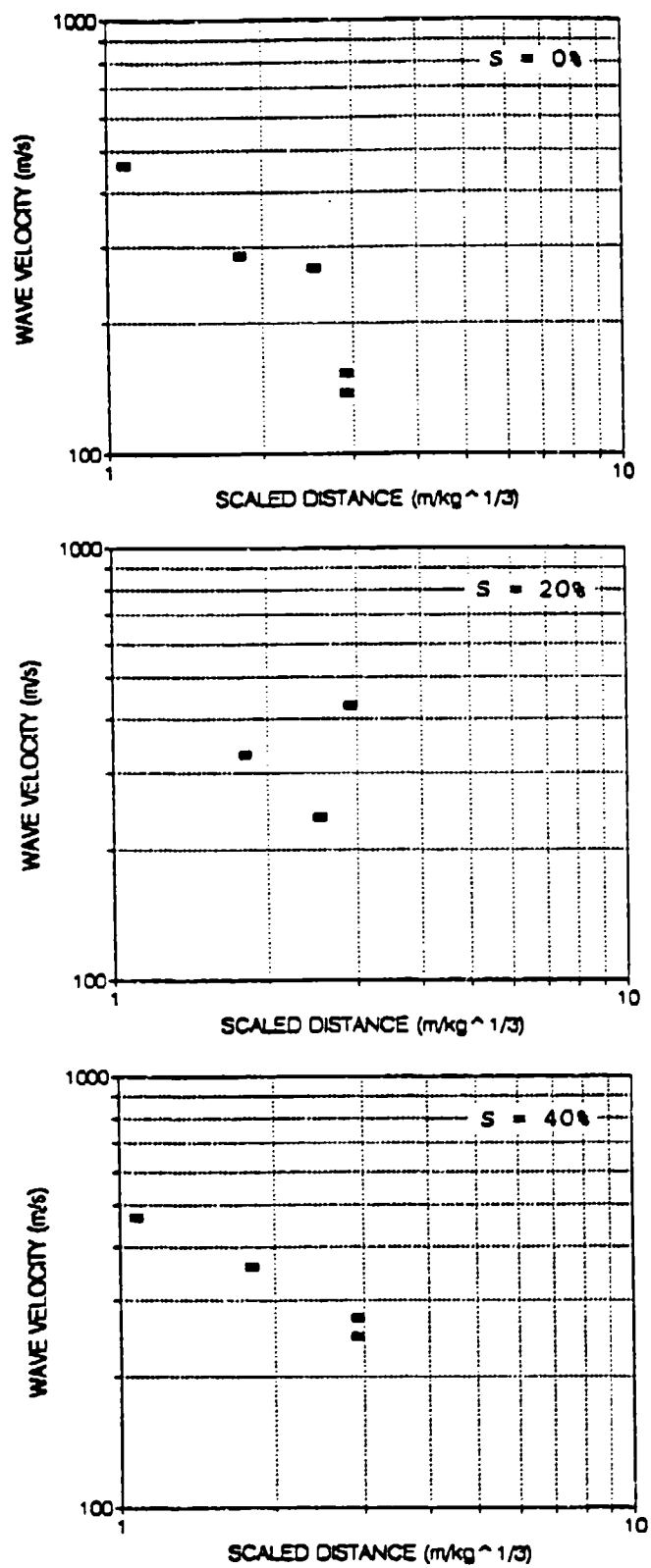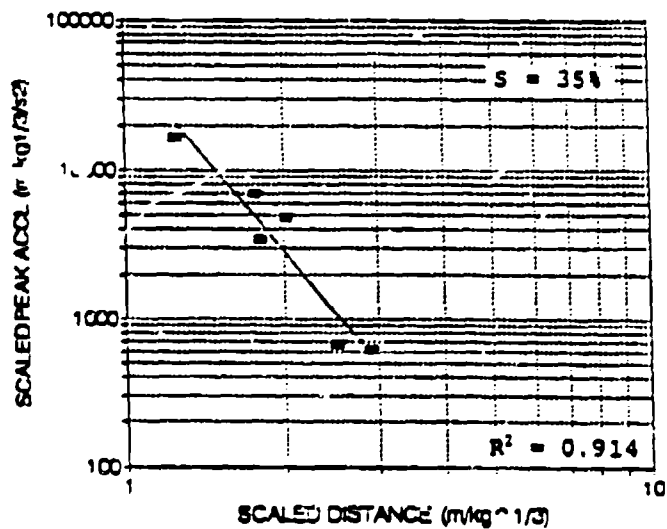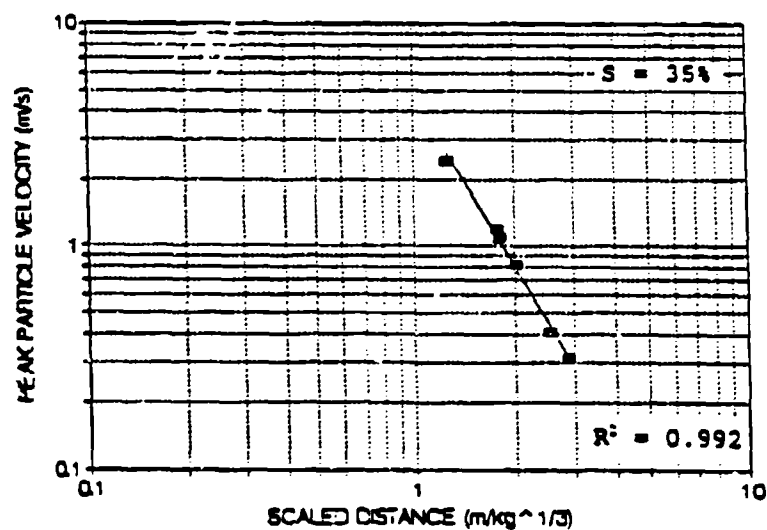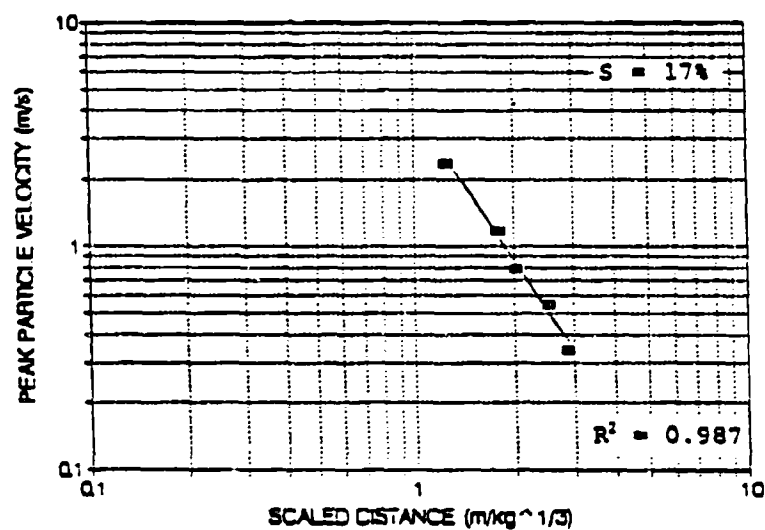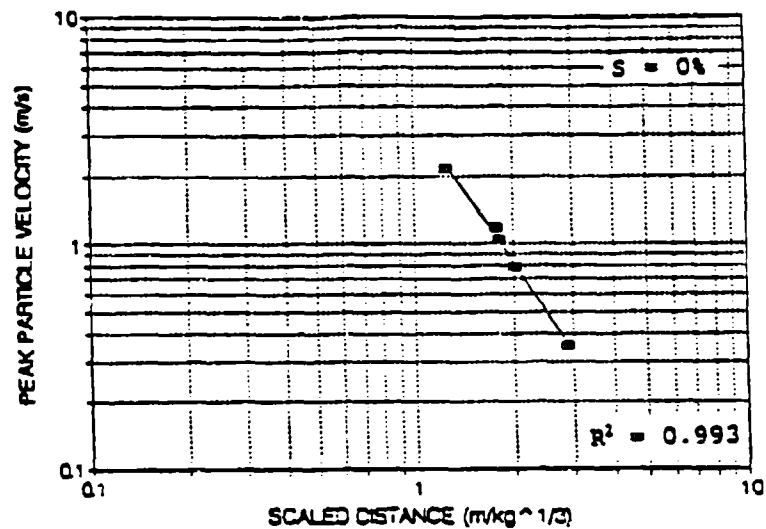Figure 4.9 Peak particle velocity as a function of scaled distance for Tyndall beach sand.

74
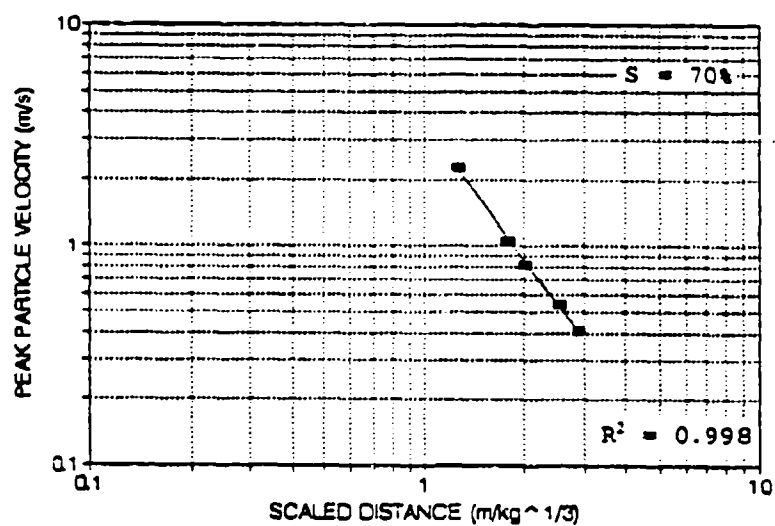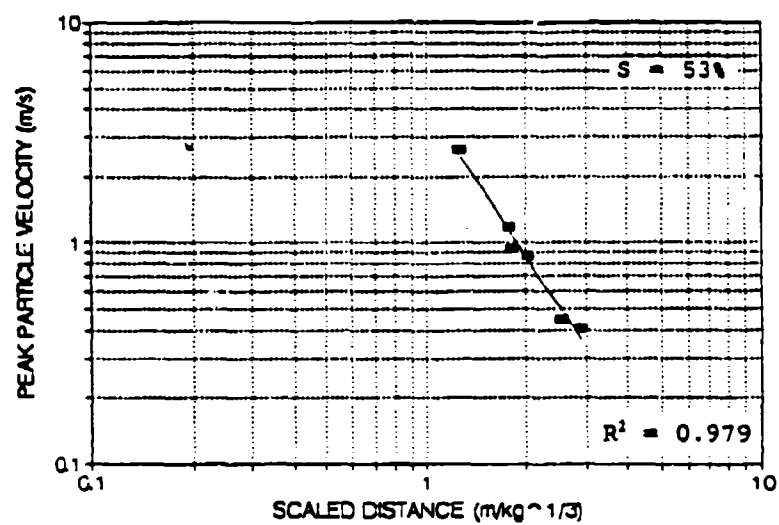
Figure 4.9 (continued) Peak particle velocity as a function of scaled distance for Tyndall beach sand.
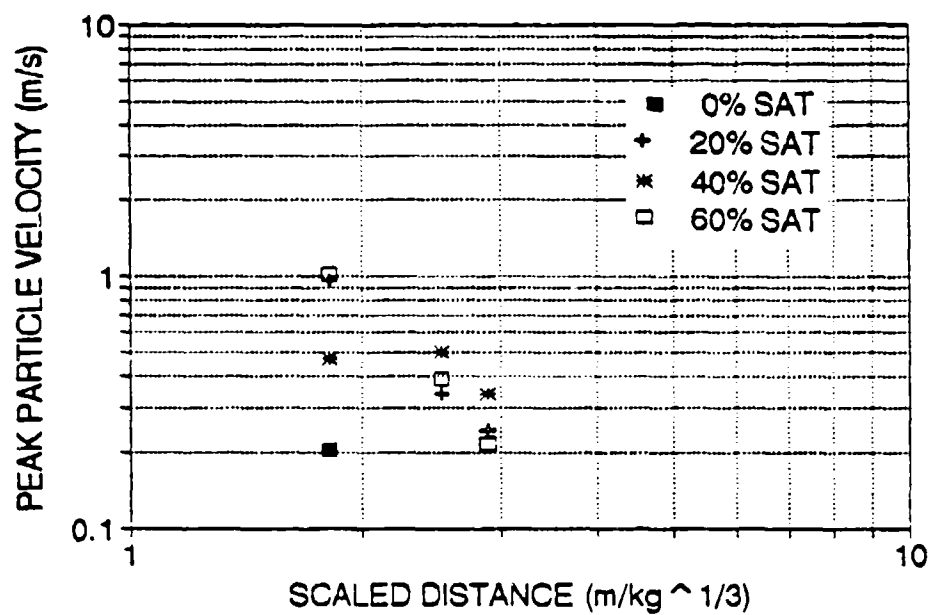
Figure 4.10   Peak particle velocity as a function of scaled distance for Ottawa 20-30 sand.

SECTION V

ANALYSIS OF RESULTS

A. PEAK STRESS, PEAK PARTICLE ACCELERATION, AND PEAK PARTICLE VELOCITY
   PREDICTION EQUATIONS

Free-field stress and ground motion prediction equations from Drake
and Little (1983) were presented in Equations (2.10) through (2.14) of
Section II.A.4. Equations were developed for peak stress, peak particle
acceleration, peak particle velocity, peak particle displacement, and
impulse and are expressed as an equation of a line in the form of Equation
(2.9)

$$y = b(x)^m. \tag{2.9}$$

If the constants b and m are known for a data set, a response equation as
a function of scaled distance can be defined.

Prediction equations for peak stress, peak particle acceleration,
and peak particle velocity on Tyndall beach and Ottawa 20-30 sands are
presented in this section in the form of Equation (2.9). Development of
response equations for peak particle displacement and impulse have not
been pursued and will not be analyzed in this investigation.

1. Equations for Peak Stress

Plots of peak stress versus scaled distance for Tyndall and
Ottawa sands were shown in Figures 4.2 and 4.3. Values of b and m are
determined from these plots for various compaction saturations and are
listed in columns one (1) through three (3) of Tables 5.1a and 5.1b. From
Drake and Little's (1983) equation for stress (Equation (2.10)), the
constant m is denoted by -n and the constant b in SI units is equivalent

Table 5.1a PEAK STRESS, PEAK PARTICLE ACCELERATION AND PEAK PARTICLE VELOCITY EQUATION CONSTANTS FOR TYNDALL BEACH SAND

SATURATION	Stress			Acceleration			Velocity		
	m (-n) (1)	b (kPa) (2)	b (psi) (3)	m (-n-1) (4)	b ($mkg^{1/2}/s^2$) (5)	b ($ftlb^{1/2}/s^2$) (6)	m (-n) (7)	b (m/s) (8)	b (ft/s) (9)
0	-2.61	1820	2870	-3.37	27700	2585800	-2.21	3.76	93.2
17	-2.32	2000	2420	-3.52	38900	4184800	-2.28	4.15	109.9
35	-2.30	2110	2530	-4.27	55000	11766100	-2.53	4.62	154.1
53	-2.30	1970	2350	-3.16	29100	2253300	-2.30	4.20	113.7
70	-2.62	2080	3310	-3.41	33200	3213700	-2.03	3.49	73.7

Table 5.1b PEAK STRESS, PEAK PARTICLE ACCELERATION AND PEAK PARTICLE VELOCITY EQUATION CONSTANTS FOR OTTAWA 20/30 SAND.

SATURATION	Stress			Acceleration			Velocity		
	m (-n) (1)	b (kPa) (2)	b (psi) (3)	m (-n-1) (4)	b ($mkg^{1/2}/s^2$) (5)	b ($ftlb^{1/2}/s^2$) (6)	m (-n) (7)	b (m/s) (8)	b (ft/s) (9)
0	-3.25	1130	3220	*	*	*	*	*	*
20	-3.13	1840	4680	-5.00	48700	20269300	-2.94	5.37	259.6
40	-2.95	1370	2970	-1.39	3000	45000	-0.51	0.67	3.50
60	-2.89	1180	2400	-4.68	35200	10891800	-3.22	6.97	435.1

* Not determined due to inadequate data.

to $f0.049\rho c_c(2.52)^{-n}$. Peak stress equations developed for Tyndall and Ottawa sands are shown in Tables 5.2 and 5.3.

2. Equations for Peak Particle Acceleration

From the scaled peak particle acceleration regressions of Figures 4.7 and 4.8, the constants b and m are obtained for both Tyndall and Ottawa sands and are listed in columns four (4) through six (6) of Tables 5.1a and 5.1b. From Drake and Little's (1983) Equation (2.12) for peak particle acceleration, m is equivalent to $-n-1$ and the constant b in SI units is $f126c_c(2.52)^{-n-1}$. Peak particle acceleration equations for Tyndall and Ottawa sands are given in Tables 5.2 and 5.3.

3. Equations for Peak Particle Velocity

From the peak particle velocity regressions of Figures 4.9 and 4.10, the constants b and m are determined for both Tyndall and Ottawa sands and are listed in columns seven (7) through nine (9) of Tables 5.1a and 5.1b. The constant m is equivalent to $-n$ and b in SI units is $f49(2.52)^{-n}$ from Drake and Little's (1983) peak particle velocity equation (Equation (2.11)). Particle velocity equations for Tyndall and Ottawa sands are given in Tables 5.2 and 5.3.

B. ANALYSIS OF ATTENUATION COEFFICIENTS

The slopes of the least square regression lines from the log-log data for peak stress $(-n)$, peak particle acceleration $(-n-1)$, and peak particle velocity $(-n)$ of Table 5.1 share the common variable n (Drake and Little, 1983). The variable n was defined as the attenuation coefficient in Section II.A.4. Attenuation coefficients for Tyndall and Ottawa sands are plotted as a function of degree of saturation during compaction in Figures 5.1(a) and (b).

Tyndall sand attenuation coefficients (Figure 5.1(a)) display some change over the range of compaction saturations from 0 to 70 percent. The

Table 5.2a STRESS AND GROUND MOTION PREDICTION EQUATIONS DERIVED FROM TYNDALL SAND REGRESSION DATA (SI UNITS).

0% Saturation

$$P = 1820 \left(\frac{R}{W^{1/3}}\right)^{-2.81}$$

$$a\,W^{1/3} = 27700 \left(\frac{R}{W^{1/3}}\right)^{-2.}$$

$$V = 3.76 \left(\frac{R}{W^{1/3}}\right)^{-2.81}$$

17% Saturation

$$P = 2000 \left(\frac{R}{W^{1/3}}\right)^{-2.13}$$

$$a\,W^{1/3} = 38900 \left(\frac{R}{W^{1/3}}\right)^{-3.}$$

$$V = 4.15 \left(\frac{R}{W^{1/3}}\right)^{-2.38}$$

35% Saturation

$$P = 2110 \left(\frac{R}{W^{1/3}}\right)^{-2.30}$$

$$a\,W^{1/3} = 55000 \left(\frac{R}{W^{1/3}}\right)^{-4.}$$

$$V = 4.62 \left(\frac{R}{W^{1/3}}\right)^{-2.53}$$

53% Saturation

$$P = 1970 \left(\frac{R}{W^{1/3}}\right)^{-2.10}$$

$$a\,W^{1/3} = 29100 \left(\frac{R}{W^{1/3}}\right)^{-3.}$$

$$V = 4.20 \left(\frac{R}{W^{1/3}}\right)^{-2.30}$$

70% Saturation

$$P = 2080 \left(\frac{R}{W^{1/3}}\right)^{-2.62}$$

$$a\,W^{1/3} = 33200 \left(\frac{R}{W^{1/3}}\right)^{-3.}$$

$$V = 3.49 \left(\frac{R}{W^{1/3}}\right)^{-2.03}$$

Table 5.2b STRESS AND GROUND MOTION PREDICTION EQUATIONS DERIVED FROM TYNDALL SAND REGRESSION DATA (ENGLISH UNITS).

0% Saturation

$$P = 2870 \left(\frac{R}{W^{1/3}}\right)^{-2.61}$$

$$a\,W^{1/3} = 605400 \left(\frac{R}{W^{1/3}}\right)^{-3}$$

$$V = 28.41 \left(\frac{R}{W^{1/3}}\right)^{-2.31}$$

17% Saturation

$$P = 16720 \left(\frac{R}{W^{1/3}}\right)^{-2.13}$$

$$a\,W^{1/3} = 979800 \left(\frac{R}{W^{1/3}}\right)^{-3}$$

$$V = 33.49 \left(\frac{R}{W^{1/3}}\right)^{-2.38}$$

35% Saturation

$$P = 17460 \left(\frac{R}{W^{1/3}}\right)^{-2.30}$$

$$a\,W^{1/3} = 2754900 \left(\frac{R}{W^{1/3}}\right)^{-3}$$

$$V = 46.97 \left(\frac{R}{W^{1/3}}\right)^{-2.53}$$

53% Saturation

$$P = 16210 \left(\frac{R}{W^{1/3}}\right)^{-2.10}$$

$$a\,W^{1/3} = 527600 \left(\frac{R}{W^{1/3}}\right)^{-3}$$

$$V = 34.65 \left(\frac{R}{W^{1/3}}\right)^{-2.30}$$

70% Saturation

$$P = 22830 \left(\frac{R}{W^{1/3}}\right)^{-2.62}$$

$$a\,W^{1/3} = 752500 \left(\frac{R}{W^{1/3}}\right)^{-3}$$

$$V = 22.46 \left(\frac{R}{W^{1/3}}\right)^{-2.03}$$

Table 5.3a STRESS AND GROUND MOTION PREDICTION EQUATIONS DERIVED FROM TYNDALL SAND (SI UNITS).

0% Saturation	20% Saturation	40% Saturation	60% Saturation
$P = 1130 \left(\dfrac{R}{W^{1/3}}\right)^{-1.35}$	$P = 1840 \left(\dfrac{R}{W^{1/3}}\right)^{-1.13}$	$P = 1370 \left(\dfrac{R}{W^{1/3}}\right)^{-0.98}$	$P = 1180 \left(\dfrac{R}{W^{1/3}}\right)^{-1.09}$
	$\sigma W^{1/3} = 48700 \left(\dfrac{R}{W^{1/3}}\right)^{-1.69}$	$\sigma W^{1/3} = 3000 \left(\dfrac{R}{W^{1/3}}\right)^{-1.59}$	$\sigma W^{1/3} = 35200 \left(\dfrac{R}{W^{1/3}}\right)^{-1.48}$
	$V = 5.37 \left(\dfrac{R}{W^{1/3}}\right)^{-0.64}$	$V = 0.67 \left(\dfrac{R}{W^{1/3}}\right)^{-0.51}$	$V = 6.97 \left(\dfrac{R}{W^{1/3}}\right)^{-1.55}$

Table 5.3b STRESS AND GROUND MOTION PREDICTION EQUATIONS DERIVED FROM TYNDALL SAND (ENGLISH UNITS).

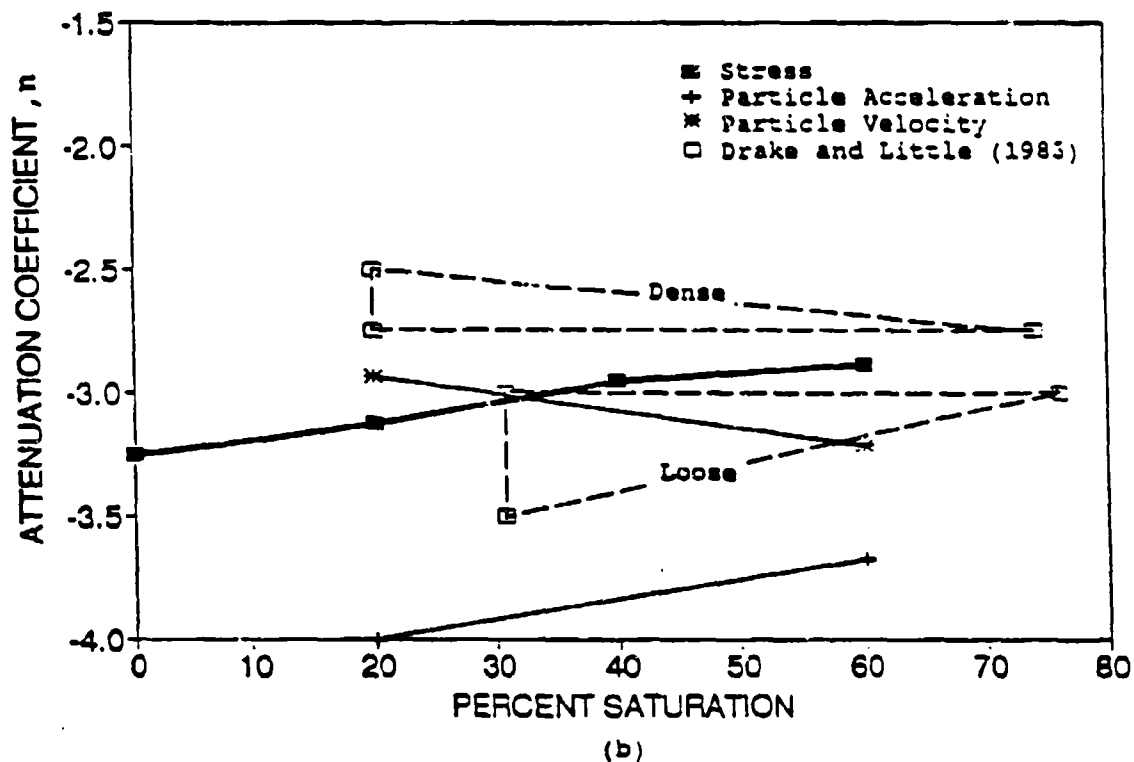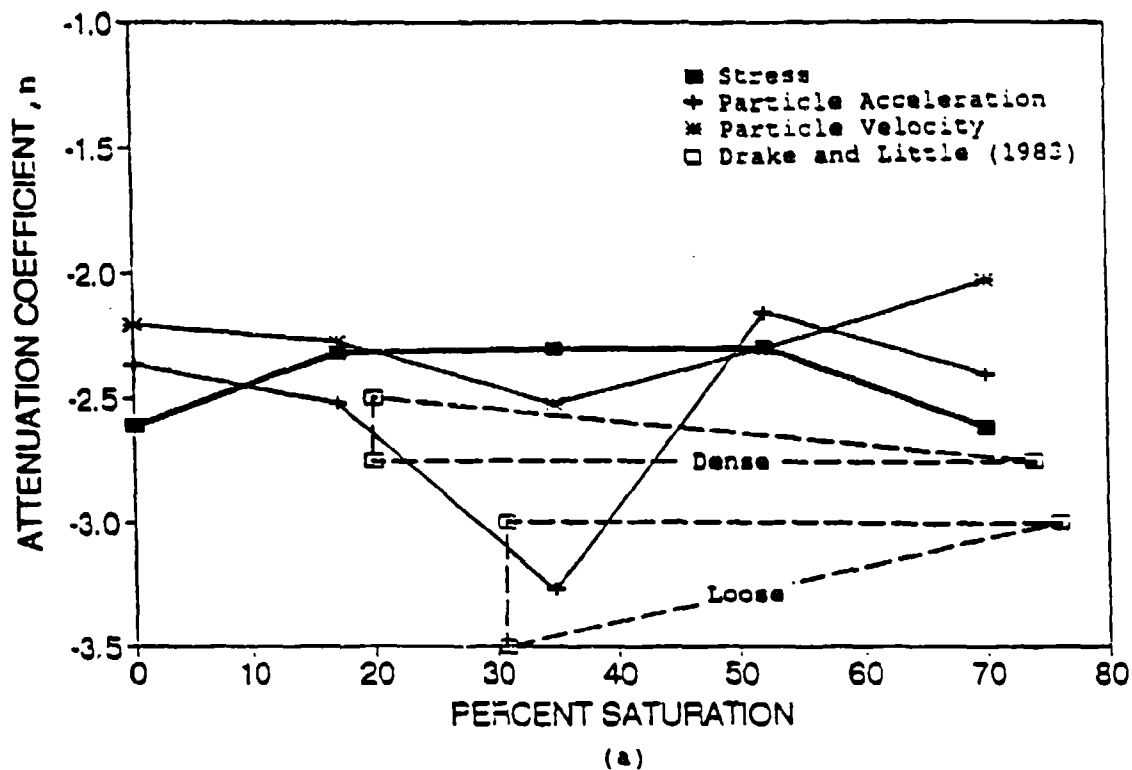| 0% Saturation	20% Saturation	40% Saturation	60% Saturation
$P = 3220 \left(\dfrac{R}{W^{1/3}}\right)^{-0.95}$	$P = 4680 \left(\dfrac{R}{W^{1/3}}\right)^{-1.13}$	$P = 2970 \left(\dfrac{R}{W^{1/3}}\right)^{-0.98}$	$P = 2400 \left(\dfrac{R}{W^{1/3}}\right)^{-1.09}$
	$\sigma W^{1/3} = 20269300 \left(\dfrac{R}{W^{1/3}}\right)^{-1.69}$	$\sigma W^{1/3} = 45000 \left(\dfrac{R}{W^{1/3}}\right)^{-1.59}$	$\sigma W^{1/3} = 10891800 \left(\dfrac{R}{W^{1/3}}\right)^{-1.48}$
	$V = 259.6 \left(\dfrac{A}{W^{1/3}}\right)^{-0.94}$	$V = 3.50 \left(\dfrac{R}{W^{1/3}}\right)^{-0.51}$	$V = 435.1 \left(\dfrac{R}{W^{1/3}}\right)^{-1.32}$

Figure 5.1 Attenuation coefficients as a function of saturation from regressions of stress, particle acceleration, and particle velocity and from Drake and Little (1983). (a) Tyndall beach sand. (b) Ottawa 20-30 sand.

82

attenuation coefficients are in the same range as the assumed envelope of attenuation coefficients (represented by the dotted line) from Drake and Little's (1983) dense and loose sand data. The assumed envelope was constructed with data from Table 2.1, and the dotted line was added to represent data at intermediate saturations which was not available from Drake and Little's results.

Attenuation coefficients for Ottawa sand display little change over the range of compaction saturations. These coefficients again fall in the assumed envelopes of attenuation coefficients from Drake and Little (1983) (Figure 5.1(b)).

C.   ANALYSIS OF INTERCEPTS VALUES

The y-intercepts, b, of the least square regressions for peak stress, scaled peak particle acceleration, and peak particle velocity are given in Table 5.1. Intercepts are determined at a scaled distance of one for both SI and English units of $R/W^{1/3}$. Intercept values in SI units for Tyndall and Ottawa sands are plotted in Figures 5.2(a), (b), and (c) as a function of compaction saturation. Intercept values for peak stress and scaled peak particle acceleration are lowest at 0 and 53 percent saturations and are at a maximum at 35 percent saturation. Intercepts for peak particle velocity are lowest at 0 and 70 percent saturations and again are at a maximum at 35 percent saturation. Minimum and maximum intercept values for both peak stress and scaled peak particle acceleration differ by a factor of two in some instances.

Peak stress intercepts for Ottawa sand follow a similar trend to stress intercepts of Tyndall sand. Due to a lack of accelerometer data for Ottawa sand, representative trends could not be determined for scaled peak particle acceleration and peak particle velocity intercepts. This data is represented by a dotted line.

Intercepts for Tyndall and Ottawa sands in English units are shown in Figures 5.3(a), (b), and (c) as well and exhibit the same trends as

83

Figure 5.2   Intercept values, b, for Tyndall beach and Ottawa 20-30 sands
in SI units.   (a) Peak stress.   (b) Scaled peak particle
acceleration.   (c) Peak particle velocity.
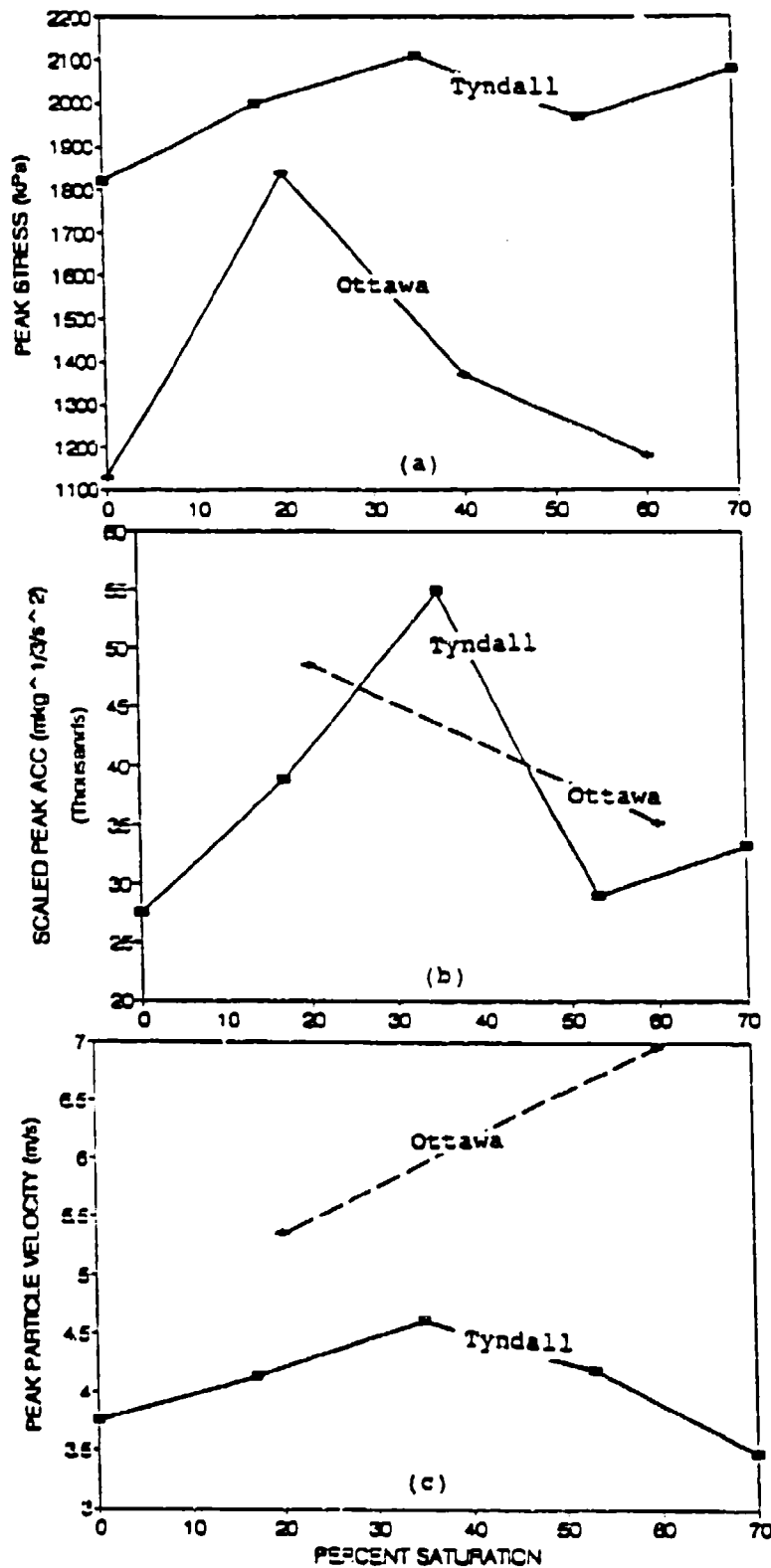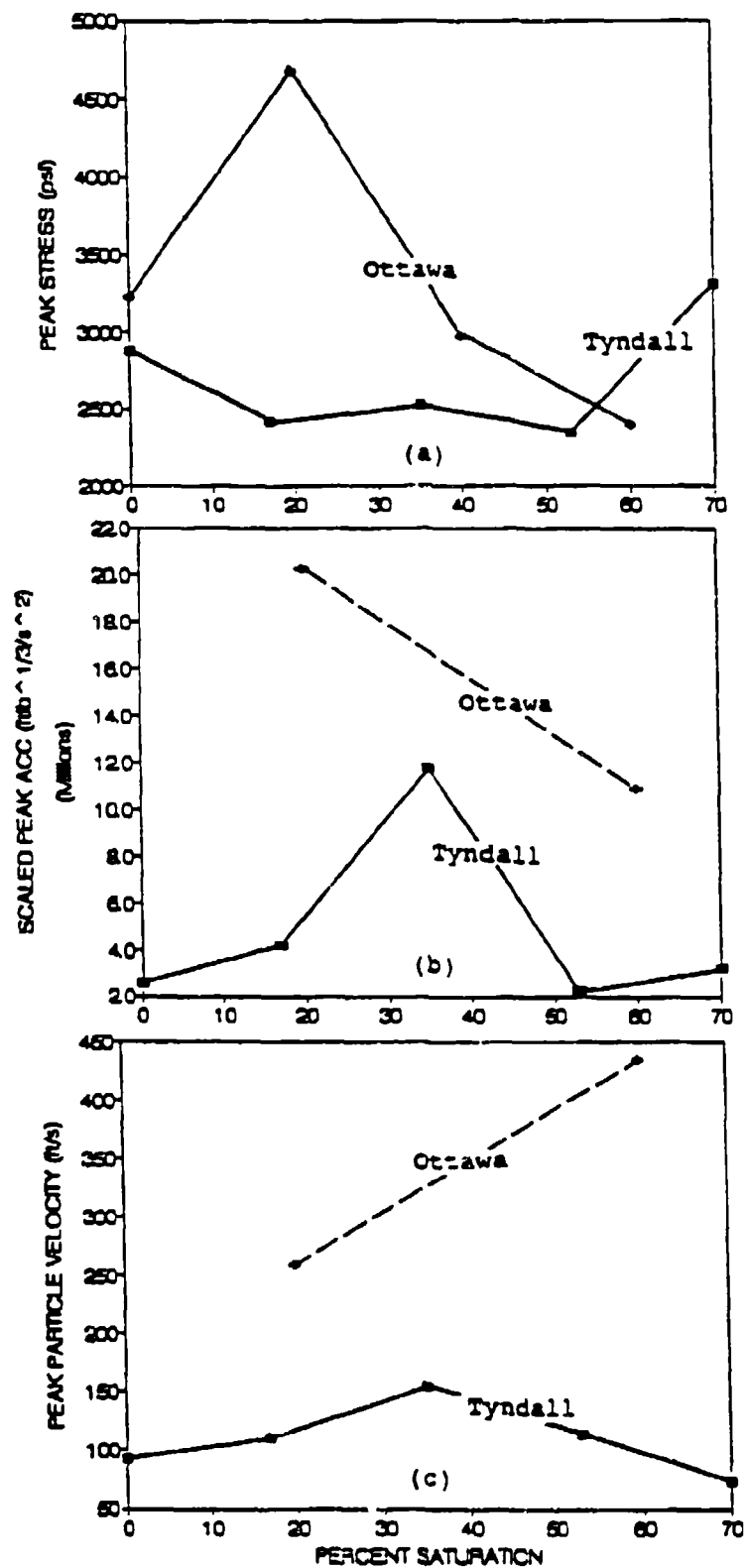
Figure 5.3 Intercept values, b, for Tyndall beach and Ottawa 20-30 sands in English units. (a) Peak stress. (b) Scaled peak particle acceleration. (c) Peak particle velocity.

those in SI units. English unit intercept values can be obtained from SI unit regression lines at a scaled distance of 0.4 $m/kg^{1/3}$.

Wave velocity, stress transmission ratio, peak stress, and shear modulus for sands compacted moist (Ross et al., 1988; Pierce et al., 1989; Charlie et al., 1990; and Wu et al., 1984) display a remarkably similar trend to the intercept values of Figures 5.2 and 5.3 where maximum values occur at intermediate saturations (Section II.B.1.).

Bishop and Blight (1963) suggested that an increase in effective stress in unsaturated soils is due to an increase in the soils capillary pressure. The effective stress increase is the product of the soil saturation, S, and matric suction, $(u_a - u_w)$. Charlie et al. (1990) observed the effects of matric suction on capillary stresses for Silica 50/80 sand. The result was a capillary stress of 0 at a saturation of 0 and 100 percent and a maximum capillary stress at approximately 38 percent saturation (Figure 5.4). Charlie et al. (1990) conducted one dimensional quasi-static compression tests at a constant strain rate on dense silica sand to determine the constrained modulus, M, as a function of saturation. Modulus values for the stress-strain relationships increased up to 34 percent saturation and then decreased with increasing saturation (Figure 5.5). Modulus values followed the same trend as Figure 5.4 for the product of matric suction and saturation, and thus demonstrated a relationship between the degree of saturation during compaction and soil modulus.

Comparing the results of Figure 5.5 for Silica 50/80 sand and the intercept results of Figures 5.2 and 5.3, we conclude that stress wave propagation is a function of modulus as well as compactive saturation.

D.   ANALYSIS OF SEISMIC WAVE VELOCITY AND CONSTRAINED MODULUS

At large distances from a blast soil strains are small and are part of the soils elastic range (strains less than 10^{-4}%). Small strain wave velocity, or seismic velocity, is a basic index of the dynamic response of soils.
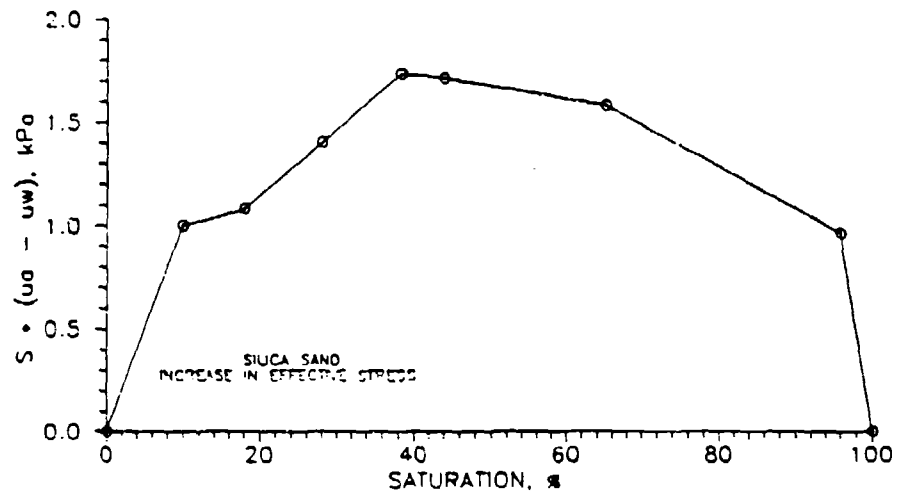
Figure 5.4   Increase in effective stress for 50/80 Silica sand due to saturation and matrix suction (From Charlie et al., 1990).
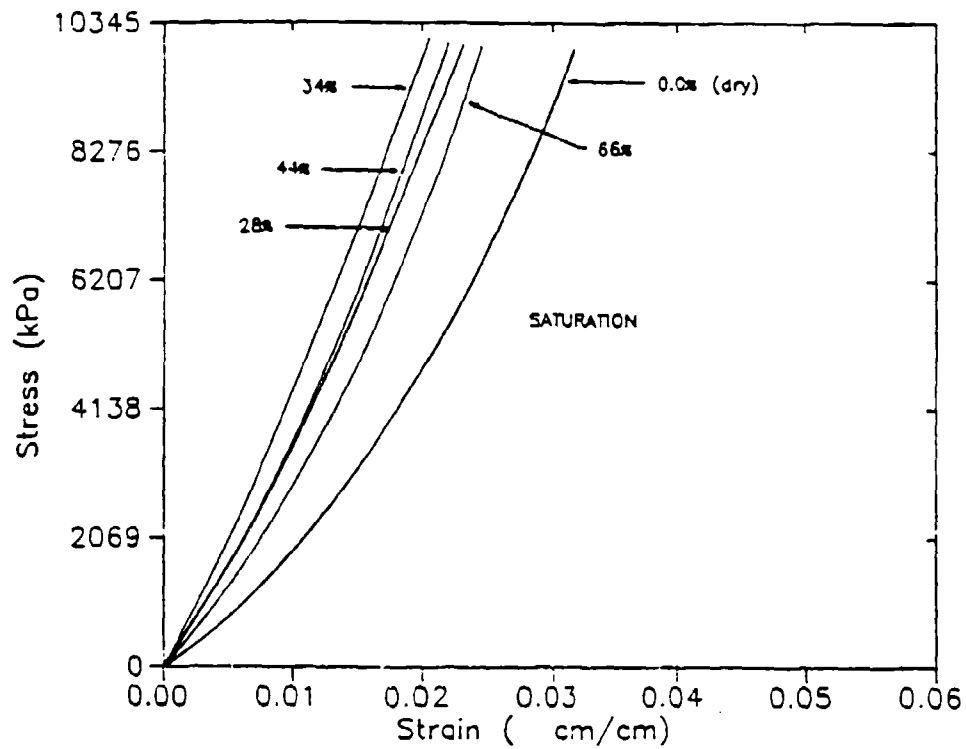

Figure 5.5   Quasi-static stress strain curves for 50/80 Silica sand (From Charlie et al., 1990).

A plot of wave velocity versus scaled distance for dry Tyndall beach sand is shown in Figure 5.6(a). The seismic velocity is approached as the scaled distance increases and the wave velocity becomes relatively constant. An approximate range of seismic velocity can be determined from a log-log plot of the data at a scaled distance of 2.9 $m/kg^{1/3}$ (Figure 5.6(b)). The elastic range for these sands is calculated to be at scaled distances greater than 10 $m/kg^{1/3}$.

Seismic wave velocity approximations for Tyndall sand are shown in column one (1) of Table 5.4a and for Ottawa sand are shown in column one (1) of Table 5.4b. Seismic velocity as a function of saturation is plotted in Figures 5.7(a) and (b).

Seismic velocity taken from Table 2.1 by Drake and Little (1983) for dense and loose sands are shown in column two (2) of Tables 5.4a and 5.4b. Seismic velocities at intermittent saturations are not reported by Drake and Little (1983) and are represented by an envelope of assumed data (Figures 5.7(a) and (b)).

Peak stress and peak particle velocity are related to one another through Equation (2.3). Seismic velocity can be expressed in terms of peak stress and peak particle velocity by rearranging the terms of equation (2.3) Using this relation, seismic velocities for Tyndall sand

$$c_c = \frac{\beta}{\rho V}. \tag{5.1}$$

are determined from peak stresses and peak particle velocities of Figures 4.2 and 4.9 and are shown in column three (3) of Table 5.4a. Peak stresses and peak particle velocities for Ottawa sand are determined from Figures 4.3 and 4.10, and computed seismic velocities are given in column three (3) of Table 5.4b. As shown in Figures 5.7(a) and (b), seismic velocities computed using Equation (5.1) are comparable to the range of measured wave velocities and seismic velocities determined by Drake and Little (1983).

Peak stress and peak particle velocities of Equation (5.1) are assumed to be in the elastic range of the soil, therefore resulting in seismic velocities of the elastic range as well. Peak stress and peak particle velocity values for Tyndall and Ottawa sands in this
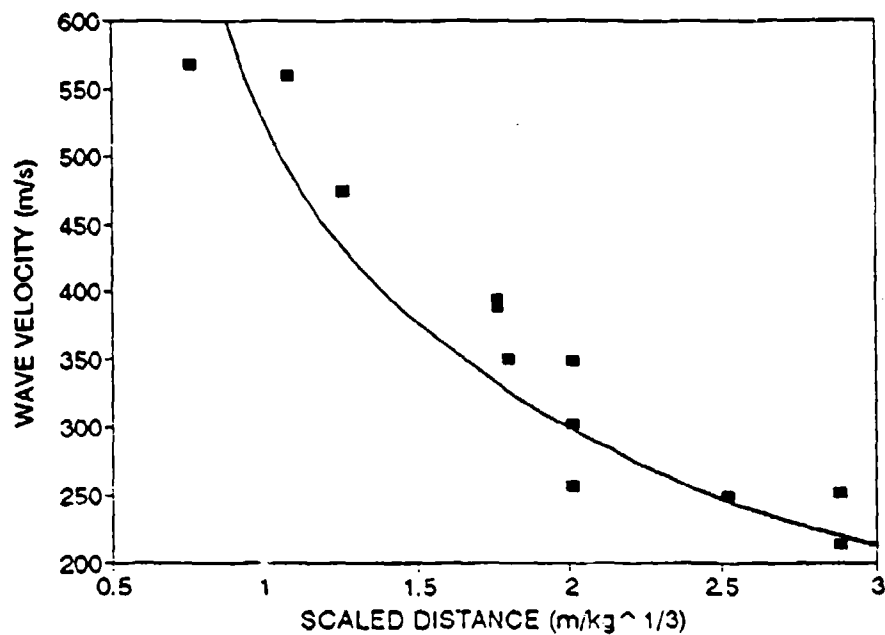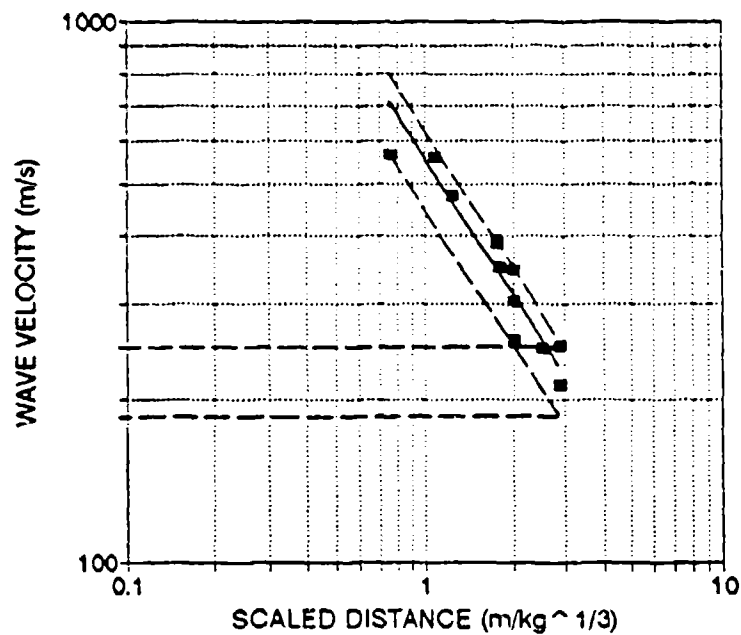
Figure 5.6   Wave velocity versus scaled distance for dry Tyndall beach
            sand.   (a) Normal scale.   (b) Log-log scale approximate
            siesmic velocities at scaled distance of 2.9 m/kg$^{1/3}$.

89

Table 5.4a COMPARISON OF WAVE VELOCITIES FOR TYNDALL BEACH SAND.

Wave Velocity (m/s)

SATURATION	Measured Wave Velocity (1)	Drake & Little (1983) (2)	Eq. 5.1 (3)	Eq. 5.8 (4)
0	200-260		207	384
17	250-360		314	
20		275-396[a]		
31		183[b]		
35	210-290		369	
53	220-370		305	
70	240-400		220	
74		300[a]		
76		152-183[b]		

[a] Determined from dense poorly graded sand.
[b] Determined from loose poorly graded sand.

Table 5.4b COMPARISON OF WAVE VELOCITIES FOR OTTAWA SAND.

Wave Velocity (m/s)

SATURATION	Measured Wave Velocity (1)	Drake & Little (1983) (2)	Eq. 5.1 (3)	Eq. 5.8 (4)
0	130-210		*	525
20	220	275-396[a]	174	
31		183[b]		
40	230-260		94	
60	200-240		146	
74		300[a]		
76		152-183[b]		

* Not determined due to inadequate data.
[a] Determined from dense poorly graded sand.
[b] Determined from loose poorly graded sand.

90
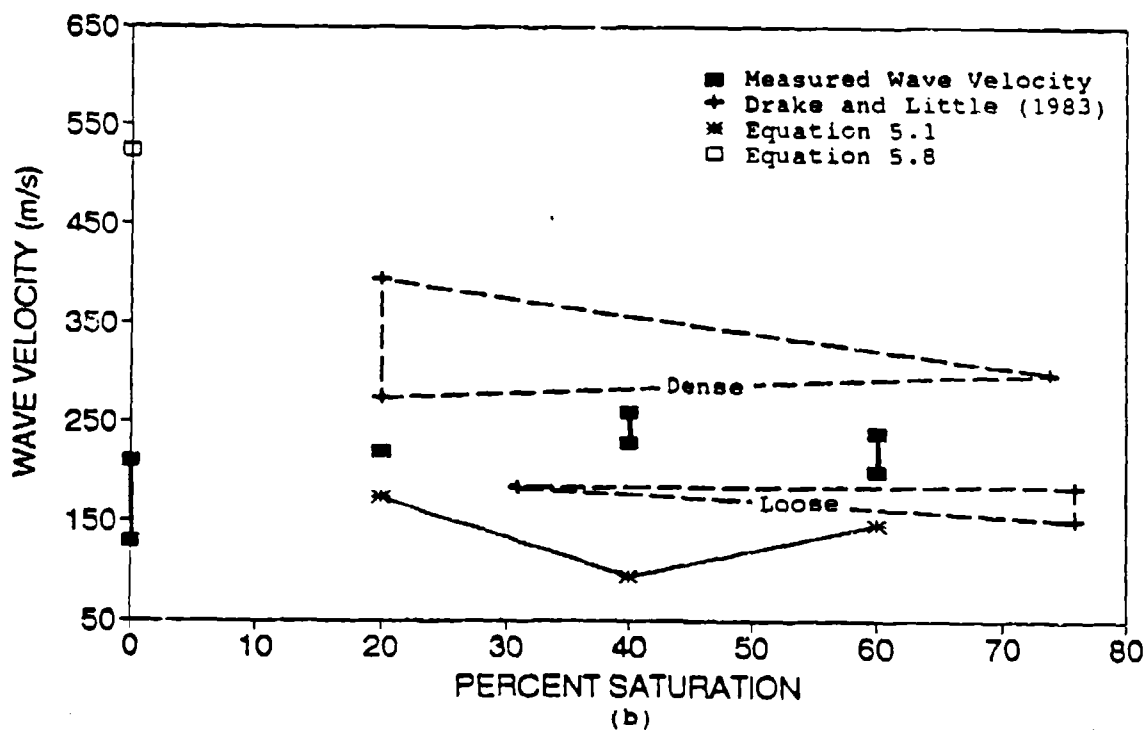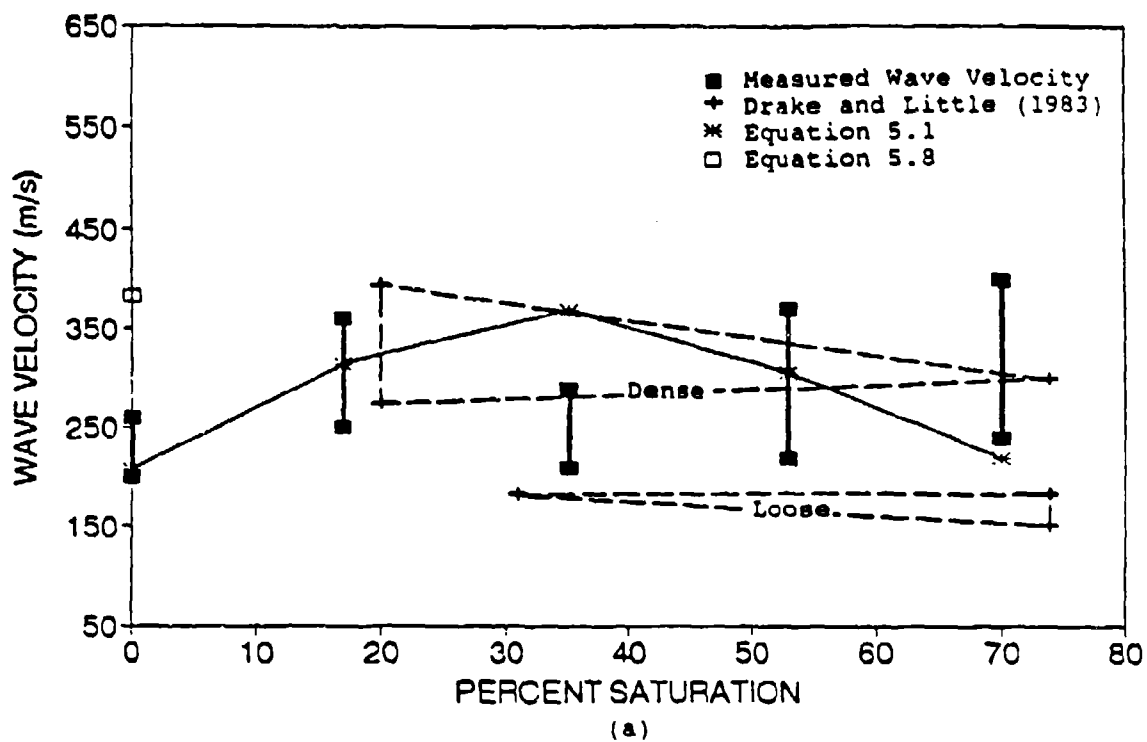
Figure 5.7 Measured wave velocities from centrifuge data at a scaled range of 2.9 m/kg$^{1/3}$, and seismic velocities from Drake and Little (1983), and computed from Equations (5.1) and (5.8). (a) Tyndall beach sand. (b) Ottawa 20-30 sand.

91

investigation are not available from the elastic range. However, values can be obtained from a scaled distance of 2.9 m/kg$^{1/3}$ and will be used herein. The density, ρ, for use in Equation (5.1) for moist specimens is assumed constant as a result of desaturation to the residual saturation (APPENDIX C).

Seismic velocity and constrained modulus are related to one another through Equation (2.4). Rearrangement of Equation (2.4) allows one to solve for M in terms of c_c

$$M = \rho c_c^2. \tag{5.2}$$

Again, the mass density of moist centrifuge specimens is assumed constant due to desaturation. Modulus, therefore, is directly proportional to the square of the seismic velocity. Values of constrained modulus for Tyndall sand are computed from seismic velocities given in column one (1) of Table 5.4a, and are listed in column one (1) of Table 5.5a. The proportional relationship of seismic velocity and modulus is evident as they both display the same unique trend. Modulus values are also determined from measured seismic velocities (column one (1), Table 5.4a) and listed in column two (2) of Table 5.5a.

Values of constrained modulus for Tyndall sand are plotted versus saturation in Figure 5.8(a). For comparison, assumed modulus envelopes for dense and loose sands by Drake and Little (1983) are included in Figure 5.8(a). Values of constrained modulus for Ottawa sand are computed similarly to those of Tyndall sand and are presented along with values from Drake and Little (1983) in Table 5.5b. A plot of modulus versus degree of saturation for Ottawa sand is shown in Figure 5.8(b).

One dimensional quasi-static compression tests at constant strain rate were conducted on Tyndall sand to experimentally determine the constrained modulus at large strains. These results are given in column five (5) of Table 5.5a along with the large strain modulus results of Charlie et al. (1990) from Section V.B. (column (4), Table 5.5a).

92

Table 5.4a COMPARISON OF WAVE VELOCITIES FOR TYNDALL BEACH SAND.

Wave Velocity (m/s)

SATURATION	Measured Wave Velocity (1)	Drake & Little (1983) (2)	Eq. 5.1 (3)	Eq. 5.8 (4)
0	200-260		207	384
17	250-360		314	
20		275-396ᵃ		
31		183ᵇ		
35	210-290		369	
53	220-370		305	
70	240-400		220	
74		300ᵃ		
76		152-183ᵇ		

ᵃ Determined from dense poorly graded sand.
ᵇ Determined from loose poorly graded sand.

Table 5.4b COMPARISON OF WAVE VELOCITIES FOR OTTAWA SAND.

Wave Velocity (m/s)

SATURATION	Measured Wave Velocity (1)	Drake & Little (1983) (2)	Eq. 5.1 (3)	Eq. 5.8 (4)
0	130-210		*	525
20	220	275-396ᵃ	174	
31		183ᵇ		
40	230-260		94	
60	200-240		146	
74		300ᵃ		
76		152-183ᵇ		

* Not determined due to inadequate data.
ᵃ Determined from dense poorly graded sand.
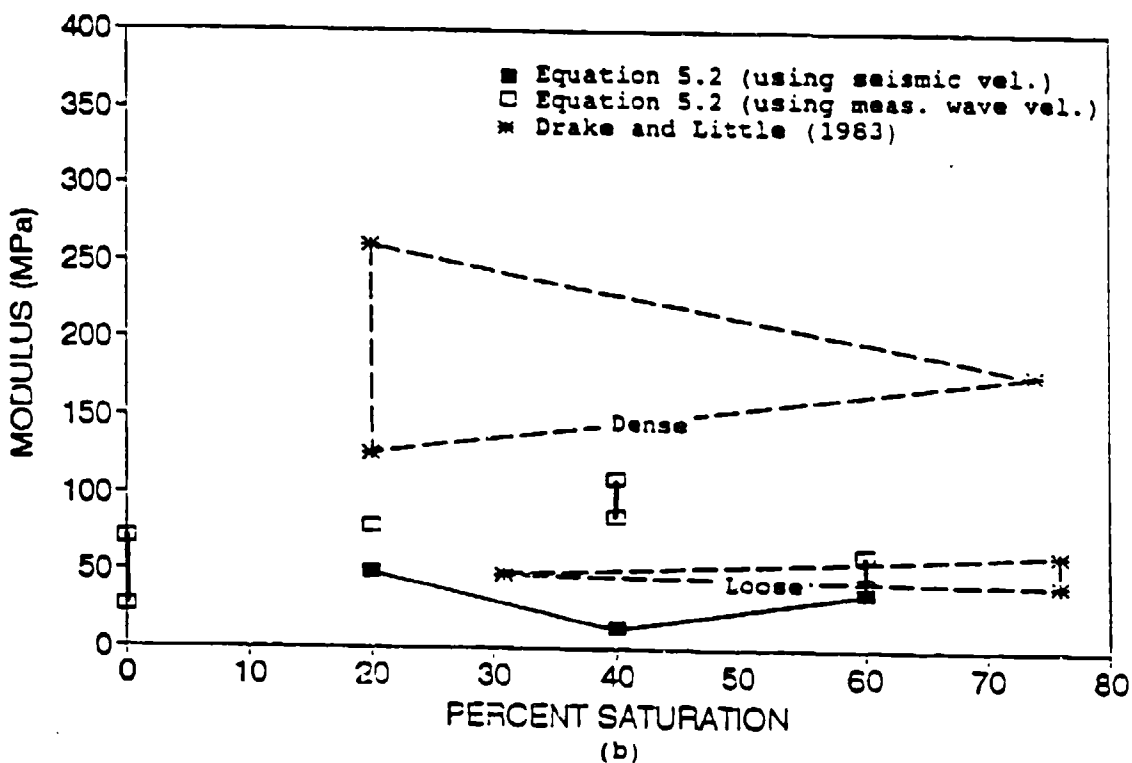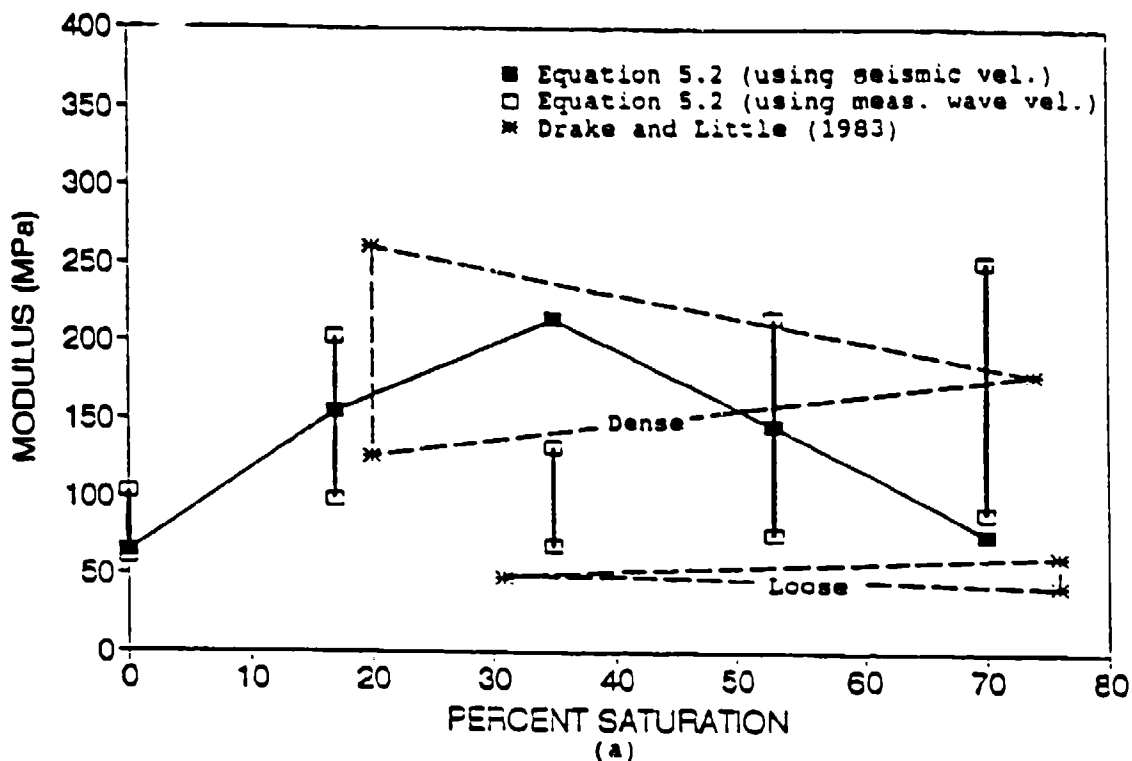ᵇ Determined from loose poorly graded sand.

93

Figure 5.8   Constrained modulus as a function of saturation computed from Equation (5.2) and taken from Drake and Little (1983).   (a) Tyndall beach sand.   (b) Ottawa 20-30 sand.

94

E.   ANALYSIS OF ACOUSTIC IMPEDANCE

The acoustic impedance, ρc_c, is a measure of a soils ability to transmit stress waves. Using Drake and Little's (1983) peak stress equation (Equation (2.10)), one can back calculate ρc_c as a function of stress and scaled distance

$$\rho c_c = \frac{P}{f\ 0.049\left(2.52\dfrac{R}{W^{1/3}}\right)^{-n}}.$$ (5.3)

Acoustic impedance at a scaled distance of 2.9 m/kg$^{1/3}$ is given in column one (1) of Tables 5.6a and 5.6b for Tyndall and Ottawa sands. Back calculating ρc_c using the above equation assumes that the constant $f0.049\rho c_c(2.52)^{-n}$, empirically determined by Drake and Little (1983), is correct.

Acoustic impedance can also be computed as a function of peak stress and peak particle velocity in a form similar to Equation (5.1).

$$\rho c_c = \frac{P}{V}.$$ (5.4)

Values of ρc_c from Equation (5.4) are given in column two (2) of Tables 5.6a and 5.6b for Tyndall and Ottawa sands. Plots of ρc_c for Tyndall and Ottawa sands are shown in Figures 5.9(a) and (b) and include assumed envelopes of ρc_c observed by Drake and Little (1983).

F.   ANALYSIS OF PEAK STRESS

Envelopes of peak stress data taken from Drake and Little (1983) for very loose dry sand, loam loess and dry sand, and very dense sand are shown in Figure 5.10 along with peak stress data for dry dense and medium dense Tyndall and Ottawa sands. Both attenuation and magnitude of peak stresses for the two sets of data are similar. Centrifuge data also extends over a scaled distance similar to that of Drake and Little (also see Figures 4.2 and 4.3).

Table 5.6a COMPARISON OF ACOUSTIC IMPEDANCE FOR TYNDALL BEACH SAND.

ACOUSTIC IMPEDANCE X 10^3 (kg/m^2-s)

SATURATION	Eq. 5.3 (1)	Eq. 5.4 (2)	Drake & Little (1983) (3)
0	272	315	
17	227	492	
20			566[a]
31			262[b]
35	232	579	
53	225	478	
70	285	345	
74			498[a]
76			283-339[b]

[a] Determined from dense poorly graded sand.
[b] Determined from loose poorly graded sand.

Table 5.6b COMPARISON OF ACOUSTIC IMPEDANCE FOR OTTAWA SAND.

ACOUSTIC IMPEDANCE X 10^3 (kg/m^2-s)

SATURATION	Eq. 5.3 (1)	Eq. 5.4 (2)	Drake & Little (1983) (3)
0	290	*	
20	447	283	566[a]
31			262[b]
40	278	154	
60	226	238	
74			498[a]
76			283-339[b]

* Not determined due to inadequate data.
[a] Determined from dense poorly graded sand.
[b] Determined from loose poorly graded sand.
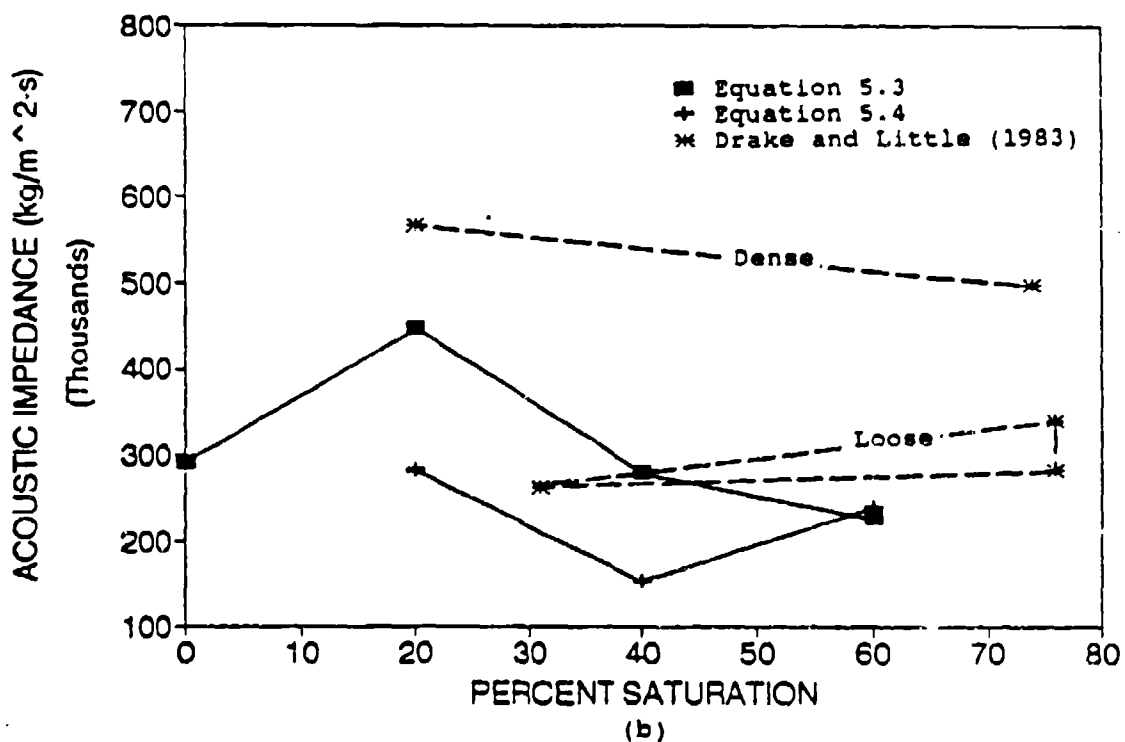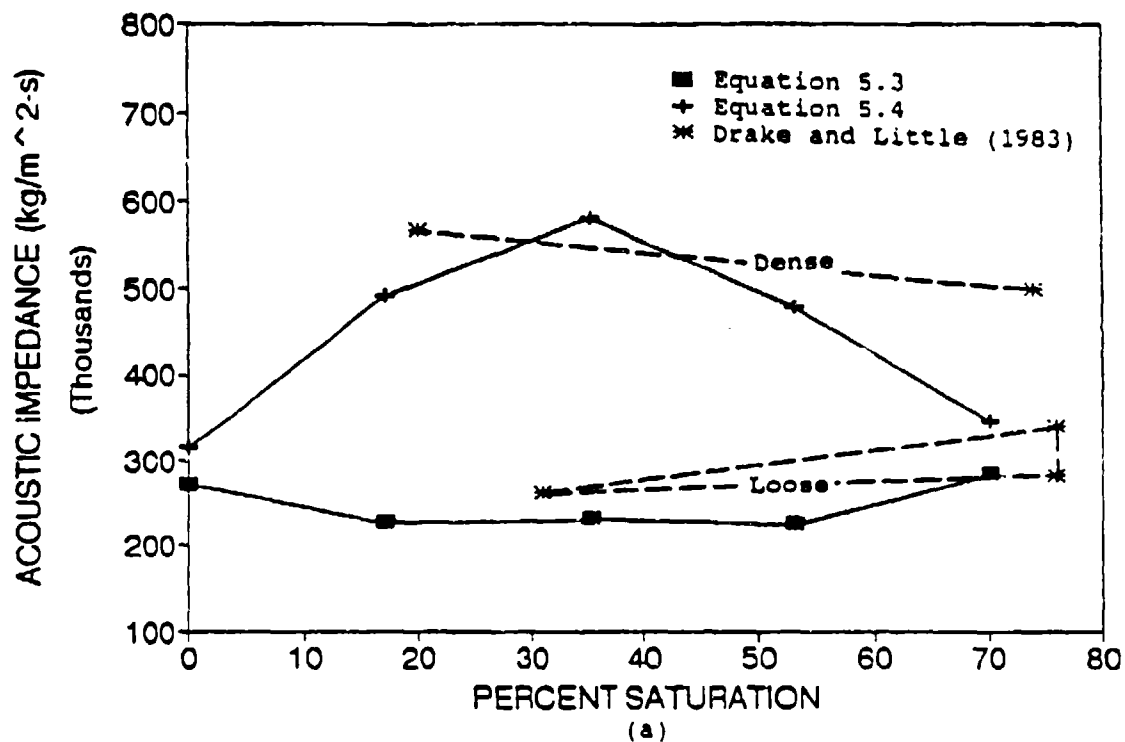
Figure 5.9 Acoustic impedance as a function of saturation computed from Equations (5.3) and (5.4), and taken from Drake and Little (1983). (a) Tyndall beach sand. (b) Ottawa 20-30 sand.
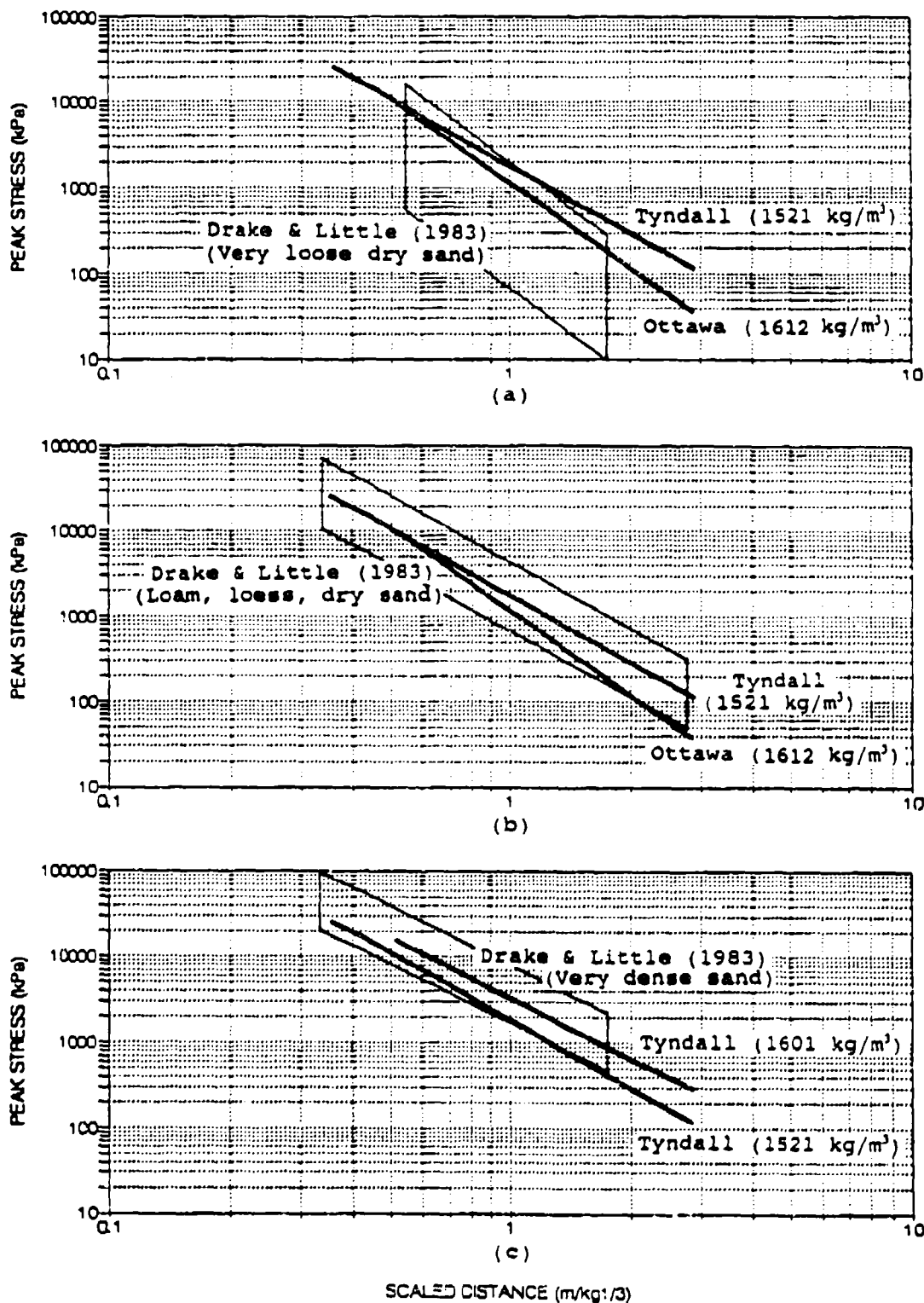
Figure 5.10 Peak stress envelopes versus scaled distance for blast data from Drake and Little (1983). (a) Very loose dry sand. (b) Loam, loess, and dry sand. (c) Very dense sand. Results for dense and medium dense dry Tyndall beach and Ottawa 20-30 sands are also plotted.

98

Plots of peak stress as a function of peak particle velocity for Tyndall beach sand are shown in APPENDIX D.

G.   ANALYSIS OF UNSATURATED SOIL MECHANICS THEORY

Unsaturated soil mechanics theory is based on the linear behavior of soil properties, such as shear strength and strain, between dry and saturated states.   For instance, unsaturated soil mechanics theory by Fredlund (1985), described in Section II.B.3, assumes that shear strength of soil varies linearly with $(\sigma-u_a)$ and (u_a-u_w) (Figure 2.10).   Similarly, Fredlund's (1985) equation for soil strain

$$\epsilon = m_1^e \, d(\sigma-u_a) + m_2^e \, d(u_a-u_w) \qquad (2.22)$$

utilizes the same stress components as does shear $((\sigma-u_a)$ and $(u_a-u_w))$, and given that the compressibility factors m_1^e and m_2^e are constant, then resulting soil strains vary linearly as well.

Pierce (1989) derived an equation to predict modulus for dense Eglin sand by utilizing the experimental results from split-Hopkinson pressure bar testing at various values of $(\sigma-u_a)$ and (u_a-u_w).   Pierce based Equation (5.5) on Fredlund's (1985) Equation (2.22) for strain.

$$M = (1.510 - 0.016(u_a-u_w) + 0.0004(\sigma-u_a)) \; X \, 10^5 \qquad (5.5)$$

(kPa).   Pierce observed that the modulus of Eglin sand was relatively unaffected by changes in pore water pressures but was affected by changes in total stress.   Tests specimens were compacted dry, saturated, and then the water content was adjusted using the pressure plate method.   Pierce's results are supported by Fredlund's theory that pore water pressure has little influence on changing the modulus of the sand.

Results reported by Charlie et al. (1990) for sands compacted moist are not predicted by Fredlund's (1985) theory.   As demonstrated in Figure 5.5, modulus is related to the saturation at the time of compaction and

displays non-linear trends over the range of saturations from 0 to 66 percent. Since modulus is directly related to soil strength, soil strength is assumed to vary non-linearly with the degree of saturation at the time of compaction as well. This would infer that soil properties, such as shear strength and soil strain, also vary non-linearly with modulus and compactive saturation.

Studies by Hardin and Black (1968) on various quantities which influence shear modulus, G_o, of sand have shown that for shearing strain amplitudes less than 10^{-4}%, G_o was essentially independent of each of the variables except effective stress, σ', and void ratio, e. Saturation had little effect on G_o. Hardin and Richart (1963) developed an empirical expression to relate G_o, e, and σ' for round-grained soils

$$G_o = \frac{218 (2.17-e)^2}{1+e} \sqrt{\sigma'} \quad (kPa) .$$ (5.6)

By applying concepts of the theory of elasticity and Equations (2.6) and (2.7), shear modulus can be related to constrained modulus, M, in the form

$$M = \frac{2 (1-\mu) G_o}{1-2\mu} .$$ (5.7)

Substituting constrained modulus into Equation (2.4) yields seismic velocities as a function of e and σ' in the form

$$C_c = \sqrt{\frac{437 \times 10^3 (1-\mu) (2.17-e)^2}{\rho (1-2\mu) (1+e)}} (\sigma')^{1/4} \quad (m/s) .$$ (5.8)

Although Equation (5.8) is easily derived, its validity for moist soils is questionable. The constrained modulus of Equation (5.7) is defined as a function of shear modulus, and shear modulus for sand is experimentally determined dry. The use of Equation (5.8) to derive seismic velocities becomes further complicated when determining effective stress of an unsaturated soil. One must then rely on unsaturated theory such as Equation (2.17) from Bishop (1960).

Seismic velocities for dry Tyndall and Ottawa sands using Equation (5.8) are given in column four (4) of Tables 5.4a and 5.4b.

SECTION VI

SUMMARY, CONCLUSIONS AND RECOMMENDATIONS

A. SUMMARY

The survivability of a buried structure from a nearby blast loading is dependent on the dynamic soil properties of the backfill material around and over the structure. Moisture in the backfill material at the time of compaction has been shown to affect the soil stiffness, therefore, influencing the soils stress transmission ability. This report presents the results of a series of systematic explosive tests, in representative cohesionless backfill material, conducted to determine the effect of saturation at the time of compaction on blast induced stress wave propagation and ground motion response. Tyndall beach and Ottawa 20/30 sands were utilized for the backfill material.

Explosive testing was conducted on the centrifuge in soil models of 1/18.9 and 1/26.3 scale and were accelerated to 18.9 and 26.3 g's respectively. With the use of scaling laws, detonators having 1031 mg and 350 mg of PBX 9407 were used to simulate 6.9 kg and 6.4 kg (7.8 kg and 7.3 kg TNT equivalent) prototype charges respectively. Charges were buried to simulate contained bombs at a depth of burial of 1.4 meters resulting in a ground shock coupling factor of 0.71 $m/kg^{1/3}$ (1.8 $ft/lb^{1/3}$). By using models to simulate prototype blast events, testing could be conducted at a fraction of the money and time required to perform large scale blast testing.

Model and prototype performance are related using a set of parameters known as scaling laws. The Buckingham Pi Theory was used to develop these scaling laws through the principles of dimensional analysis. By using two model charge masses to represent a single prototype TNT

charge mass of approximately 7.5 kg, the principle of "modeling of models" was implemented and provided a check on the consistency of the scaling.

Models were compacted moist to target saturation levels and a constant void ratio using a method of vibration. Compaction by vibration was chosen to be the most efficient means for preparing soil models because of the ability to reproduce uniform specimens and oppose the forces of capillarity.

From blast response data for Tyndall and Ottawa sands, empirical equations for peak stress, peak particle acceleration, and peak particle velocity were developed as a function of compaction saturation. Attenuation coefficients, wave velocities, constrained modulus, and acoustic impedance for Tyndall and Ottawa sands were compared with data from Drake and Little (1983). Intercept values at scaled distances of $1 \text{ m/kg}^{1/3}$ and $1 \text{ ft/lb}^{1/3}$ were analyzed for peak stress, scaled peak particle acceleration, and peak particle velocity.

B.   CONCLUSIONS

1.   Stress and Ground Motion Empirical Equations

Stress and ground motion equations are obtained from least square regression lines of soil response data as a function of scaled distance. These equations are defined by two components: the slope of the regression line (m) or attenuation, and the y-intercept of the line (b) at a scaled distance of one. Slope and intercept values as a function of compaction saturation for Tyndall and Ottawa sands are listed in Tables 5.1a and 5.1b. Prediction equations developed from these constants for peak stress, peak particle acceleration and peak particle velocity are shown in Tables 5.2 and 5.3.

Peak stress, scaled peak particle acceleration, and peak particle velocity intercept values for both Tyndall and Ottawa sands are strongly influenced by compaction saturation. Tyndall sand intercepts for peak stress and scaled peak particle acceleration are lowest at 0 and 53 percent saturations and are at a maximum at 35 percent saturation (Figures

102

5.2(a) and (b)). Intercepts for peak particle velocity are lowest at 0 and 70 percent saturations and again are at a maximum at 35 percent saturation (Figure 5.?(c)). Peak stress intercept values for Ottawa sand follow a similar trend to stress intercept values of Tyndall sand (Figure 5.3(c)). Minimum and maximum intercept values for Tyndall scaled peak particle accelerations and Ottawa peak stresses differ by a factor of two. Because of limited data obtained for Ottawa sand, intercept trends could not be observed for scaled peak particle acceleration and peak particle velocity.

2.   Comparison with Split-Hopkinson Pressure Bar Tests

Wave velocity, constrained modulus, and acoustic impedance were computed from response data for Tyndall sand. Results display minimum values at 0 and 70 percent saturations and are maximum at the mid saturations (Figures 5.7, 5.8 and 5.9). Similar trends were observed for Tyndall and Ottawa sand intercept values. This trending pattern closely compares to the trending pattern for wave velocity and stress transmission ratio observed by Ross et al. (1988), Pierce et al. (1989), and Charlie et al. (1990) on the SHPB (Section II.B.1.). Centrifuge results thus indicate that an increase in blast induced stress transmission occurs for soils compacted over the mid saturation range.

3.   C_ _ .-i ith Drake and Little (1983) Blast Testing

Both attenuation and magnitude of peak stress as a function of scaled distance for dry Tyndall and Ottawa sands compare closely to peak stress data from Drake and Little (1983) (Figure 5.10). Attenuation coefficients, wave velocity, constrained modulus, and acoustic impedance determined from centrifuge modeling closely approximate proximity to those obtained by Drake and Little (Figures 5.1, 5.7, 5.8, and 5.9). This demonstrates the centrifuges ability to model large scale stresses as a result of blast loading. Verification of prototype explosive events is currently being conducted by Villano (1992) and Dowden (1992).

4.   Comparison with Unsaturated Soil Mechanics Theory

Finally, results by Ross et al. (1988), Pierce et al. (1989), and Charlie et al. (1990), along with the results presented in this investigation, do not agree with unsaturated soil mechanic theory by Fredlund (1985). As demonstrated in this investigation, the non-linear behavior of constrained modulus as a function of compactive saturation does not follow the linear shear stress and matric suction relationship proposed by Fredlund (Figure 2.10). Centrifuge results indicate that greater shear stresses are developed in soils compacted in the mid saturations.

C.   RECOMMENDATIONS FOR DESIGN

Explosive test results for Tyndall beach and Ottawa 20-30 sands compacted moist (saturations ranging from approximately 20 to 50 percent) indicate that Equations (2.10) to (2.12), developed by Drake and Little (1983), underpredict peak stress, peak particle velocity and peak particle acceleration by a factor of about two. Therefore, for cohesionless backfill sands compacted moist, it is recommended that the predicted values for peak stress, peak particle velocity and peak particle acceleration be doubled for design purposes.

REFERENCES

American Society for Testing and Materials, "Annual Book of ASTM Standards", 1987.

Anonymous, "Structures to Resist the Effects of Accidental Explosions", Air Force, AFR 88-22, Nov. 1990, Unlimited Distribution.

Baker, W. E., Kulesz, J. J., Westine, P. S., Cox, P. A. and Wilbeck, J. S., "A Manual for the Prediction of Blast and Fragment Loadings on Structures," U.S. Army Engineer Division, Huntsville, Alabama, Nov. 1980, 738 pp.

Bishop, A. W., Alpan, I., Blight, G. E., and Donald, I. B., "Factors Controlling the Strength of Partly Saturated Cohesive Soils," Research Conference on Shear Strength of Cohesive Soils, ASCE, University of Colorado, Boulder, Colorado, June 1960, pp. 503-532.

Bishop, A. W. and Blight, G. E., "Some Aspects of Effective Stress in Saturated and Partly Saturated Soils," Geotechnique, Vol. 13, No. 3, Sept. 1963, pp. 177-197.

Blight, G. E., "Effective Stress Evaluation for Unsaturated Soils," Journal of the Soil Mechanics and Foundations Division, ASCE, Vol. 93, No. SM 2, March 1967, pp. 125-148.

Bradley, D. M., Townsend, F. C., Fagundo, F. E. and Davidson, J. L., Centrifugal Scaling Laws for Ground Launch Cruise Missile Shelter, ESL-TR-84-07, Air Force Engineering and Services Center (RDCS), Tyndall Air Force Base, Florida, April 1984, 90 pp.

Buckingham, E., "Model Experiments and the forms of Empirical Equations," Transactions, ASME, Vol. 37, June 1915, pp. 551.

Charlie, W. A. and Pierce, S. J., "High Intensity Stress Wave Propagation in Partially Saturated Sand," Contract No. F49620-87-0004, Air Force Engineering and Services Center (RDCS), Tyndall Air Force Base, Florida, Sept. 1988.

Charlie, W. A., Ross, C. A. and Pierce, S. J., "Split-Hopkinson Pressure Bar Testing of Unsaturated Sand," Geotechnical Testing Journal, ASTM, Vol. 13, No. 4, Dec. 1990, pp. 291-300.

Charlie, W. A. and Walsh, A. J., "Centrifuge Modeling of Explosive Induced Stress Waves in Unsaturated Sand," Contract No. F4962-88-C0053, Air Force Engineering and Services Center (RDCS), Tyndall Air Force Base, Florida, Sept. 1990, 14 pp.

Dowden, N. A., "Centrifuge and Small Scale Modeling of Stress Wave Propagation in Unsaturated Poudre Valley Sand", Masters Thesis, Department of Civil Engineering, Colorado State University, Ft. Collins, Colorado, Spring 1993.

Dowding, C. H., Blast Vibration Monitoring and Control, Prentice-Hall, Inc., Englewood Cliffs, NJ, 1985, pp. 6-52.

Drake, J. D. and Little, C. D., "Ground Shock from Penetrating Conventional Weapons," Symposium Proceedings from The Interaction of Non-Nuclear Munitions with Structures, U.S. Air Force Academy, Colorado, May 1983, pp. 1-6.

Fredlund, D. G., The Behavior of Unsaturated Soils, Saskatoon, Saskatchewan, Canada, Unpublished Manuscript, 1981.

Fredlund, D. G., "Soil Mechanics Principles That Embrace Unsaturated Soils," Eleventh International Conference of Soil Mechanics and Foundation Engineering, ISSMFE, Saskatoon, Saskatchewan, Canada, Vol. 2, 1985, pp. 465-471.

Hardin, B. O. and Black, W. L., "Vibration Modulus of Normally Consolidated Clay," Journal of Soil Mechanics and Foundation Div., ASCE, Vol. 94, No. SM 2, March 1968, pp. 353-369.

Hardin, B. O. and Richart, F. E., Jr., "Elastic Wave Velocities in Granular Soils," Journal of Soil Mechanics and Foundation Div., ASCE, Vol. 89, No. SM 1, Feb. 1963, pp. 33-65.

Holloway, D. C., Wilson, W. H. and Bjarnholt, G., "Use of Ordinary Carbon Resistors as Piezoresistive Transducers to Dynamically Measure Borehole Pressures," Proceedings of the 1985 Society for Experimental Mechanics, Grenelefe, Florida, Nov. 1985.

Holtz, R. D. and Kovacs, W. D., An Introduction to Geotechnical Engineering, Prentice-Hall, Englewood Cliffs, NJ, 1981, pp. 166-178.

Kline, S. J., Similitude and Approximation Theory, McGraw-Hill Book Company, New York, NY, 1965, pp. 1-35.

Ko, H-Y., "Summary of the State-of-the-art in Centrifuge Model Testing," Proceedings of the Centrifuges in Soil Mechanics, Paris, France, 1988, pp. 11-18.

Kolsky, H., Stress Waves in Solids, Dover Publications, Inc., New York, NY, 1963, 210 pp.

Lambe, T. W. and Whitman, R. V., Soil Mechanics, John Wiley and Sons, Inc., New York, NY, 1969, pp. 151-161.

McWhorter, D. B. and Sunada, D. K., Ground-Water Hydrology and Hydraulics, Water Resources Publications, Littleton, Colorado, 1977, 290 pp.

Pierce, S. J., Charlie, W. A. and Ross, C. A., "High Amplitude Stress Wave Propagation in Moist Sand," Proc. of the Fourth Intl. Symposium on the Interaction of Non-nuclear Munitions with Structures, Vol. 1, Panama City Beach, Florida, April 1989, pp. 331-335.

Rinehart, J. S., Stress Transients in Solids, Hyper Dynamics, Santa Fe, NM, 1975, 230 pp.

Ross, C. A., Thompson, P. Y. and Charlie, W. A., "Moisture Effects on Wave Propagation in Soils," Abstracts from ASCE/EMD Specialty Conference, Blacksburg, VA, 1988.

Schmidt, R. M., "Scaling Considerations for Dynamic Experiments," Intl. Confr. on Recent Advances in Geotechnical Earthquake Engineering and Soil Dynamics, Rolla, Missouri, April-May 1981, pp. 1111-1113.

Shukla, A. and Prakash, V., "Wave Propagation in Porous Media as a Function of Fluid Saturation," Proceedings of the Society for Experimental Mechanics, Inc., Vol. XLVII, Portland, Oregon, March 1988, pp. 80-87.

Terzaghi, K., _Theoretical soil Mechanics_, John Wiley and Sons, Inc., New York, NY, 1943, 510 pp.

Veyera, G. E. and Fitzpatrick, B. J., "Stress Transmission and Microstructure in Compacted Moist Sand," Contract No. F49620-88-C-0053/SB5881-0378, Air Force Engineering and Services Center, Tyndall Air Force Base, Florida, Dec. 1990, 56 pp.

Villano, E. J., "Small Scale Modeling of Stress Wave Propagation in Unsaturated Sand", Masters Thesis, Department of Civil Engineering, Colorado State University, Ft. Collins, Colorado, Spring 1993.

Wu, S., Gray, D. H. and Richart, F. E., "Capillary Effects on Dynamic Modulus of Sands and Silts," _Journal of Geotechnical Engineering_, ASCE, Vol. 110, No. 9, Sept. 1984, pp. 1188-1203.

(the reverse of this page is blank)

APPENDIX A

DERIVATION OF SCALING LAWS

The Buckingham Pi theory acts as a means to relate functions expressed in terms of dimensional units and functions of non-dimensional units. A non-dimensional quantity is defined as any quantity formed in such a way that all the units identically cancel. In evaluating models, it is necessary to define a function relating all the parameters of the modeled system. Buckingham (1915) proposed a theory which eliminates the need to know the function, allowing direct similitude through non-dimensional π terms.

In any given physical system there exists one or more dependent parameters which in turn are a function of independent parameters. Independent parameters are those quantities which are necessary to fix location inside a given problem, whereas dependent parameters are dependent upon the location. If q_1 is a dependent parameter and q_2, q_3, ... q_m are independent, we may write

$$q_1 = f(q_2, q_3, \ldots, q_m) . \tag{A.1}$$

Equation (A.1) can be mathematically expressed as

$$f(q_1, q_2, q_3, \ldots, q_m) = 0 \tag{A.2}$$

and parameters can be combined to form non-dimensional π terms such that

$$f(\pi_1, \pi_2, \ldots, \pi_n) = 0 \tag{A.3}$$

The number of π terms, n, is related by

$$n = m - k \qquad (A.4)$$

where m is the number of q's, and k, from Buckingham's (1915) original formulation of the theorem, is equal to the minimum number of independent dimensions required to construct the dimensions of all other parameters q_1, q_2, ... q_m. In conclusion, if all of the relevant parameters are included in Equation (A.2), then similitude between model and prototype can be achieved with the dimensionless π terms such that

$$\pi_{model} = \pi_{prototype}. \qquad (A.5)$$

Derivation of the scaling laws of Table 2.2 are based on Equation (A.5). As an example, using the dimensionless π term, Lgρ/E, we can assume where m represents the model, p represents the prototype and

$$\frac{L_m g_m \rho_m}{E_m} = \frac{L_p g_p \rho_p}{E_p} \qquad (A.6)$$

 L = linear dimension;

 g = gravitational force;

 ρ = mass density; and

 E = modulus of elasticity.

The majority of scaling literature assumes that materials used in the prototype are the same as what is used to construct the model, or at least that the material properties will be kept constant (Bradley et al., 1984). Therefore, $E_m = E_p$ and $\rho_m = \rho_p$, and Equation (A.6) becomes

$$L_m g_m = L_p g_p. \qquad (A.7)$$

Since the prototype is assumed to be at 1 g, $g_p = 1$, and setting $g_m = N$, we arrive at the first scaling law

$$L_p = L_m N. \qquad (A.8)$$

The length term, L, and the gravity term, N, are used to derive the other scaling laws of Table 2.2. A complete derivation of Table 2.2 is conducted by Bradley et al. (1984).

APPENDIX B

INSTRUMENTATION CALIBRATION

A.   STRESS GAGE CALIBRATION RESULTS

Quasi-static stress-voltage relationships for the carbon stress gages were experimentally determined. This procedure consisted of vertically loading eight 4-inch columns of Tyndall Beach sand in increments of 2.2 kN (500 lb). The sand was confined in rigid stainless steel cylinders (Figure B.1) with a carbon gage placed at a depth of 2.54 cm. A calibrated load cell attached to the loading machine was used for direct load readings while corresponding carbon resistance change was measured with a digital volt meter after being amplified by n Ectron signal conditioner. Voltages for amplification gain were corrected.

For pressures up to 19 MPa, linear stress-voltage relationships resulted (Figure B.2). Eight resistors were calibrated in this manor and a mean regression slope of 190.7 MPa/volt was used for the calibration of all gage resistors used in this research effort (Figure B.3).

B.   ACCELEROMETER CALIBRATION RESULTS

Calibration of accelerometers for this research was conducted by the manufacturer (ENDEVCO). Calibration curves for the accelerometers and their sensitivities are shown in Figure B.4. All calibrations are traceable to the National Bureau of Standards.
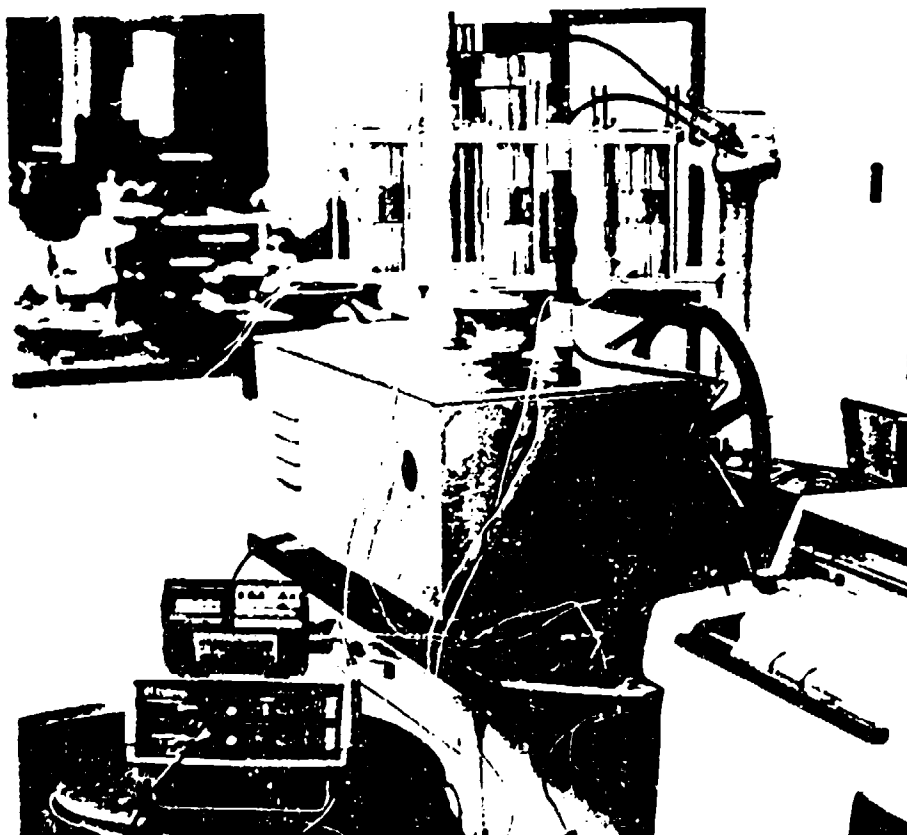
Figure B.1 Calibration of carbon stress gages from a vertical load in stainless steel cylinders.
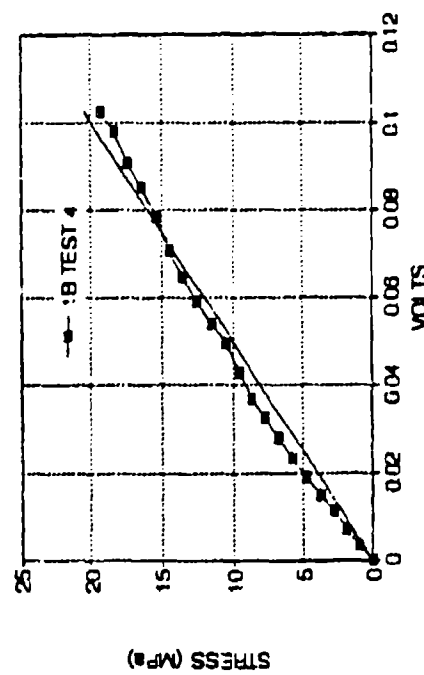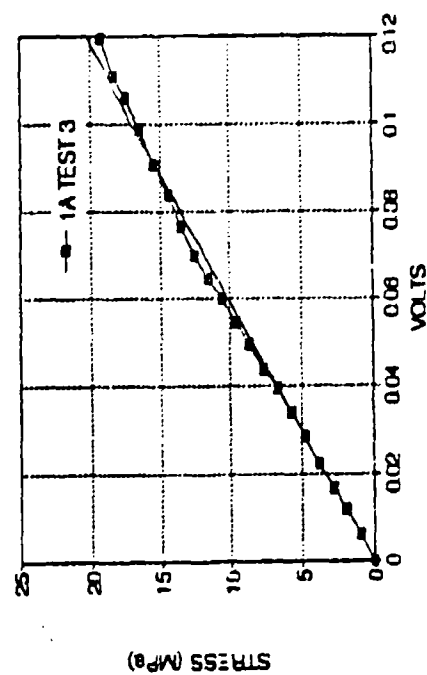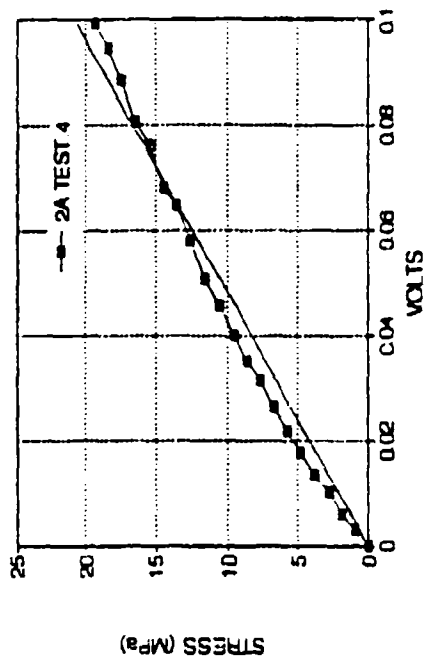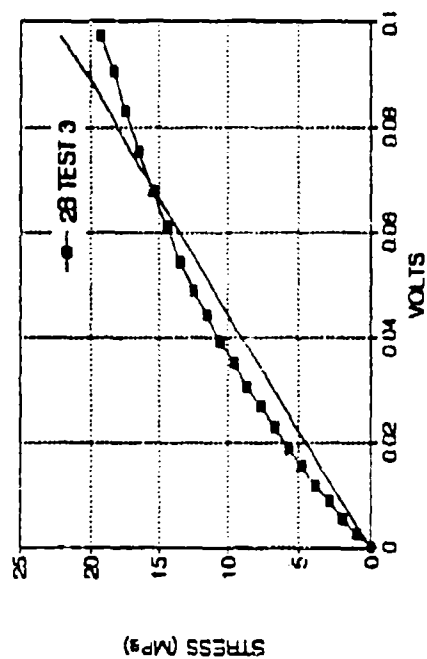
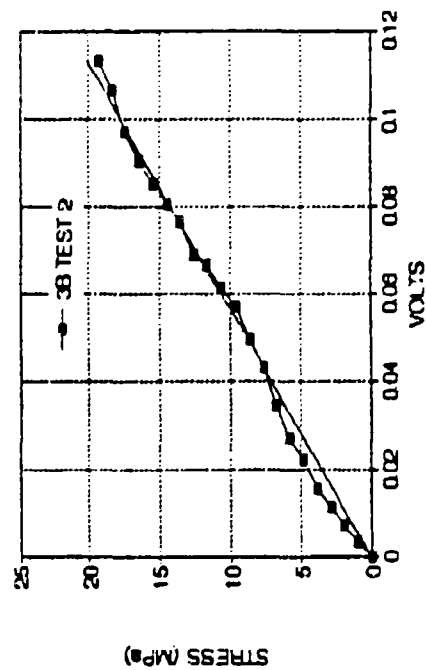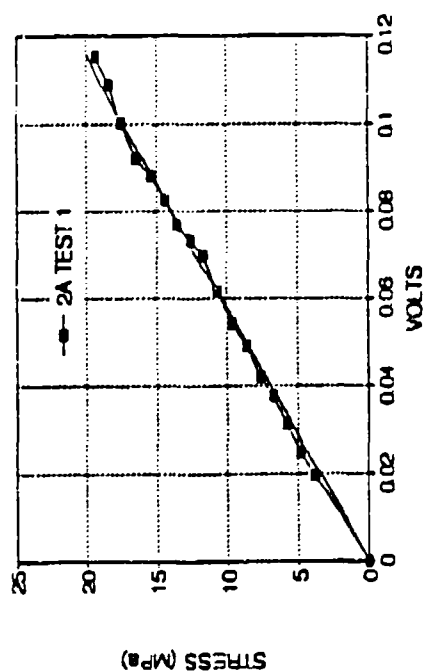Figure B.2 Stress-voltage relationships and regressions for carbon stress gages.
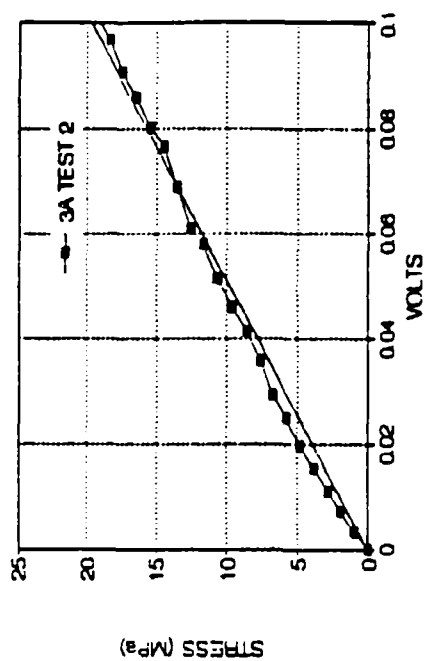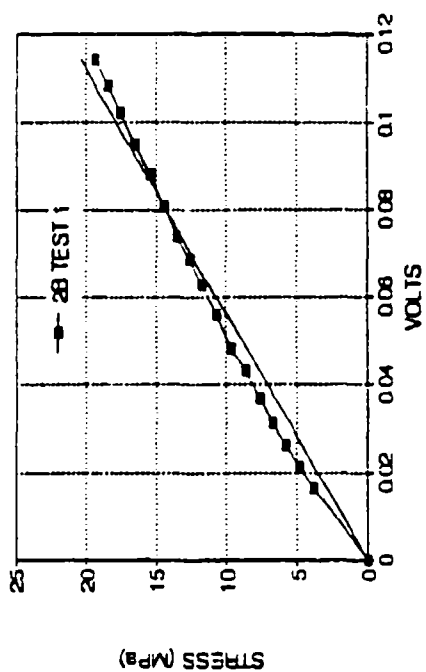
113

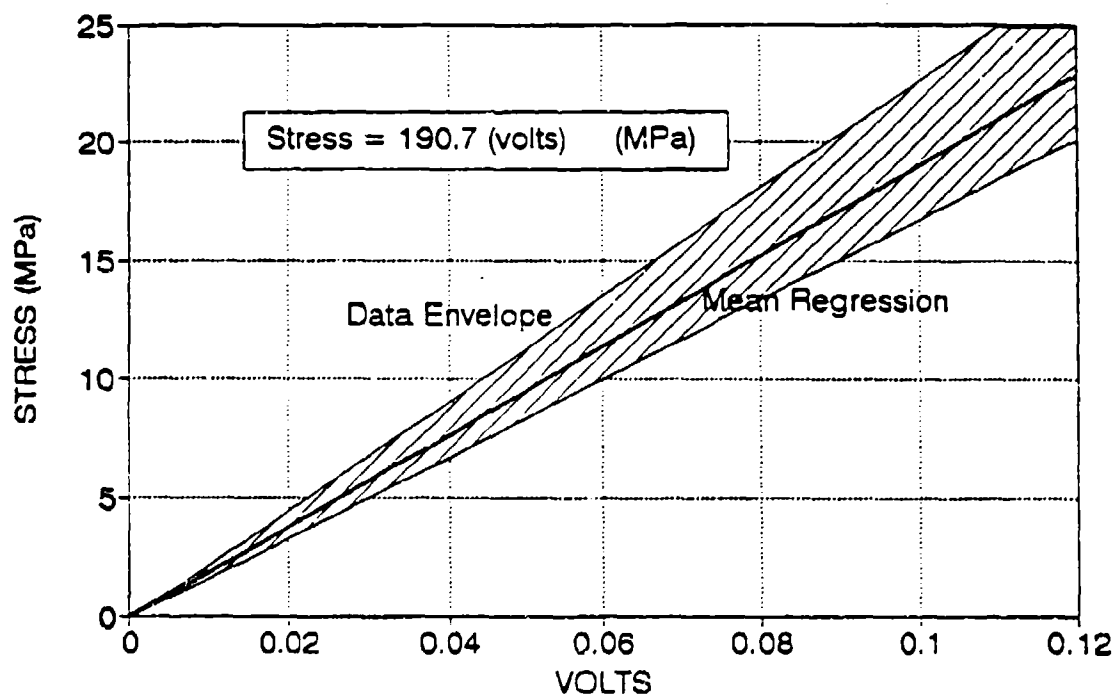Figure B.2 (continued) Stress-voltage relationships and regressions for carbon stress gages.

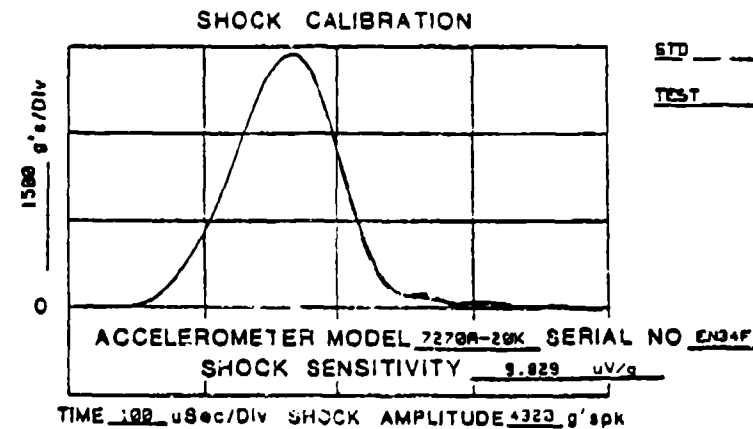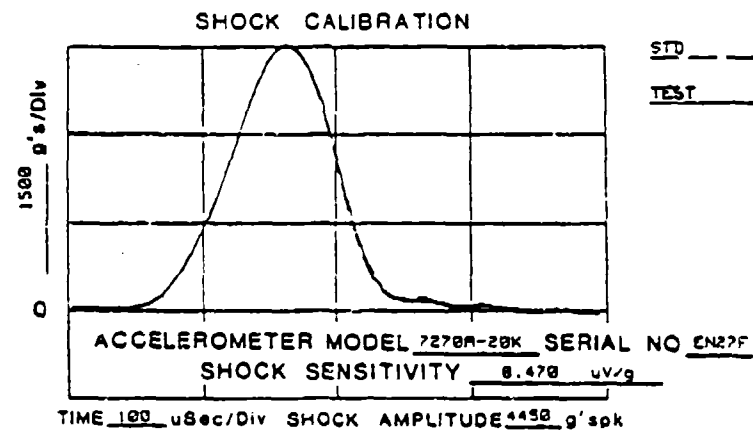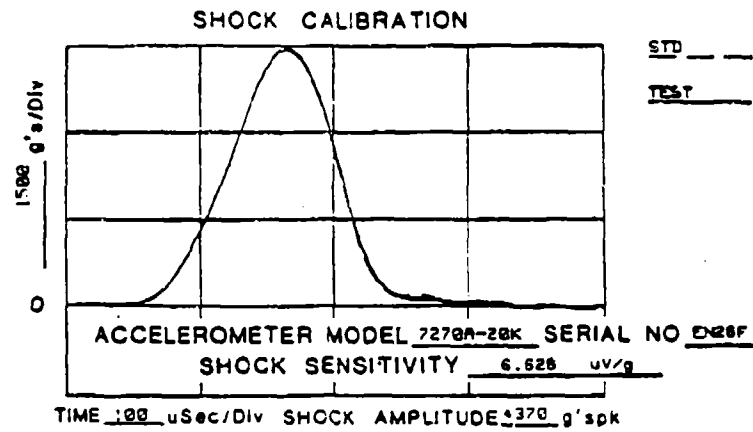**Figure B.3 Stress gage calibration envelope and mean regression.**

SHOCK CALIBRATION

1500 g's/Div

0

ACCELEROMETER MODEL 7270A-20K SERIAL NO EN26F

SHOCK SENSITIVITY 6.628 uV/g

TIME 100 uSec/Div SHOCK AMPLITUDE 4370 g'spk

STD
TEST

SHOCK CALIBRATION

1500 g's/Div

0

ACCELEROMETER MODEL 7270A-20K SERIAL NO EN27F

SHOCK SENSITIVITY 6.470 uV/g

TIME 100 uSec/Div SHOCK AMPLITUDE 4450 g'spk

STD
TEST

SHOCK CALIBRATION

1500 g's/Div

0

ACCELEROMETER MODEL 7270A-20K SERIAL NO EN34F

SHOCK SENSITIVITY 9.829 uV/g

TIME 100 uSec/Div SHOCK AMPLITUDE 4320 g'spk

STD
TEST

Figure B.4   Calibration curves for Accelerometers.

116

APPENDIX C

AFFECTS OF DESATURATION ON SPECIMEN DENSITY

Just as soil depth scales with acceleration of the centrifuge (Section III.B.3.), height of capillary rise also scales with acceleration. The result of capillary rise scaling is a reduction in the rise height and results in desaturation of the pore fluid.

Desaturation curves for Tyndall and Ottawa sands are shown in Figures 3.9(a) and 3.9(b). Capillary rise heights at 1 g for the two sands are 2.04 meters and 1.53 meters, respectively. A typical specimen height for this investigation is 0.28 meters, and at 1 g both sands have the potential to hold at least 70 percent saturation to a height of 0.28 meters. When the specimens are accelerated to 18.9 g's, the height of capillary rise becomes 0.11 meters and 0.08 meters for Tyndall and Ottawa sands, respectively. At 26.3 g's, the height of capillary rise becomes 0.08 meters and 0.06 meters for Tyndall and Ottawa sands. Thus, the saturation of the soil above these capillary heights is at the residual saturation which is approximately 11 and 5 percent for Tyndall and Ottawa sand respectively (Section III.B.1).

The instrument layer is located at a height of 20 cm within the specimen. Thus, at an acceleration of 18.86 g's, the height of the instruments is well above the capillary rise height of 0.11 meters and 0.08 meters for Tyndall and Ottawa sands. As a check to monitor the height of capillary rise for Tyndall sand, water content readings for moist specimens were obtained at various depths immediately after testing. Plots of saturation versus height within the specimens for Tyndall sand are shown in Figures C.1(a) and (b). Curves plotted for Tyndall sand compacted at 17, 35, and 53 percent saturations follow a typical
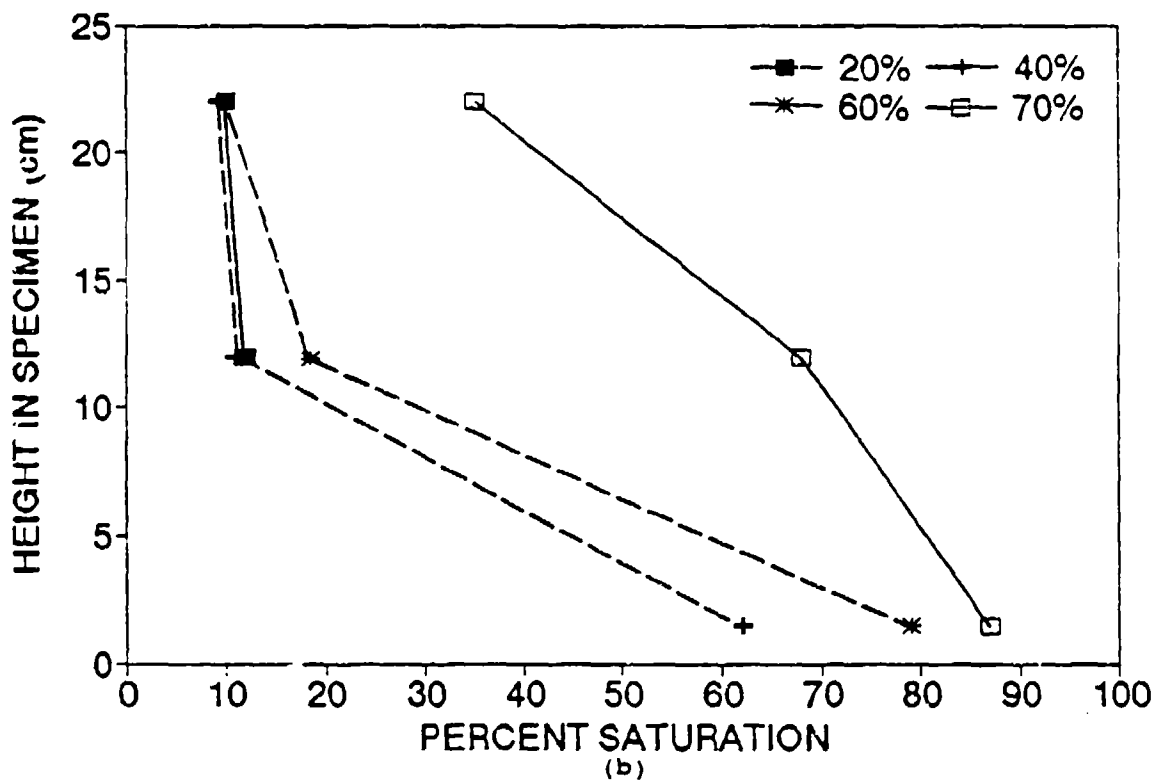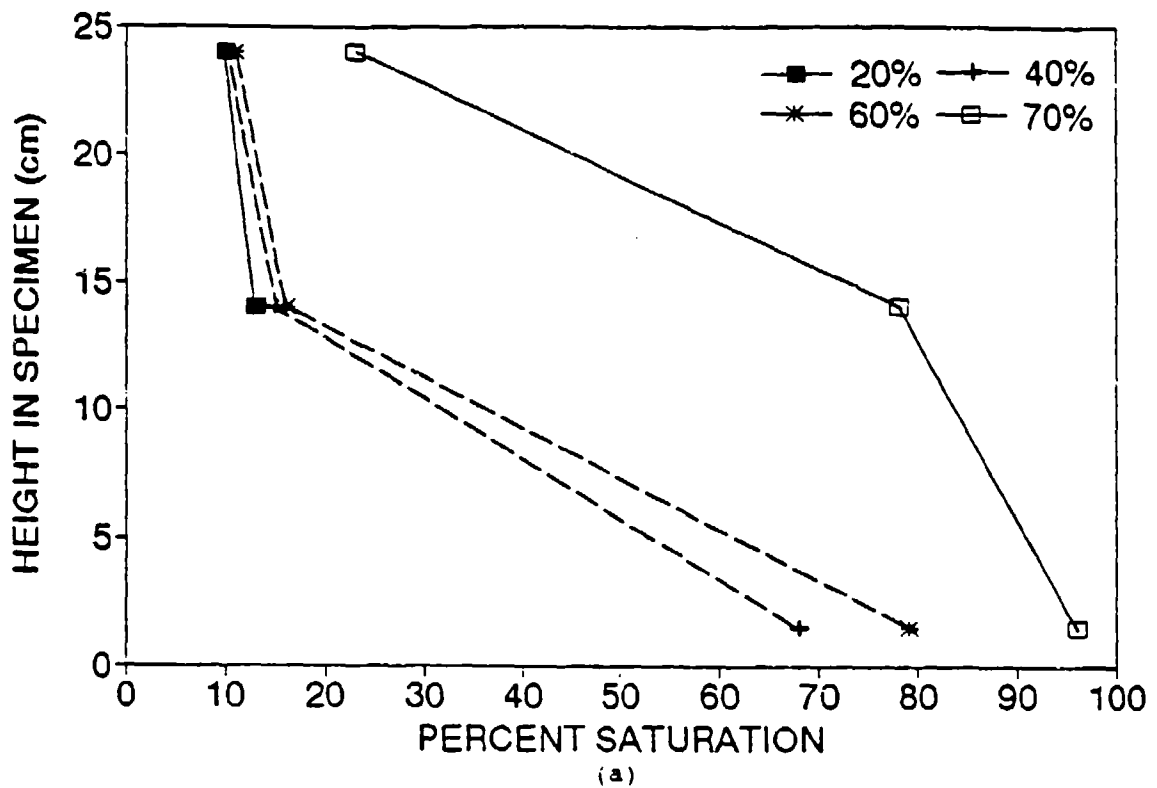
117

Figure C.1   Saturation versus height within soil specimen.   (a) Specimens accelerated at 18.86 g's.   (b) Specimens accelerated at 26.34 g's.

118

desaturation path, and capillary rise heights fall in the range from 12 to 17 cm.

Due to excessive water in the 70 percent saturation specimens of Tyndall sand, a special dry layer was placed at the bottom of the bucket. This allowed for a greater capacity of pore fluid to be stored in the bottom of the specimen away from the instrumentation.

APPENDIX D

PEAK STRESS VERSUS PEAK PARTICLE VELOCITY

Plots of peak stress as a function of peak particle velocity for Tyndall beach sand are shown in Figure D.1. Note that from Equation (2.15)

$$\rho c_c = \frac{P}{V} \qquad (D.1)$$

and thus, the acoustic impedance of Tyndall beach sand is equal to the slope of the regression through the data in Figure D.1. The mean regression slope of all the data form Figure D.1 is 529.,5 kPa/m/s. Values of acoustic impedance determined using Equations (5.3) and (5.4), for Tyndall sand of various saturations, are presented in Table 5.6a.
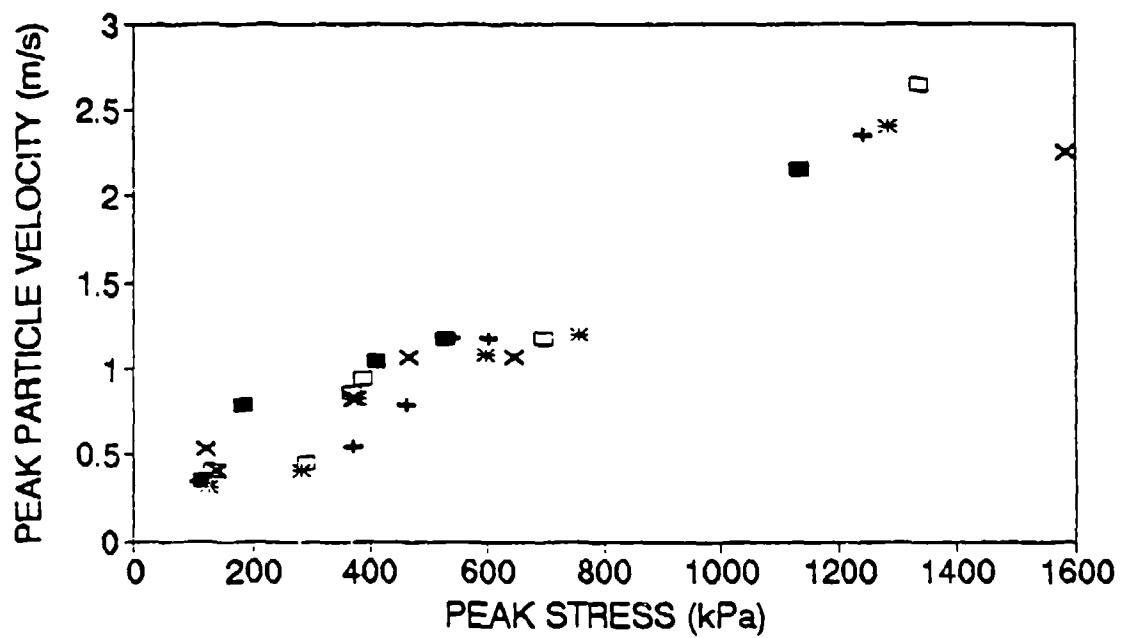
Figure D.1 Plot of peak stress as a function of peak particle velocity.